Study and Development of Optical Fibre Sensors for Refractometric Measurements

Cristina Cunha
Mestrado em Engenharia Física
Departmento de Física e Astronomia
2023

Supervisor
Dr.Orlando Frazão, Investigador Sénior do INESCTEC, Investigador Externo da Faculdade de Ciências
Co-supervisor
Dra.Susana Novais, Investigador Júnior do INESCTEC, Colaboradora Externa da Faculdade de Ciências


U.PORTO
FACULDADE DE CIÊNCIAS
UNIVERSIDADE DO PORTO

Acknowledgements

First, I would like to thank my supervisor Professor Orlando Frazão for the advice given throughout this dissertation development, and for the opportunity to work freely on something I enjoy. This allowed me to find myself as an investigator.

Second, to my co-supervisor Doctor Susana Novais, who accompanied me every step of the way for the past year, thank you for being a good friend and helping me look further in my role as a researcher.

Then, to everyone in INESCTEC, CAP (Center of Applied Photonics), thank you for creating a healthy and propitious environment to learn and develop various important skills, both soft and technical, which also helped to successfully finish this important step in my academic path.

I want to specially acknowledge Doctor Susana Silva, Doctor Catarina Monteiro, António Vaz Rodrigues, Professor Luís Coelho, Doctor João Mendes, Paulo Santos, Paulo Robalinho, Luísa Mendonça and Gaspar for the guidance, patience and technical support in the laboratory.

I also want to give a special acknowledgment to Doctor Cátia Leitão and Ana Assunção, from the University of Aveiro, for the technical support regarding the plasmonic Au sensors. Thank you for your kindness.

To Anselmo Falorca, thank you for being here for the past 3 years, and most important for listening to me and caring. I hope to continue our balcony talks for many years.

Last, but not least, to my friends and family, who I will not name, because it would be too many, thank you for the moral support, and for believing and comforting me when I needed it. Especially to my Mom, whose sacrifices and dedication allowed me to be here.

Thank you to everyone!

Obrigada!

UNIVERSIDADE DO PORTO

Abstract

Faculdade de Ciências da Universidade do Porto
Departamento de Física e Astronomia

MSc. Engineering Physics

Study and Development of Optical Fibre Sensors for Refractometric Measurements

by Cristina CUNHA

This dissertation is focused on the study and development of optical fibre sensors designed for refractometric measurements. Specifically, the sensors developed in this research were explored as a proof of concept for the non-invasive detection of glucose levels in aqueous solutions, spanning a concentration range of 25 to 200 mg/dl, which closely resembles the levels of glucose commonly found in human saliva.

The study began with the experimental characterization of various sensor tips in relation to refractive index (RI) within a reflection interrogation system. Sensor types included single-mode fibres, multimode fibres, coreless silica fibres (CSF), and a configuration that combines CSF with graded index fibres.

After identifying the most promising sensor, further optimization was undertaken. First, by determining the optimal sensor length, taking into account the self-imaging theory, which was accompanied by COMSOL Multiphysics simulations. Second, by applying a thin film of graphene oxide (GO), with a concentration of 80 μg/ml, for sensitivity enhancement using a layer-by-layer technique.

The final sensor to be presented is a functionalized plasmonic gold (Au) sensor based on unclad multimode optical fibre, which is studied in a transmissive interrogation system. Prior to the functionalization process, a RI characterization is presented to assess the quality of the Au coating, along with a comparative study between optical fibres with different core diameters - 400 μm and 600 μm.

In the end, a brief discussion regarding future work and possible further optimization of the presented sensors is provided.

UNIVERSIDADE DO PORTO

Resumo

Faculdade de Ciências da Universidade do Porto
Departamento de Física e Astronomia

Mestrado Integrado em Engenharia Física

Estudo e Desenvolvimento de Sensores em Fibra Ótica para Medidas Refractometricas

por Cristina CUNHA

Esta dissertação tem como principal foco o estudo e desenvolvimento de sensores de fibra ótica para medições refratométricas. Mais especificamente, os sensores desenvolvidos neste estudo foram explorados como prova de conceito para a deteção não invasiva dos níveis de glucose em soluções aquosas, abrangendo uma gama de concentrações de 25 a 200 mg/dl, que se assemelha aos níveis de glucose tipicamente encontrados na saliva humana.

O estudo começou com a caracterização experimental de várias pontas sensoras em relação ao índice de refração (RI) num sistema de interrogação por reflexão. Os tipos de sensores incluíram fibras monomodo, fibras multimodo, fibras de sílica sem núcleo (CSF) e uma configuração que combina CSF com fibras que possuem um perfil de RI parabólico.

Após identificar o sensor mais promissor, foram realizadas otimizações adicionais. Primeiro, ao determinar o comprimento ótimo do sensor, tendo em conta a teoria da auto-imagem, e que foi acompanhada por simulações COMSOL Multiphysics. Segundo, através da aplicação de um filme fino de óxido de grafeno (GO), com uma concentração de 80 μg/ml, para melhorar a sensibilidade, usando uma técnica camada a camada.

O último sensor a ser apresentado é um sensor de plasmónica com ouro (Au) funcionalizado baseado em fibra ótica multimodo sem revestimento, e que é estudado num sistema de interrogação transmissivo. Antes do processo de funcionalização, é apresentada uma caracterização do RI para avaliar a qualidade do revestimento de ouro, juntamente com um estudo comparativo entre fibras óticas com diferentes diâmetros de núcleo (400 μm e 600 μm).

No fim, é fornecida uma breve discussão sobre trabalhos futuros e possíveis otimizações adicionais dos sensores apresentados.

Contents

List of Figures

List of Tables

Glossary

CSF	Coreless Silica Fibre
FBG	Fibre Bragg Gratings
GIF	Graded Index Fibre
GO	Graphene Oxide
HCF	Hollow Core Fibre
LbL	Layer-by-Layer
MZI	Mach-Zehnder Interferometer
MMF	Multimode Fibre
MMI	Multimode Interference
NA	Numerical Aperture
NPs	Nano-Particles
NRs	Nano-Rods
OFS	Optical Fibre Sensor
OSA	Optical Spectrum Analyzer
PCF	Photonic-Crystal Fibre
PCS	Plastic Clad Silica
RI	Refractive Index
SMF	Single Mode Fibre
SMS	Single Mode-Multimode-Single Mode Structure
SP	Surface Plasmon
SPP	Surface Plasmon Polaritons

SPR	Surface Plasmon Resonance
THCF	Tapered Hollow Core Fibre
TCF	Thin Core Fibre
UDU	Up Taper-Down Taper-Up Taper

Chapter 1

Introduction

1.1 Motivation

Nowadays, optical fibre sensors (OFS) are widely applied across various domains for detecting and monitoring diverse parameters including physical, chemical, and biological [1]. These sensors offer various advantages, making them a very attractive topic for research and development within the scientific community. Some of these benefits include compact size, flexibility, affordability, high sensitivity, remote sensing capabilities, and immunity to electromagnetic interference compared to conventional electronic devices.
More specifically, over recent decades, there has been a continuous interest in refractometric based sensors due to their capacity of easy ambient monitoring across various fields [2]. These sensors bring forth several advantages, such as label-free and real-time detection, as well as precise measurements. Coupled with the advantages previously mentioned regarding OFS, refractometric based on OFS present an engaging and interesting option for a wide spectrum of applications. These applications span both industrial sectors, such as the food and beverage industry, environmental monitoring, and healthcare, as well as scientific domains [3, 4].
Moreover, the relationship between refractive index (RI) and the concentration of certain substances has been studied and discussed for several years now, and plays a crucial role in translating RI detection to the corresponding concentration of the analyte, such as glucose. Within the biomedical industry, glucose monitoring is a real-life application which is worth paying attention. Fast and accurate detection of glucose concentration holds immense importance in various sectors such as disease diagnosis, clinical analysis, biotechnology, and quality control within the food industry. Monitoring glucose levels is

crucial for maintaining human health, as abnormal levels can lead to diverse pathological conditions, such as: diabetes, hypoglycemia, and hyperglycemia. Hypoglycemia manifests when blood glucose concentration falls below the normal range (between 80 to 120 mg/dl), while hyperglycemia is characterized by elevated glucose levels. Normally, diabetes is indicated when fasting blood glucose surpasses 180 mg/dl. Continuous efforts within the research community are dedicated to developing a variety of glucose sensors, including those based on optical fibre sensing [5–7]. Particularly, glucometers based on non-invasive detection are a trendy research topic, since the most common and commercialize device yet, still requires to prick the blood and use bio-markers to detect glucose levels. This method is considered invasive, uncomfortable, and not user-friendly, making it a problem in the daily monitorization of glucose, specially, among younger and older generations.

Therefore, in addition to study OFS refractometric sensors, those capable to non-invasively detect glucose in aqueous solutions, to mimic the glucose levels found in saliva, are a central theme explored in this dissertation.

1.2 Objectives

The primary objectives of this dissertation can be categorized into two main areas. The first goal consists of the development of optical fibre sensors for RI detection. Upon accomplishing this initial goal, the second major objective entails a proof of concept for the practical application of the developed sensors. In this stage, the focus shifts towards the study and development of optimal OFS tailored for non-invasive detection of glucose within aqueous solutions. The detection range spans from 25-200 mg/dl, which aligns with the typically observed glucose levels in saliva.

1.3 Structure

The structure of the dissertation is described as follows:

- Chapter 1 introduces the dissertation by outlining its motivation, objectives, structure, and outputs.
- Chapter 2 provides an overview of the key theoretical concepts that support the practical work undertaken in this dissertation. It is divided into sections discussing

different types of optical fibre sensors, which are later developed in the course of the dissertation. The chapter also reviews existing literature regarding refractometric optical fibre sensing.

- Chapter 3 presents the experimental characterization of different refractometric fibre tip sensors. It goes from the simplest to the most complex to be fabricated: starting with a sensor based on a single mode fibre (SMF), then one based on a multimode fibre (MMF), and moving on to a sensor using coreless silica fibre (CSF), and finally, a probe that combines CSF and graded index fibre (GIF). In the end, the performance of the probes are compared regarding RI and temperature sensing, as well as stability and resolution tests.

- Chapter 4 continues from the previous chapter by focusing on optimizing the CSF tip. The first optimization is regarding the length of the probe, using the theoretical principles of self-imaging sensing, and confirmed through Multiphysics COMSOL 6.0 simulation. Additionally, the application of graphene oxide using the layer-by-layer technique is explored as a sensitivity enhancer. The final sensor is characterized in RI, and then, tested for glucose aqueous solutions measurements, as a proof of concept for a real-life application.

- Chapter 5 focuses on the development of a plasmonic sensing structure based on an unclad optical fiber with a gold (Au) coating. The chapter provides a detailed description of the fabrication and functionalization processes of the sensor. Before finalizing the functionalization step, various sensors are characterized in terms of RI to determine which one exhibited the best responses. Subsequently, the sensor with the best response was tested with glucose aqueous solutions at different concentrations.

- Chapter 6 presents final remarks and discusses the future work that can be continued after the dissertation.

1.4 Outputs

Communications in National/International Conferences

C. Cunha, S. Novais, and O. Frazão "Study and development of optical fibre sensors for

glucose detection, *ProDEF Day*, Porto, Portugal, 2022 - **Poster presentation**.

C. Cunha, A.S. Assunção, C.S. Monteiro, C. Leitão, J.P. Mendes, S. Silva, O. Frazão, and S. Novais, 2023, "Transmissive glucose concentration plasmonic Au sensor based on unclad optical fibre". in *2023 IEEE 7th Portuguese Meeting on Bioengineering (ENBENG)*. IEEE, 2023, pp.13-16, Available here - **Oral Communication**.

C. Cunha, S. Silva, O. Frazão, and S. Novais, "Glucose Concentration Monitoring with Advanced Surface Plasmon Resonance Optical Fibre Sensor Technology", *IJUP 2023*, Porto, Portugal, 2023 -**Poster presentation**.

C. Cunha, S. Silva, O. Frazão, and S. Novais, "Proof of Concept for a Self-Imaging-Based Non-Invasive Fibre Sensor for Glucose Detection", *DCE23 - Symposium of Engineering Physics*, Porto, Portugal, 2023 - **Poster presentation**.

C. Cunha, S. Silva, O. Frazão, and S. Novais, "Non-Invasive Glucose Fibre Sensor Based on Self-Imaging Technique: Proof of Concept", *EOSAM*, Dijon, France, 2023, Available here - **Oral communication**.

C. Cunha, S. Silva, O. Frazão, and S. Novais, "Optical Fibre Surface Plasmon Resonance for Glucose Detection", *EOSAM*, Dijon, France, 2023, Available here - **Poster communication**.

Scientific Journals

L. Soares, C. Cunha, S. Novais, A. Ferreira, O. Frazão, and S. Silva, "Refractive index measurements of ethanol-water binary liquid solutions using a graded-index fibre tip sensor", *IEEE Sensors Letters*, pp.1-4, 2023. Available here.

C. Cunha, C.Monteiro, António Rodrigues, S.Silva, O. Frazão, and S. Novais, "Enhanced Sensitivity in Optical Sensors through Self-Image Theory and Graphene Oxide Coating" - **submitted for IEEE Sensors Journal**.

Chapter 2

Literature Review

2.1 Introduction

Over the past few decades, there has been a significant increase in the demand for detecting environmental changes by monitoring physical, chemical, or biological parameters. This surge of interest in the scientific community, as well as in the industrial sector, has led to the development of new sensing devices based on optical fibres. Optical fibres possess unique intrinsic characteristics, which make them attractive for a variety of applications. To remain competitive with traditional sensors, optical fibre-based sensors must be reliable, resilient, and cost-effective, while also exhibiting a high degree of sensitivity. As such, there is a pressing need to improve the performance of these sensors and identify new areas where they can be effectively applied [5].

This chapter begins by introducing the concept of optical fibre, followed by a detailed exploration of the classification of optical fibre sensors. Then, is presented a comprehensive overview of the optical fibre sensors (OFS) developed in the context of this dissertation. The end of the chapter provides an overview of OFS for refractive index (RI) measurements, tracing the evolution of these technologies from their earliest reports to the current state-of-the-art.

2.2 Optical Fibre Concept

The term ”fibre optics” was first named by Kapany in 1958 when he introduced this new field to the research and development community [8]. An optical fibre is a strand of dielectric material which can trap optical radiation at one end and guide it to the other.

Normally, the fibre consists of at least two optically dissimilar materials, as shown in a generalized manner in Figure 2.1[9]. These materials are arranged so that one material, called the cladding, completely surrounds the other. The central material, called the core, normally carries the majority of the transmitted energy. This energy is trapped in the core by reflection at the boundary surface where the core and cladding meet. Often the cladding is itself surrounded by further layers which are added mainly for mechanical strength and protection, but which are not intended to directly influence the guiding properties of the fibres. The refractive index of the cladding, n_{cl}, should be lower than the refractive index of the core, n_{co}, to allow light to be confined in the core through total internal reflection. The critical angle, θ_c, corresponds to the minimum angle of incidence that yields total reflection and can be calculated using Snell's Law, which is presented as the following equation [9]:

$$\theta_c = sin^{-1}\left(\frac{n_{cl}}{n_{co}}\right) \tag{2.1}$$

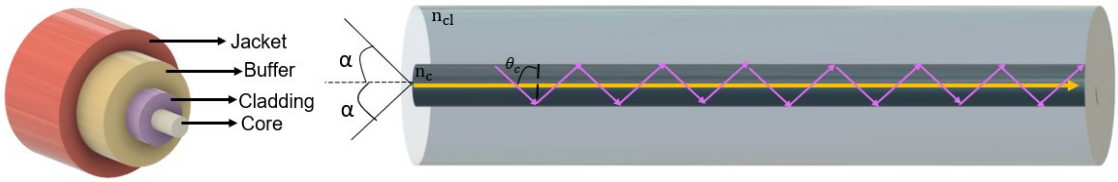

FIGURE 2.1: Optical fibre scheme. Adapted from [9]

The cladding layer of an optical fibre serves multiple purposes, including reducing scattering loss caused by dielectric discontinuities at the core surface, increasing mechanical strength, and protecting the core from surface contaminants. Losses in optical fibres can be broadly classified into two categories: intrinsic losses, which are caused by inherent characteristics of the fibre such as scattering, absorption, and dispersion due to structural defects; and extrinsic losses, which are caused by operating conditions such as splicing loss, connector loss, and curvature loss [10]. The modes of an optical fibre are the guided electromagnetic waves that describe the propagation of light along the waveguide. Each mode has a specific pattern of electric and magnetic field distributions that is repeated at equal intervals along the fibre. Moreover, only a certain number of modes are capable of propagating through the fibre, and these are the electromagnetic waves that satisfy both the homogeneous wave equation within the fibre, as well as the boundary conditions at the waveguide surfaces [11]. Optical fibres can be divided into two categories based on the number of modes they can support: single-mode fibre (SMF), which can only support

a single mode, and multimode fibre (MMF), which can support multiple modes. Additionally, both SMF and MMF can be further divided into step-index fibres and graded-index fibres based on variations in the composition of the fibres core and consequently a refractive index profile distinct. The classification of optical fibres is illustrated in Figure 2.2, where a represents the radius of the core [10].

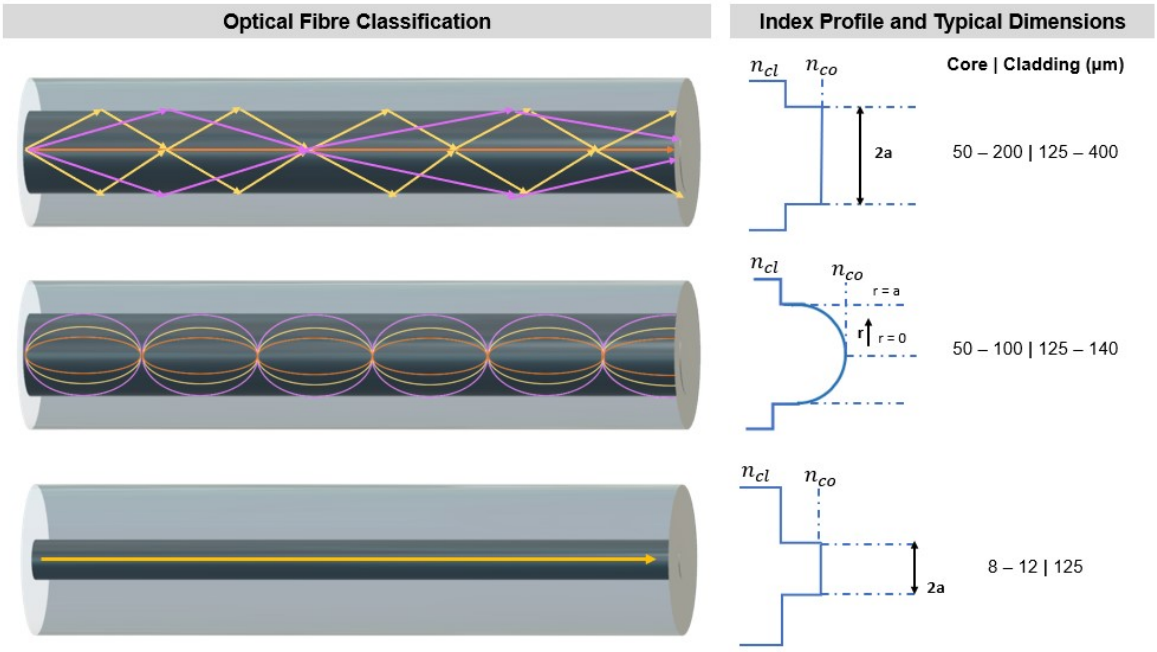

FIGURE 2.2: Comparison of conventional multimode step-index (first), graded-index optical fibres (second) and single-mode (third) based on [10].

Furthermore it is also possible to define the numerical aperture (NA) of the fibre when discussing MMF. The numerical aperture is the measure of the ability of an optical fibre confine incident light into the fibre and can be define as follows [9]:

$$NA = sin(\alpha) \tag{2.2}$$

Where α corresponds to the half-angle of the maximum cone of light that can enter into the fibre.

2.3 Optical Fibre Sensors

A sensor can be defined as a device that detects changes in a physical/chemical quantity and can provide some type of feedback signals. In recent years, optical fibre technology has emerged as a highly attractive and promising technology for sensing applications and has been extensively investigated by the research and development community due

to its commercial value [5, 12]. When compared to conventional electronic sensors, OFS offer a range of advantages, including immunity to electromagnetic interference and radio frequency interference, safety and reliability in harsh environments, low volume and weight, high sensitivity and resolution, and low cost. These advantages have contributed to the development of numerous optical fibre sensors for accurate sensing applied in a wide-ranging applications, such as: environmental, health care, industrial process control, aerospace, and others [12–15].

Figure 2.3 depicts the general structure of an OFS, presenting a scheme in both transmission and reflection. In reflection an optical circulator can be added to interrogate the sensor. Typically, in the simplest form, an OFS includes a light source (e.g., laser, LED), optical fibre as the medium to transmit light, sensing or modulating element, photodetector and processing electronics, such as oscilloscope or Optical Spectrum Analyzer (OSA) [16]. The principle of operation behind any OFS is based on the interaction of light with physical or chemical parameters that are being measured. The sensing element modulates some parameter of the optical system (intensity, wavelength, polarization, phase) which consequently leads to a change of the optical signal received at the photodetector [16, 17].

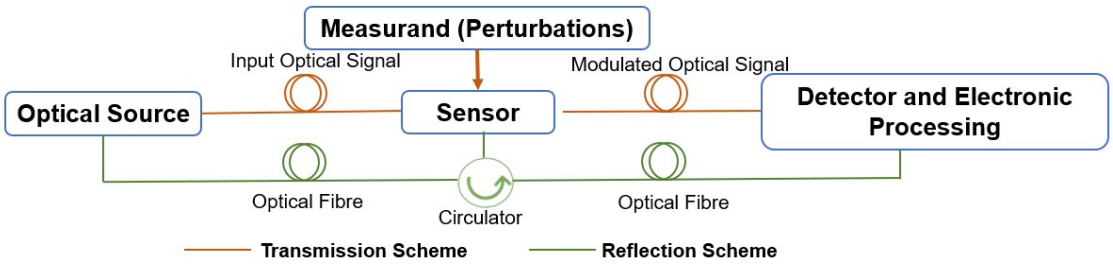

FIGURE 2.3: Typical optical fibre sensor system. Adapted from [18].

2.3.1 Classification of Optical Fibre Sensors

Optical fibre sensors presence in the global industry and continued interest by the research and development community lead to the existence of several categorizations of OFS. Thus, OFS can be mainly classified based on:

- **Modulation process**: phase, polarization, intensity and wavelength[17];
- **Sensing elements**: depending where the modulation takes place, outside or inside the fibre, an OFS can be extrinsic or intrinsic respectively [17];

- **The measurable spatial scope**: single-point, multi-point, or distributed [18];
- **Operating application**: strain, temperature, RI, humidity, pressure, curvature, detection of biomolecules or chemical species, among others [1];
- **Working principle**: loss-related mechanisms (fibre attenuation, end coupling, fibre bending loss) [19, 20], optical fibre interferometers (e.g., Mach-Zehnder, Michelson, Fabry-Perot, Sagnac) [21], optical fibre gratings (Bragg gratings, long period gratins)[22, 23] or nonlinear optical effects and scatterings (Rayleigh scattering, Raman Scattering, Kerr effect) [24].

In the following sections the optical fibre sensors studied and developed in the context of this dissertation will be discussed in more detail to provide a general and comprehensive understanding of the sensors under consideration.

2.3.2 Intensity Modulated Sensors

Intensity modulated sensors make use of the modulation of light intensity to detect changes and consequently being able to measure different physical parameters such as pressure, strain, temperature, among others. For example, changes in temperature can lead to alterations in the RI of the optical fibre which then translates into a change in the intensity of the light that is detected at the detector [17]. Normally, this modulation process require more light to function due to the fact that they detect changes in the intensity of light. Consequently, large-core multimode fibres are a suitable choice to be part of the sensing system [16]. There are several advantages when using intensity-modulated sensors as they can offer a cost-effective and simple solution for sensing applications, and they are also compatible with the widely-used multimode fibre technology, making them an accessible and practical choice for many applications. Nevertheless, when dealing with intensity modulated sensors it should be taken into consideration the fluctuations of the light source intensity as it can induce errors in the measurements.

2.3.3 Multimode Interference Sensors

Multimode interference (MMI) optical fibre sensors are fundamentally based on the interference of light in multimode fibre. The MMI, as a typical example, includes the single mode-multimode-single mode structure (SMS) and has been explored as an attractive technology for optical communications and sensing [25]. When light is coupled into

the fibre different modes are excited and propagate with different propagation constants leading to an interference pattern that is sensitive to external perturbations [17]. In 2003 Mehta and his team proposed the first based MMI fibre optic sensor. The sensor is composed of a multimode step-index fibre tip that has been cleaved and paired with a planar mirror. This combination can detect the reflected optical power based on the longitudinal displacement between the mirror and the multimode fibre [26]. Figure 2.4 presents a typically SMS structure.

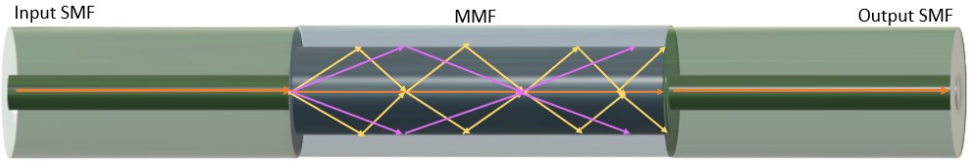

FIGURE 2.4: Schematic configuration of SMS. Adapted from [25].

There are several advantages in MMI sensors such as: affordability, compact size and simplicity, high sensitivity, facility of manufacture, high repeatability, and versatility as they can be applied to monitor a variety of physical parameters. Additionally, MMI sensors are also versatile in their configurations:

- **MMI based sensors with coreless termination fibre (CSF)**: the MMF is substituted by the CSF in the SMS structure (SCS) - Figure 2.5**.a** [27];
- **Conventional SMS fibre sensors**: MMF fusion spliced between input and output SMFs - Figure 2.5**.b** [28];
- **Cascade of MMI-Based fibre sensors**: system where multiple MMI fibre sensors are connected in series to form a cascade in order to improve sensing performance - Figure 2.5**.c** [29];
- **MMI-based sensors with tapered fibre**: the MMF or CSF sections can be tapered to increase the evanescent wave and, consequently, the effective index of the guided mode is more sensitive to the RI of the surrounding medium - Figure 2.5**.d** [29].

2.3.4 Surface Plasmon Resonance Sensors

The evolution of fibre optic surface plasmon resonance (SPR) sensors dates back to the early 1990s. In 1990, one of the pioneering studies on fibre-optic SPR sensors was reported by Villuendas and Palayo [30]. They presented a SPR-based optical fibre sensor

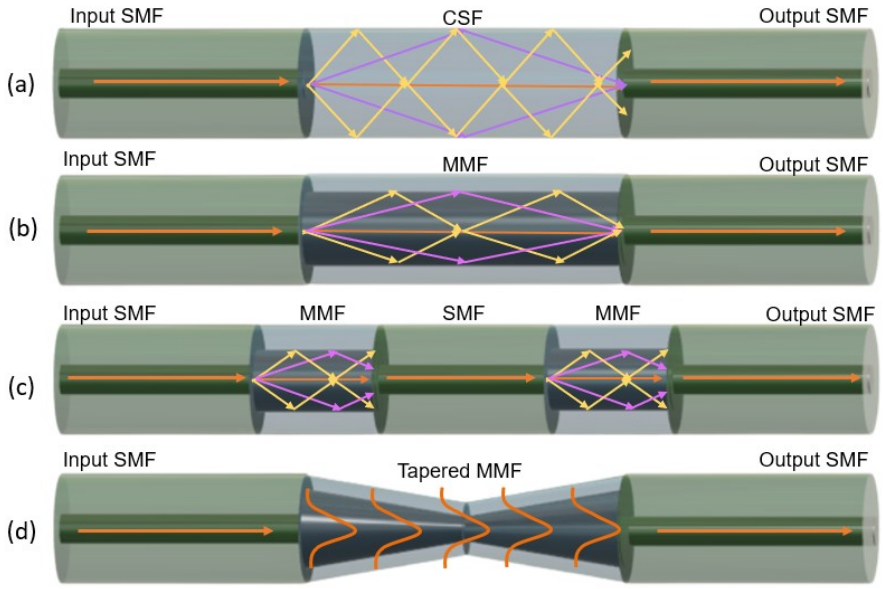

FIGURE 2.5: Typical configurations of MMIs: a) SCS, b) SMS, c) cascade SMS, d) tapered SMS. Adapted from [25].

that demonstrated sensitivity and dynamic range in measuring sucrose concentration in aqueous solution. The results showed good potential for use in chemical detection. Since then, SPR fibre sensors have become a powerful tool for bio-sensing and chemical detection due to their high sensitivity and specificity. Furthermore, they can provide real-time measurement and can be integrated into compact and portable systems making them suitable and attractive options in other fields such as clinical diagnostics, environmental monitoring and food safety. In theory, the collective oscillation of free electrons in metallic surfaces is known as plasmon, owing to the fact that the density of free electrons in a conductor is approximately 10^{23} cm^{-3}, which is comparable to the density of plasma. In this sense, surface plasmons are collective oscillations of electrons that occur at an interface between two media with dielectric constants of opposite signs, usually a metal, with dielectric constant $\epsilon_m < 0$ (for example, gold (Au) or silver (Ag)), and a dielectric, with constant dielectric $\epsilon_m > 0$ (for example, air or water) [31]. The principle of operation for a SPR sensor is based on the interaction of light with a metal film at the interface with a dielectric material. The beam of photons can excite the collective conduction electrons creating an oscillation movement in the metal film, the surface plasmon, that propagates along the interface of the metal-dielectric material. The film must be thin, at the nanometric scale, so that the evanescent field from the waveguide, which decays exponentially in the perpendicular direction to the metal surface, can penetrate the metal and excite surface

plasmons at the metal-dielectric interface [31, 32]. When the wave vector of the evanescent wave at the waveguide-metal interface and the wave vector of the surface plasmon created at the metal-dielectric interface are coincident it gives rise to the phenomenon of SPR. Hence, as the wave vector is a function of the refractive index or dielectric constants of the materials, sensors based on SPR can be used to sense different physical parameters such as the RI [31].

Figure 2.6 illustrates a typical configuration of SPR based on optical fibre. The fabrication of the sensor consists in removing a small portion of the cladding from the fibre followed by coating the unclad core with a thin metallic film [33].

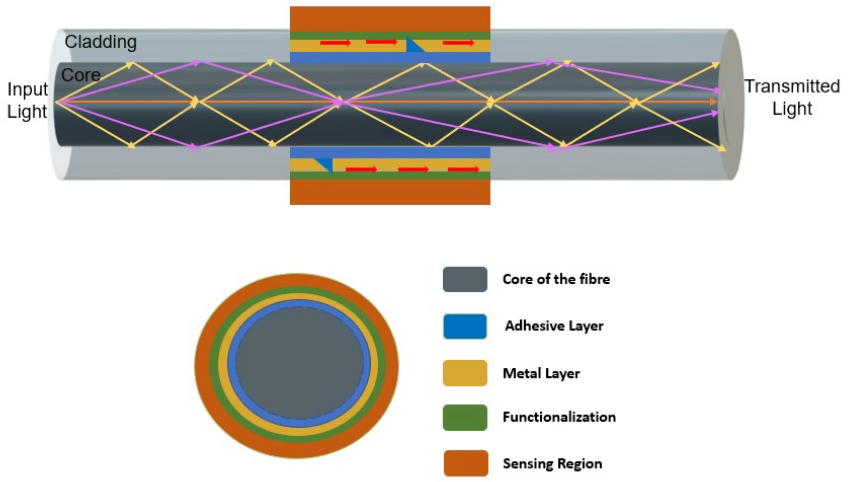

FIGURE 2.6: Schematic configuration of typical SPR fibre optic sensor: longitudinal view and cross-sectional view. Adapted from [33, 34]

Since the metallic film greatly influences the performance of SPR sensors, various metals have been studied to enhance their sensitivity. The most commonly explored metals include Au [6] and Ag [35]. Among these, Au is probably the most extensively studied and utilized in SPR sensors due to its strong SPR dip (minimum in reflectivity), chemical inertness, stability, and ease of functionalization for immobilizing biomolecules. On the other hand, other metals have presented significant limitations. For instance, silver has a sensitive SPR, however it is highly prone to oxidation. Copper and aluminum offer low sensitivity and are also susceptible to oxidation. Sodium is violently reactive, and indium is expensive. Moreover, the thickness of the metallic nanofilm is another crucial factor that must be carefully considered. For instance, the Au thickness of 50 nm generally enables a higher sensitivity of the sensor since it allows for the acquisition of the narrowest and deepest SPR attenuation. However, an adjustment in the Au thickness of just 5 to 10 nm

can shift where the SPR wavelength is located, changing the sensitivity of the sensor and, in turn, their performance [36].

To improve the stability and the support to plasmonic material it can be applied coating adhesive layers, namely, Titanium, between the fibre and the metallic film since the surface of the fibre is very smooth [34].

Nowadays, in chemical detection most SPR sensors make use of functionalization processes to improve the specificity and optimization of the sensor. The most common process for functionalization of an analyte is by covalent binding which involves creating a chemical bond between an enzyme with high affinity to the analyte to be studied and the metal surface [6].

2.3.5 Graphene Oxide Based Sensors

Graphene is a single atomic layer of graphite, which can be defined as a two-dimensional (2D) monolayer of carbon atoms that are joined by strong covalent bonds and arranged in a hexagonal lattice [37]. The first isolation of graphene was reported in 2004 by Novoselov and Geim [38]. The isolation was possible using a mechanical exfoliation method combined with repeated peeling of graphene layers using adhesive tape. Since then, graphene has spark the interest in the research and development community demonstrating stunning properties: high specific surface area, conductivity and strength, biocompatibility, broadband light absorption and transparency, among others [37, 39]. In the last decade, OFS based on graphene materials have emerge as part of an active and attractive area of research as they combine the advantages of the optical fibre and the unique properties of the graphene.

Furthermore, instead of using graphene, graphene oxide (GO) can be used, as it can be more advantageous than graphene from a cost and commercial scale perspective. Additionally, GO is characterized by high levels of oxygen functionalization that form covalent bonds with the hexagonal carbon lattice. These properties confer excellent sensitivity and selectivity to GO in the context of biochemical sensing applications [40]. Several reports have demonstrated enhanced sensitivity of different configurations using GO coatings compared to conventional configurations. For instance, GO coatings have been utilized in Mach-Zehnder interferometers for measuring temperature and humidity [41], detecting glucose [42], in fibre bragg gratings (FBG), for detecting ethanol in petrol [43], and in MMI based on SMS configuration for sucrose detection [44], among other applications.

2.4 Overview on Refractive Index Sensors

Since the focus of this dissertation is on developing various RI sensors based on optical fibre, the following section provides an overview of such probes, combined with the fundamentals already discussed in the previous sections.

The earliest optical fibre refractometers reports were proposed in 1982 and 1983 by Peter Cooper [45, 46], where he performed RI measurements of several different liquids. Moreover, he suggest that the variation of RI with increasing wavelength was described by a smooth monotonically decreasing function. In the following year, Kumar *et al.* [47] used a multimode tapered optical fibre to propose a novel fibre-optic refractometer with greater sensitivity compared to previous reports.

Currently, optical fibre refractometers have evolve substantially as RI measurements are a significant characteristic of an optical material and can be used in application fields such as monitoring environment, biomedical therapy, and diagnosis, analyzing material biochemical sensing. For instance, in 2018 Novais *et al.*,[7] proposed an optical fibre tip sensor for the measurement of glucose aqueous solutions and in 2021 Yasli *et al.* [48] reported a based surface plasmon resonance (SPR) photonic crystal fibre (PCF) biosensor for cancer detection. The sensor detects variations in the RI of cancer cells compared to other cells. In the last forty years, numerous configurations for RI sensing have been proposed, leading to a vast and extensive literature on the topic. To provide an overview of recent developments, the table below presents a selection of reports on the measurement of RI and other physical parameters from the last 5 years. The focus of the literature was on the sensors with the principle of operation explained in the previous section *.

TABLE 2.1: Reported literature of refractive index optical fibre sensors from 2018 to 2022.

Year	Sensor Mechanism	Configuration	Length (mm)	Measurand	Range	Sensitivity	Ref
2018	MMI+MZI	Tapered SMF UDU (up tapers diameter 160 μm, down taper diameter 250 μm)	50	RI Strain Temperature	1.3211-1.3527 RIU 0-423.529 $\mu\epsilon$ 23ºC-54ºC	131.93 nm/RIU 0.0007 nm/$\mu\epsilon$ 0.0878 nm/ºC	[49]

*Glossary regarding the presented table: HCF-Hollow Core Fibre, MZI-Mach-Zehnder Interferometer, NPs-Nano Particles, NRs- Nano Rods, PCF-Photonic-Crystal Fibre, PCS-Plastic Clad Silica, THCF-Tapered Hollow Core Fibre, TCF-Thin Core Fibre, UDU-Up Taper-Down Taper-Up Taper

Table 2.1 continued from previous page

Year	Sensor Mechanism	Configuration	Sensing Length (mm)	Measurand	Range	Sensitivity	Ref
2018	MMI	SMF+etched coreless (diameter 24.4 μm)	5.1	RI	1.315-1.365 RIU	627.9 nm/RIU	[50]
2018	MMI	SMF+etched coreless (diameters between 24-125 μm)	24	RI	1.364-1.397 RIU	1467.59 nm/RIU	[7]
2018	GO based SPR	PCS (diameter 600 μm) tip with Ag/GO coating	10	RI	1.3334-1.3731 RIU	3311 nm/RIU	[51]
2018	SPR	MMF+CSF with Au coating+MMF	12	RI	1.343-1.373 RIU	3475.1 nm/RIU	[52]
2019	MMI	SMF+MMF (core diameter 105 μm) with periodically CSF sections+SMF	20	RI	1.333-1.405 RIU	206.96 nm/RIU	[53]
2019	MMI	SMF+CSF (tapered diameter 13 μm)+SMF	20	RI	1.333-1.350 RIU	686 nm/RIU	[54]
2019	MMI	MMF+CSF (lateral offset of 62.5 μm) +MMF	10	RI Temperature	1.3330-1.3468 RIU 20°C-100°C	-1364.343 nm/RIU 33 pm/°C	[55]
2019	SPR	MMF+CSF (diameter 125 μm) with Au coating +MMF	10	RI	1.3335-1.4019 RIU	4328.2 nm/RIU	[56]
2019	MMI+SPR	MMF+CSF (diameters between 61.5-125 μm) with chromium and Au coatings+MMF	10-20	RI	1.3330-1.4102 RIU	min:1473 nm/RIU max:11792 nm/RIU	[57]

Table 2.1 continued from previous page

Year	Sensor Mechanism	Configuration	Sensing Length (mm)	Measurand	Range	Sensitivity	Ref
2020	MMI+MZI	SMF+MMF (folded tapered diameter 40μm) +CSF+SMF	8	RI Temperature	1.3405-1.3497 RIU 20°C-90°C	1191.5 nm/RIU 64.8 pm/°C	[58]
2020	GO based MMI	SMF+CSF (diameter 125 μm)+SMF	30	RI	1.3300-1.3385 RIU	1348.67 nm/RIU	[59]
2020	MMI	MMF+SMF (tapered diameter 50 μm)+MMF	2.2	RI	1.333-1.437 RIU	1879.87 nm/RIU	[60]
2020	MMI+SPR	SMF+CSF (diameter 200 μm) with Au coating+SMF	12	RI Temperature	1.333-1.383 RIU 20°C-80°C	2061.6 nm/RIU 37.9 pm/°C	[61]
2020	SPR	GIF (diameter of 20 μm) with hole (diameter 10 μm) at center of the core	—	RI	1.38-1.49 RIU	4350 nm/RIU	[62]
2020	SPR	MMF+PCF with Au coating and Au NPs/ NRs +MMF	10	RI	1.33320-1.33610 RIU	15747 nm/RIU 25642 nm/RIU	[63]
2021	MMI	SMF+MC-MMF (core diameter 28 μm) +SMF	3.05	RI	1.41-1.43 RIU	890 nm/RIU	[64]
2021	MMI	SMF+TCF (core diameter 2.5 μm) +CSF (diameter 125 μm) +SMF	170	RI Temperature	1.3333-1.3794 RIU 15°C-85°C	109.9 nm/RIU -4.9 pm/°C	[65]
2021	SPR	Parallel polished POF with Au coating (diameter 600 μm and 800 μm)	13-24	RI Temperature	1.335-1.370 RIU 30°C-80°C	1174 nm/RIU -0.7 nm/°C	[66]
2021	SPR+MMI	MMF+CSF with Ag coating (diameter 125 μm) +MMF	20	RI	1.3330-1.3723 RIU 1.3723-1.4107 RIU	2507.58 nm/RIU 5228.21 nm/RIU	[67]

Table 2.1 continued from previous page

Year	Sensor Mechanism	Configuration	Sensing Length (mm)	Measurand	Range	Sensitivity	Ref
2021	SPR	MMF with bimetallic coating of Ag and Au followed with titanium dioxide layer	—	RI	1.33-1.37 RIU	14300 nm/RIU	[68]
2021	GO based MMI	SMF+CSF (diameter 125 μm) coated with GO through drop plating+SMF	30	RI	1.33-1.39 RIU	496.823 nm/RIU	[69]
2022	SPR+MMI	MMF-THCF (diameter 30 μm) -MMF	5	RI	1.335-1.400 RIU	7592.25 nm/RIU (1.40)	[70]
2022	SPR	side-polish POF (diameter core 980 μm) with Au coating	22	RI	1.335-1.390 RIU	2008.58 nm/RIU	[71]
2022	MMI	CSF (diameter 125 μm) -HCF (core-offset with inner diameter 4 μm) -CSF	10	RI	1.3355-1.3625 RIU	245.67149 nm/RIU	[72]
2022	GO based SPR	MMF (diameter 600 μm) coated with Au NPs and GO	20	RI	1.33-1.38 RIU	79 nm/RIU	[73]
2022	MMI	microfibre (diameter less than 10 μm) with UV Glue distributed silicon/Ag NPs	6	RI Temperature	1.3313-1.3422 RIU 28°C-43°C	Ag NPs: 1382.3 nm/RIU silicon NPs: 1769.7 nm/RIU 2.08 nm/°C	[74]

2.5 Concluding Remarks

This chapter has provided a brief review and discussion of a selection of optical fibre sensors that are relevant to this dissertation. Additionally, since the devices that will be developed in the context of this dissertation are optical fibre sensors for refractive index measurements, a representative overview from the earliest to recent state-of-the-art is presented.

As for the future, the field of optical fibre sensors is exciting and dynamic, with constant evolution and growing. Hence, there is continuous interest in the research and development community to expand, develop, and optimize their performance and capabilities. Refractometric fibre sensors are particularly important in this context because they are flexible and can be integrated into a variety of systems and devices. They are also highly sensitive and selective, making them well-suited for a range of applications, particularly in the areas of chemical and biological sensing.

Chapter 3

Refractometric Fibre Tip Sensors

3.1 Introduction

Fibre tip sensors are typically designed to detect changes in physical and/or chemical parameters of the surrounding medium by utilizing an interrogation system based on reflection/transmission. They have been extensively studied in fields such as chemistry and biology, where their flexibility and ability to be integrated into different interrogation systems make them ideal for molecular and biochemical sensing [75, 76]. One of the key advantages of fibre tip sensors comes from the fact that only the tip needs to be immersed in the medium that is being investigated, allowing for precise, localized and easy measurements. In addition, it is possible to reduce the size of the sensor by employing a reflection scheme, and since the light travels back and forth it leads to higher sensitivities. This chapter introduces four distinct tips for refractive index (RI) liquid sensing: single mode fibre (SMF), multimode fibre (MMF), coreless silica fibre (CSF), and CSF combined with a graded-index fibre (GIF). The chapter progresses from the simplest tip, the SMF, to the most complex fabricated, the CSF and GIF tip. It was also conducted temperature experimental studies for each sensing probe, as well as resolution and stability tests.
Finally, a summary of the achieved results is provided at the end of the chapter, along with concluding remarks that compare the four tips.

3.2 Experimental Setups

The optical sensors presented in this chapter follow the same interrogation system for RI and temperature measurements. The experimental setup used in the laboratory consisted

of a broadband optical source (1520-1620 nm), the sensor, and an Optical Spectrum Analyzer (OSA, Yokogawa AQ6370C, Japan) connected with a circulator. The OSA has a resolution of 20 pm and can measure wavelengths ranging from 600-1700 nm. In the case of the RI liquid measurements, to ensure stability and prevent contact between the sensor and the walls of the sample tubes, it was inserted into a capillary tube. Furthermore, to maintain its static positions, the samples were handled on a lifting platform, allowing for only vertical movement. For the temperature tests, the sensors were inserted horizontally into an optical fibre curing oven, with working temperatures ranging from 25ºC to 85ºC. Figure 3.1 depicts both setups.

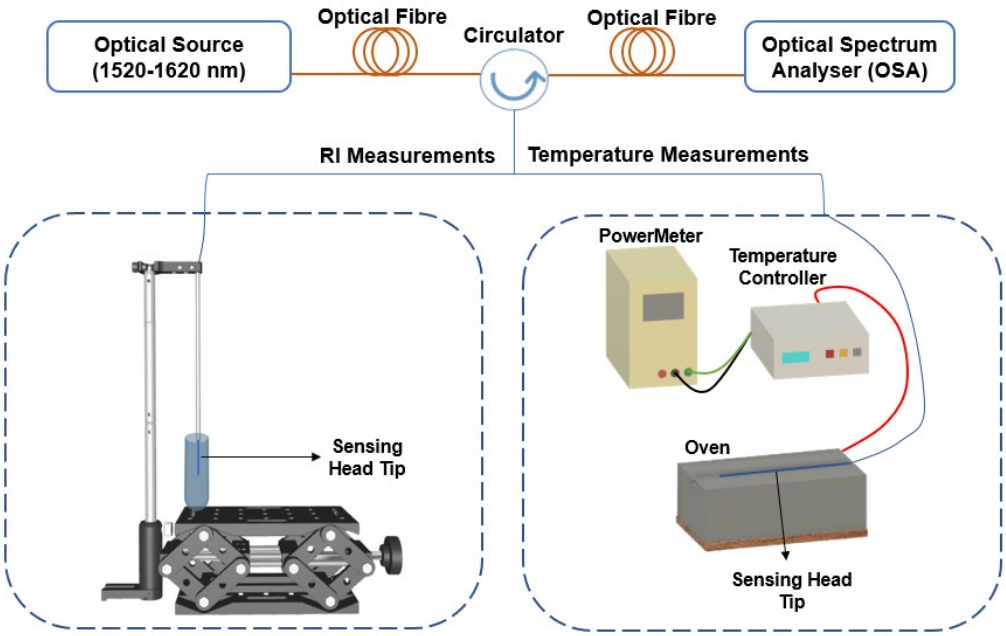

FIGURE 3.1: Schematic configuration of the setups for RI and temperature experiments - image not to scale.

3.3 Methodology

In this chapter, the methodology applied to conduct experiments with the four different sensor tips follows a consistent approach. Therefore, the methodology will be introduced first, followed by the details of the fundamentals of operation and design for each sensor, along with the respective experimental results.

The liquid samples used for RI testing were prepared in a laboratory-controlled environment at approximately 21 °C. Glucose monohydrate supplied by Sigma-Aldrich was used to prepare aqueous solutions, which were homogenized using a magnetic stirrer

(NAHITA, magnetic stirred, model n°690/1). The RI of each solution was determined using an Abbe refractometer (ATAGO, DR-A1). In the OSA, measurements were taken in real-time at a resolution of 0.5 nm with 1001 points, and the signal was normalized in relation to a SMF (SMF28, 0.14 NA - numerical aperture, Thorlabs) that conducted the input light. During RI sensing experiments, the tips were fully immersed in the prepared solutions for 150 seconds and cleaned with ethanol between each measurement to prevent glucose particles from adhering to the fibre. For the temperature experiments, the responses of the sensors were evaluated over the range of 30ºC to 80ºC in 5ºC increments, 10 in 10 minutes for the signal to stabilize. For the resolution tests, the probes were immersed in two solutions with different RI for one hour each, while in the stability tests, the tips were immersed in one solution for one hour. The resulting spectrum was continuously recorded at one-minute intervals.

3.4 Sensor Based on Single Mode Fibre

3.4.1 Fundamentals of Sensor Operation and Design

The sensor design consists of a SMF (SMF28, 0.14 NA, Thorlabs) tip with 125 μm cladding diameter and 8.2 μm core diameter. The end of the fibre was cleaved perpendicularly to the optical axis. As light reaches the interface between the tip and the liquid, a Fresnel reflection occurs and a portion of the light is reflected back. The amount of light that is reflected back depends on the difference between the RI of the fibre and the liquid, as well as the angle of incidence of the light - which can be deduced from the Fresnel equations. The Fresnel reflectivity, R, in the case of normal incidence, can be calculated as follows:

$$R = \left(\frac{n_c - n_l}{n_c + n_l} \right)^2 \tag{3.1}$$

Where n_c correspond to the RI of the fibre core and n_l to the RI of the sensing medium, as presented in Figure 3.2. Considering a sensing range being between 1.33 to 1.39 RIU, a higher n_l leads to a lower R, consequently, less optical power is detected. Therefore, it can be concluded that the SMF tip acts as an intensity modulated sensor.

3.4.2 Experimental Results

Figure 3.3 shows the optical power shift in the resulting reflection spectra when the probe is directly exposed to the solutions with different RI between 1.3368 and 1.3836 RIU. When

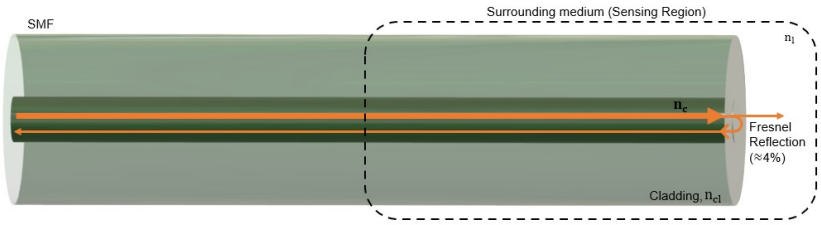

FIGURE 3.2: Schematic diagram of the sensor structure - SMF tip.

the RI of the samples increases the optical power decreases, as mentioned previously in 3.4.1. It can be concluded that the SMF tip is an intensity modulated sensor, and only changes in the optical power are observed.

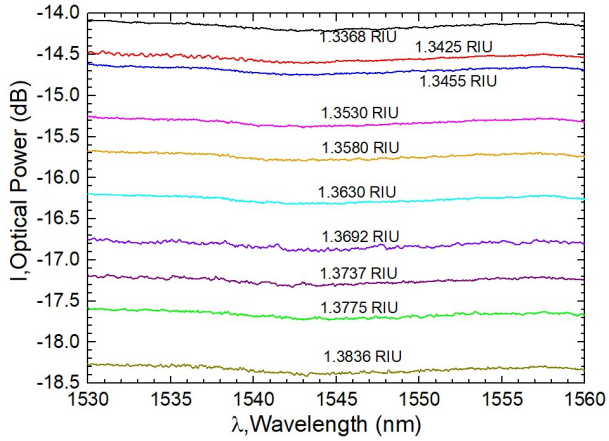

FIGURE 3.3: Output spectra of the SMF tip under different RI solutions.

The experimental results from the RI and temperature testing are presented in Figures 3.4a and 3.4b, respectively. In both studies is possible to observe a linear relationship between the parameters and the optical power. It can be noted that in both cases, a higher RI and higher temperature lead to a decrease in optical power. In the last case, is due to thermal variations as the RI of the material composing the fibre is also dependent on temperature.

The sensor showed an intensity sensitivity of -90±2 dB/RIU and a correlation coefficient (R^2) of 0.993 as a function of RI. Regarding the temperature a sensitivity of (-1.51±0.03)$\times 10^{-2}$ dB/ºC was obtained with a R^2 equal to 0.996. Both sensitivities were achieved through a wavelength-averaging span between 1530 and 1562 nm.

In Figures 3.5a and 3.5b the results of the stability and resolution tests are presented, respectively. For the stability study, the sensor was immersed in a glucose aqueous solution with a RI of 1.3775 RIU for one hour. In the case of the resolution study, the sensing probe

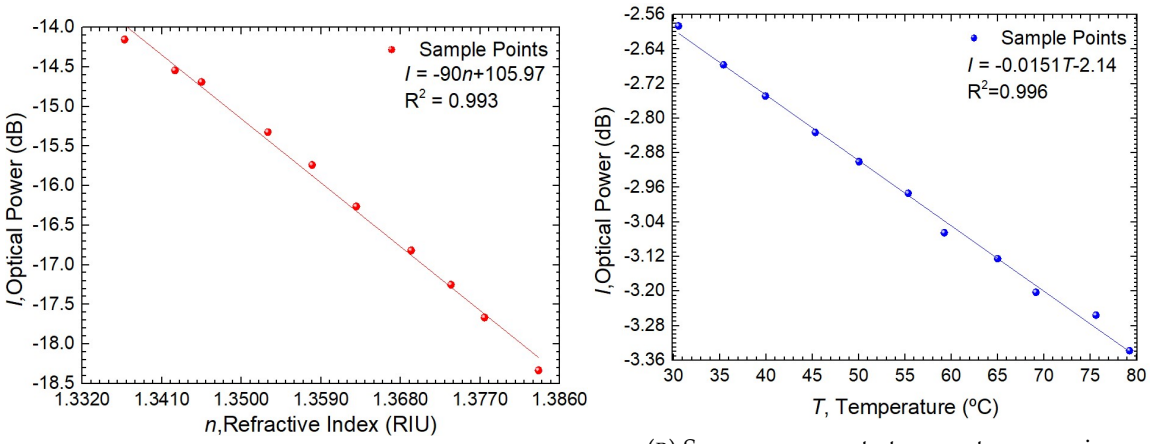

(A) Sensor response to RI experiment.

(B) Sensor response to temperature experiment.

FIGURE 3.4: RI and temperature measurements.

was immersed in two different solutions, 1.3455 RIU and 1.3775 RIU, for one hour each.

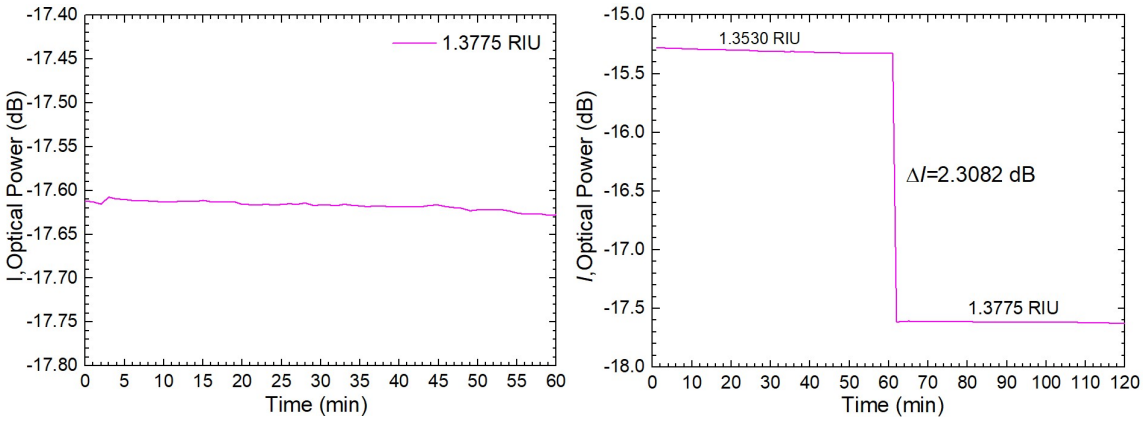

(A) Sensor stability test.

(B) Sensor resolution test.

FIGURE 3.5: Stability and resolution tests.

The stability test of the sensing probe presented a standard deviation of 1.36×10^{-5} dB/min. This indicates that the sensor exhibited very low variation or noise in its measurements over time, demonstrating a high level of stability and consistency. In the resolution test it was possible to determine the minimum value variation of RI that the sensor could discriminate, δ_{RI}, by applying the following equation [77]:

$$\delta_{RI} = 2\frac{\sigma_i \Delta_{RI}}{\Delta I} \tag{3.2}$$

Where σ_i is the maximum standard deviation of the optical power obtained between the both values of concentration (0.01533 dB), Δ_{RI} corresponds to the variation of the RI of both solutions (0.032 RIU), and, ΔI is the mean displacement of output response between the two steps (2.3082 dB). By replacing the values in equation 3.2, the obtained resolution

was 4.25×10^{-4} RIU. It is important to note that this value is greatly influenced by source fluctuations.

3.5 Sensor Based on Multimode Fibre

3.5.1 Fundamentals of Sensor Operation and Design

The sensor design consists of a MMF with a 105 μm core diameter and 125 μm cladding diameter (FG105LVA, 0.10 NA, Thorlabs) with a step-index profile. The RI of the fibre core and cladding is 1.4529 RIU and 1.4440 RIU, respectively. The portion of MMF had a length (L_{MMF}) of 8 mm and was spliced into an SMF, which acted as the input/output of the light as it is represented in Figure 3.6.

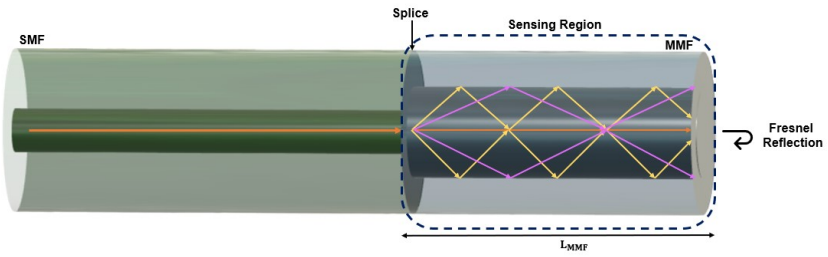

FIGURE 3.6: Schematic diagram of the sensor structure - MMF tip.

The principles of operation of the sensor are based on multimode interference and Fresnel reflection. As mentioned in section 2.3.3, a typical example of a multimode interference-based sensor is an SMS (single mode-multimode-single mode) configuration, which is typically applied in an interrogation system based on the transmission of light. This sensor is similar to the SMS structure, but in this case is studied in a reflection scheme, allowing for the sensing probe to be half of its transmission size. When the light is launched from the SMF into the probe, high-order modes with different propagation constants are excited, which leads to differences in phase between the respective modes. Therefore, by perpendicular cleaving the MMF tip in different lengths, it leads to different field profiles at the end of the probe. Consequently, the coupling between the MMF tip and the input/output of the SMF depends on the length of the probe, the wavelength, among other parameters. In other words, variations of these parameters lead to changes in the reflection spectrum, and can be used for detection of different RI of the surrounding medium of the probe.

The sensor also depends, analogously to the SMF tip, on the Fresnel reflection at the interface between the end of the tip and the surrounding medium with a specific RI.

3.5.2 Experimental Results

The resulting spectra are shown in Figure 3.7 , which were monitored with OSA with a span ranging from [1520,1580] nm. The sensing probe seems to have a well-defined loss peak and a wide passband window. It can be noted that the sensor exhibits a notable change in the amplitude of the optical signal, with higher RI leading to lower optical powers. This behaviour is due to the change of the Fresnel reflection coefficient at the interface of the MMF section and liquid, as expected from Equation 3.1. There are no alterations in wavelength, meaning that the effective RI of the guided modes at the fibre tip does not present changes.

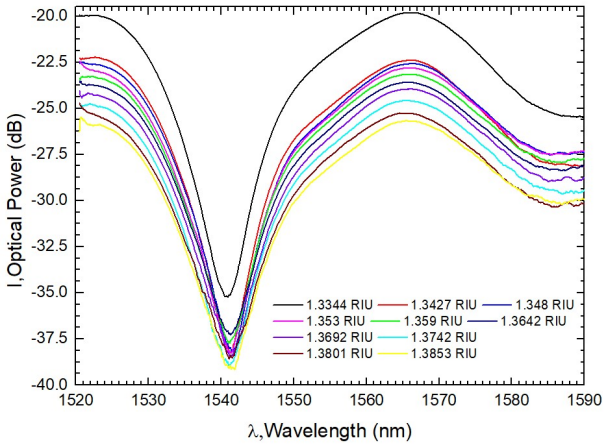

FIGURE 3.7: Output spectra of the MMF tip under different RI solutions.

Figure 3.8a presents the optical power response to the variations of the RI of the surrounding liquid, with the utilized wavelength peak being 1565 nm. The fitting curve, as anticipated from other studies [78, 79], can be described by a second-degree polynomial function, yielding a R^2 of 0.996. To determine the sensitivity of the sensor, the fitting curve was divided into two ranges and a linear approximation was applied. The final results are presented in Table 3.1.

TABLE 3.1: Sensitivity results obtained in the RI experiment.

RI range (RIU)	1.3344-1.3530	1.3590-1.3853
Sensitivity (dB/RIU)	-47±4	-104±5
R^2	0.989	0.993

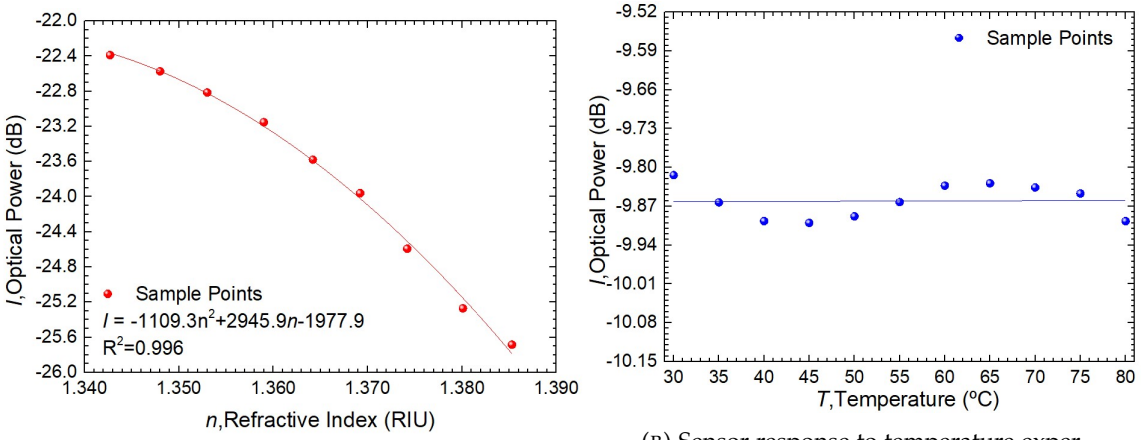

(A) Sensor response to RI experiment.

(B) Sensor response to temperature experiment.

FIGURE 3.8: RI and temperature measurements.

Following the RI experiment, the sensing head response to temperature was also analyzed, with the final result depicted in Figure 3.8b. It can be observed that when it comes to optical power dependence on the temperature, around the same wavelength peak in which the sensor was characterized for RI, the sensitivity is very residual, and the obtained value was of $(5\pm63)\times10^{-5}$ dB/ºC. The cross-sensitivity of the RI and temperature measurements was determined to be 4×10^{-7} RIU/ºC, therefore, it can be neglected when focusing on the region around 1565 nm.

Finally, the sensor was tested for stability and resolution. For the stability test, the probe was immersed for an hour in a solution with a RI of 1.3344 RIU. In the case of the resolution, the probe was immersed for one hour in a solution with the RI of 1.3344 RIU and then, another hour in a solution with RI of 1.3801 RIU. The results are presented in Figures 3.9a and 3.9b. The standard deviation obtained for the stability test was 2.4×10^{-4} dB/min

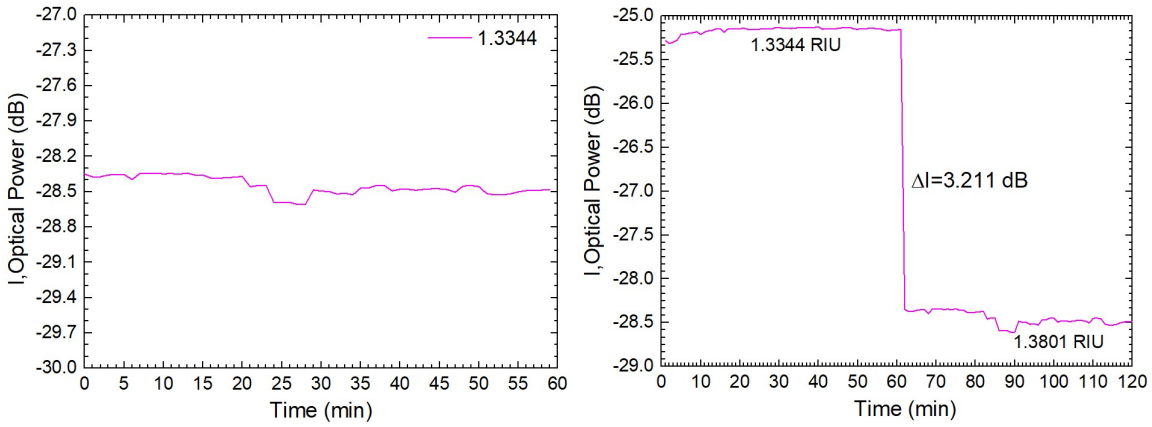

(A) Sensor stability test.

(B) Sensor resolution test.

FIGURE 3.9: Stability and resolution tests.

meaning a stable response of the sensor in terms of time.

For the resolution test, it was applied the equation 3.2, and the minimum value variation of RI that the probe was able to detect was 2.11×10^{-3} RIU.

3.6 Sensor Based on Coreless Silica Fibre

3.6.1 Fundamentals of Sensor Operation and Design

The sensor design, as depicted in Figure 3.10 consists of a CSF with 125 μm diameter (FG125LA, Thorlabs), and a RI of 1.440 RIU at 1550 nm. The portion of CSF with a length of 12 mm, L_{CSF}, was spliced into a SMF, that acted as the input/output light. The operation principles of the sensor are based on multimode interference and evanescent field. As the light propagates from the SMF to the CSF various modes are excited, and interfere constructively and destructively, giving rise to different interference patterns, depending on the length of the CSF portion, similar to the MMF tip presented previously. Upon reaching the interface of CSF-liquid, a small portion of the light is reflected back, in a Fresnel reflection, and conducted back to the SMF.

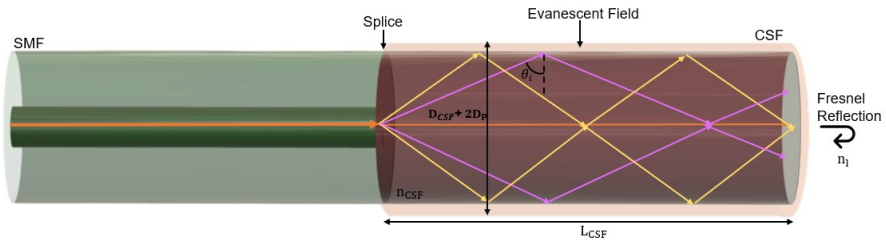

FIGURE 3.10: Schematic diagram of the sensor structure, where n_{CSF} and n_l correspond to the RI of the CSF and of the surrounding medium, D_{CSF} is the diameter of the CSF and D_p is the evanescent field penetration depth.

In addition to the multimode interference, the interaction of the evanescent wave of the CSF tip with the surrounding medium contributes to the sensor sensitivity to external perturbations. This is attributed to the fact that a CSF lacks a solid core, instead it has a hollow region, which is surrounded by a silica cladding. This condition, also makes the CSF more sensitive to mechanical bending, vibrations or pressure compared to the typical optical fibres [80].

From equation 3.3, it can be deduced that as the CSF tip is immersed in the liquids with

higher RI, it leads to a lower difference between RI of the tip and the medium, and therefore, resulting in a higher penetration, D_p, of the evanescent wave [81].

$$D_p = \sqrt{\frac{\lambda_i}{n_{CSF}^2 sin^2\theta_i - n_l^2}} \tag{3.3}$$

Where θ_i is the incident angle at the interface of the CSF and the surrounding medium, and, λ_i is the incident wavelength, which in the case of the optical source used is centered at around 1550 nm. As the RI changes, the evanescent field interaction between the sensing head and the exposed environment also changes, as well as the effective RI of each mode in the CSF. Both of these changes, will give rise to wavelength shifts in the resonant wavelength, which can then be detected and used to measure the RI of the exposed medium.

3.6.2 Experimental Results

In Figure 3.11, the experimental results for the spectra under various RI solutions ranging from 1.3331 to 1.3846 RIU are presented in a wavelength span between [1525,1605] nm. As expected, the sensor exhibits changes in both intensity and wavelength in response to RI variations. It can be confirmed that a higher RI leads to a lower detected optical power and a redshift in wavelength.

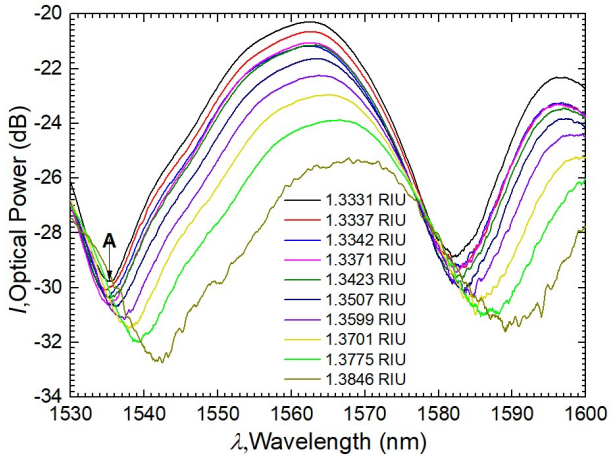

FIGURE 3.11: Output spectra of the CSF tip under different RI solutions.

The focus of this experimental results will be on the wavelength sensitivity rather than the intensity, since it is also affected by fluctuations of the optical source, which might affect the results. To investigate the wavelength sensitivity, a minimum point, denoted as A in the spectra, was selected for studying the shifts of the wavelength.

Figure 3.12a presents the wavelength response of the probe to a range of samples with different RI. It can be concluded a second-degree polynomial fitting curve with a R^2 of 0.993. This non-linear behaviour is expected since from Equation 3.3, the wavelength, λ_i, presents a squared refractive index dependency of the surrounding medium, n_l. Moreover, similar behaviour has been reported in the same RI range [7, 82].

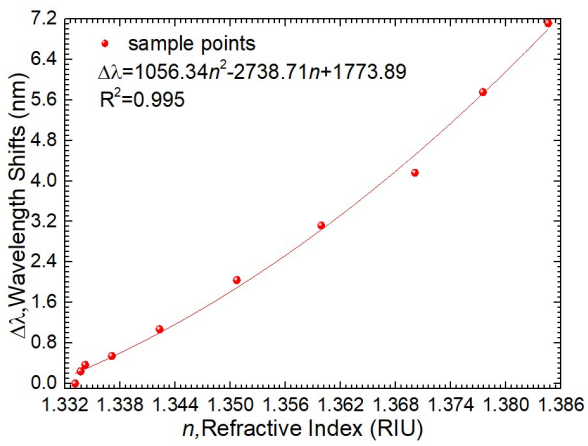

(A) Sensor response to RI experiment.

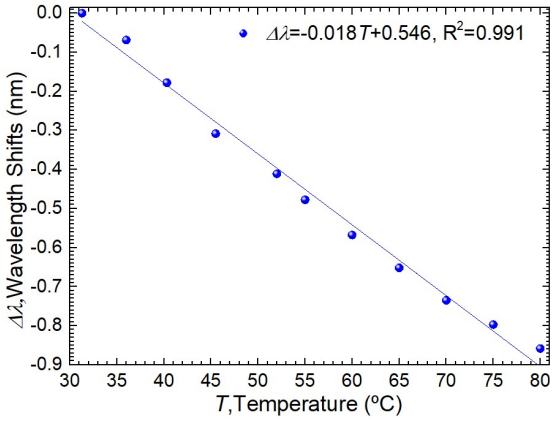

(B) Sensor response to temperature experiment.

FIGURE 3.12: RI and temperature measurements.

To determine the wavelength sensitivity of the sensor, the fitting curve was divided into two distinct ranges. Linear fits were then applied to each range to approximate the relationship between wavelength and the corresponding refractive index. The resulting sensitivities for each range are presented in Table 3.2.

TABLE 3.2: Wavelength sensitivity results obtained in the RI experiment.

RI range (RIU)	1.3331-1.3423	1.3507-1.3846
Sensitivity (nm/RIU)	108 ± 6	164 ± 19
R^2	0.987	0.973

In Figure 3.12b, the behavior of the wavelength as a function of temperature is depicted. When increasing the temperature it can be observed a blueshift of the wavelength, described by a linear fitting. The sensitivity obtained through the slope of the linear fit was (-1.81±0.05)$\times 10^{-2}$ nm/ºC, which was much lower than the sensitivities achieved in the RI sensor response. The sensitivity arises from the thermo-optic coefficient of silica, which causes changes in the refractive index of the coreless fibre, as well as the coefficient of thermal expansion, which results in variations in the length of the CSF section. These changes in length subsequently alter the field profile at the ending of the tip. Given the

negative sensitivity, the dominant temperature effect on the probe can be attributed to thermo-optic coefficient of silica.

Following the RI and temperature experiments, the stability and resolution tests were also performed. During the stability test, the sensor was immersed in a glucose aqueous solution with a RI of 1.3507 RIU for one hour. In the resolution test, two different solutions were utilized. The sensor was immersed in a glucose aqueous solution with a RI of 1.3373 RIU for one hour, and subsequently, another solution with a RI of 1.35507 RIU for another hour.

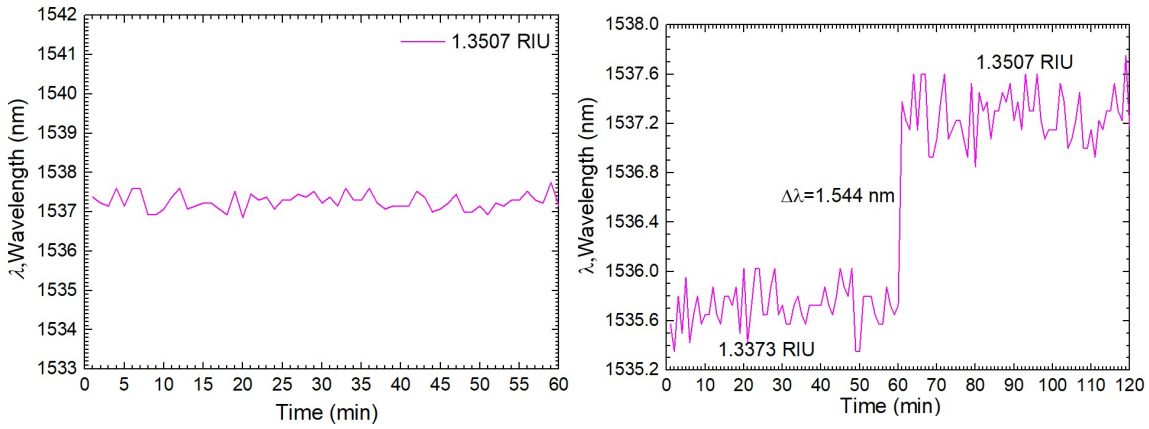

(A) Sensor stability test.

(B) Sensor resolution test.

FIGURE 3.13: Sensor stability and resolution tests.

The obtained results are presented in Figure 3.13a and Figure 3.13b. They showed that the sensor has a good stability with a standard deviation of 1.52×10^{-3} nm/min and a resolution of 3.6×10^{-3} RIU, meaning that this is the minimum variation detectable. The resolution was determined by applying equation 3.2, regarding wavelength variations instead of optical power variations.

3.7 Sensor based on Coreless Silica Fibre and Graded Index Fibre

3.7.1 Fundamentals of Sensor Operation and Design

The sensor design consists of a CSF portion with a diameter of 125 μm (FG125LA, Thorlabs) spliced between a SMF with a diameter of 125 μm , and a GIF (GIF625, 0.275 NA, Thorlabs) with 62.5 μm of core diameter and 125 μm of cladding diameter. The SMF functioned as the optical input and output, as the sensor was interrogated in a reflection

scheme. The splices were performed with a TYPE 81C splicing machine (Sumitomo Electric, Japan). The length of the CSF, L_{CSF}, was 1 mm while the GIF, L_{GIF}, portion was 8 mm, making it a total of 9 mm of the sensing head. The sensor configuration is depicted in Figure 3.14.

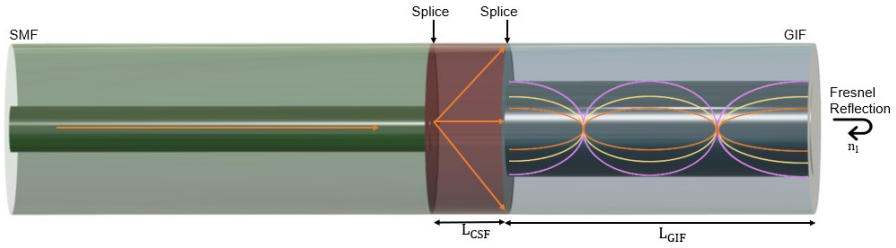

FIGURE 3.14: Schematic diagram of the sensor structure - CSF with GIF tip.

The principle of operation of the sensor is based on multimode interference and Fresnel reflection. As light propagates through the SMF and reaches the CSF, part of the light is reflected back, due to the differences of RI between the core of the SMF and the CSF. Then, part of the light that enters the CSF is excited and several modes propagate in that section and the beam of light is expanded. When entering in the GIF portion, the beam is periodically collimated. This periodic sinusoidal collimation is known as the pitch length, L_p, and can be defined as follows [83]:

$$L_p = \frac{2\pi a n_c}{NA} \tag{3.4}$$

Where it can be concluded a dependence on the: core radius (a) of the GIF fibre, RI of the core center (n_c), and numerical aperture (NA). In this probe, the CSF section acts as a beam expander, allowing to reduce the size of the GIF portion used. At the interface of GIF and external medium, a Fresnel reflection occurs due to RI differences, and part of the light is reflected back onto the sensor.

3.7.2 Experimental Results

Figure 3.15 shows the resulting spectra under different RI solutions between 1.3336 to 1.3806 RIU in a wavelength span of [1540, 1577] nm. The sensor exhibits changes in both wavelength and intensity. As the RI increases, the optical power decreases, and on the other hand, the wavelength displays a blueshift. In this study, similar to the CSF tip in 3.6.2, the focus will be on the wavelength shifts as they are not affected by fluctuations in the optical source. The wavelength shifts were studied around the maximum peak,

labeled as A in Figure 3.15.

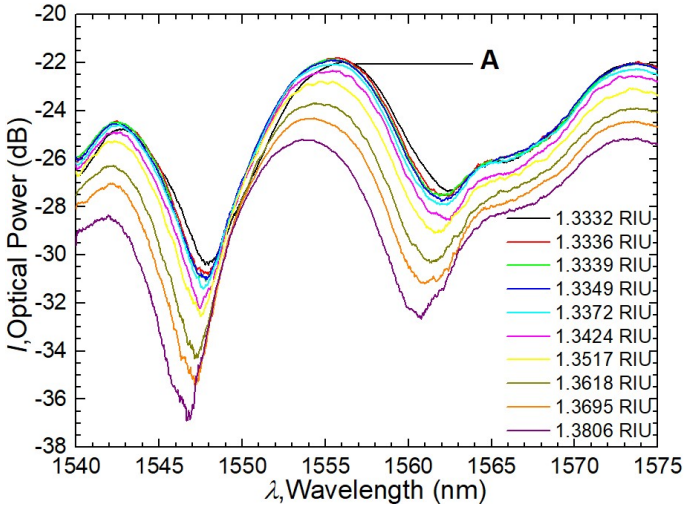

FIGURE 3.15: Output spectra of the CSF and GIF tip under different RI solutions.

The experimental results for the wavelength sensitivity study are presented in Figure 3.16a. It can be noted a linear behaviour of the wavelength as a function of RI with an R^2 of 0.991, and it was obtained a wavelength sensitivity of -82±3 nm/RIU. For the temperature experiment, both increasing and decreasing tests were performed in the same temperature range. The results are presented in Figure 3.16b. By examining the relation-

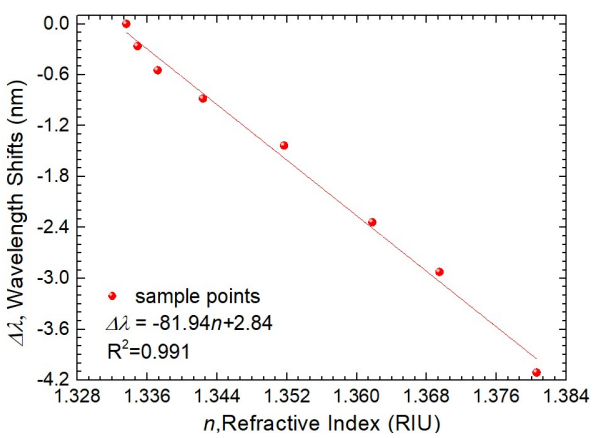

(A) Sensor response to RI experiment.

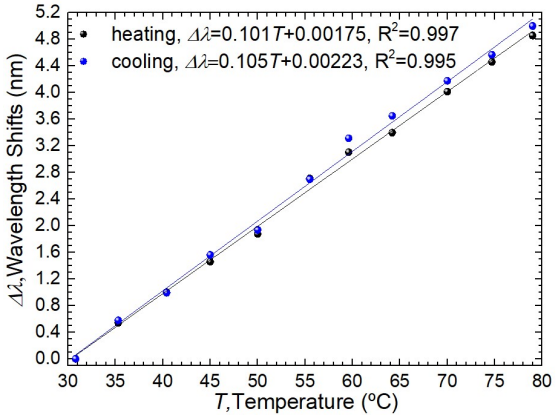

(B) Sensor response to temperature experiment.

FIGURE 3.16: RI and temperature measurements.

ship between wavelength and temperature in both the increasing and decreasing temperature scenarios, we can evaluate the sensitivity of the sensor to temperature changes and also assess any potential hysteresis effects. It can be seen that the fitting behaviour is very similar, with the increase of temperature achieving a sensitivity of 0.101±0.002 nm/°C, and an R^2=0.997, while in the decrease was obtained 0.105±0.002 nm/°C, and R^2=0.995.

Both slopes are positive meaning that the dominant effect is the coefficient of thermal expansion, dependent on the material that constitutes the sensor. The results indicate that the optical properties of the sensor are consistent regardless of the direction of temperature change, and hence, it can be considered a reliable and predictable sensor. In addition, the temperature sensitivity is much lower than the sensitivity presented in the RI study and very similar to other reports [83]. Following the temperature experiment, it was performed stability and resolution tests. For the stability study, the sensor was immersed in a glucose aqueous solution with an RI of 1.3424 RIU for one hour, while in the resolution study, the sensing probe was also immersed in a solution with a RI of 1.3695 RIU. The experimental results are presented in Figure 3.17a and Figure 3.17b.

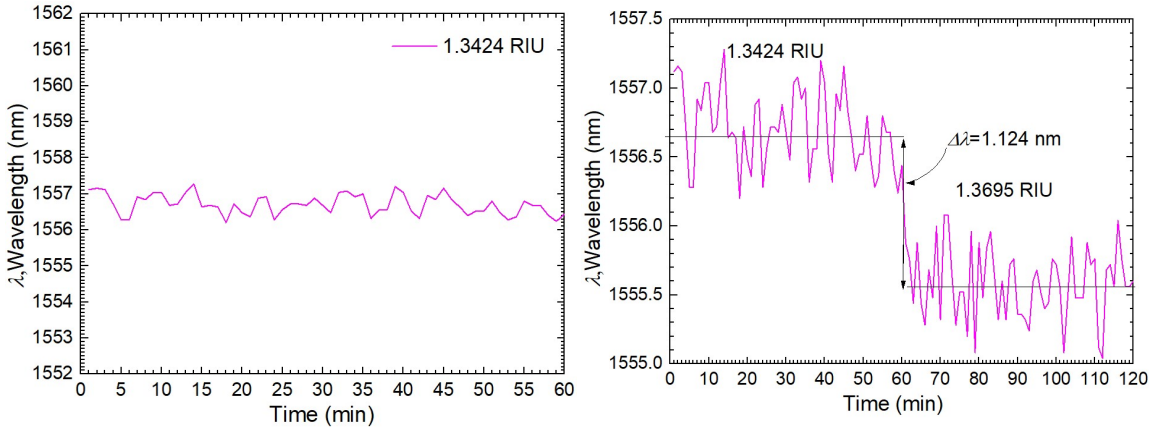

(A) Sensor stability test.

(B) Sensor resolution test.

FIGURE 3.17: Sensors stability and resolution tests.

The stability test provided a standard deviation of 2.4×10^{-3} nm/min, indicating a good stability and consistency. The resolution test was conducted to determine the smallest detectable variation of RI that the sensor could resolve. By applying Equation 3.2 and taking into account wavelength variations rather than changes in optical power, the sensor was found to be capable of discriminating a minimum RI variation of 1.37×10^{-2} RIU.

3.8 Discussion and Concluding Remarks

Through this chapter it was presented four different tips for RI measurements from the simplest to the most complex one fabricated. In the following table is presented a summary of the obtained experimental results for the four tips, as well as the main characteristics of the probes, from the sensor with the highest sensitivity to the lowest.

TABLE 3.3: Summary of experimental results for the different sensing probes.

Configuration	Sensing Length (mm)	Measurand	Range (RIU)	Sensitivity	Stability	Resolution (RIU)
CSF tip	12	RI Temperature (30-80ºC)	1.3330 - 1.3423 1.3507 - 1.3846	108±6 nm/RIU 164±19 nm/RIU (-1.81±0.05)×10^{-2}nm/ºC	1.5×10^{-3} nm/min	3.6×10^{-2}
CSF + GIF tip	1 (CSF)+8(GIF)		1.3336 - 1.3806	-82±3 nm/RIU 0.101±0.002 nm/ºC	2.4×10^{-3} nm/min	1.37×10^{-2}
MMF tip	8		1.3344 - 1.3530 1.3590 - 1.3853	-47±4 dB/RIU -104±5 dB/RIU (5±62)×10^{-5} dB/ºC	2.4×10^{-4} dB/min	2.1×10^{-3}
SMF tip	Not Applied		1.3368 - 1.3836	-82±3 dB/RIU (1.51±0.03)×10^{-2} dB/ºC	1.36x10^{-5} dB/min	4×10^{-4}

It can be concluded that the CSF tip provided the best results for RI sensing, as expected, due to a higher penetration of the evanescent field into the surrounding medium, making it more sensitive to external variations. Although the GIF tip contained a portion of CSF (1mm), the length of this portion is much smaller than the L_{CSF} of the CSF tip, resulting in a lower interaction of the evanescent field with the surrounding medium and, consequently, lower sensitivity. Increasing the length of the CSF in the GIF tip might enhance sensitivity. However, in this sensor, the aim of the portion of CSF was to expand the beam to decrease L_{GIF} and the total length of the sensing head.

Chapter 4

Graphene Oxide Sensor Based on Coreless Silica Tip

4.1 Introduction

In the previous chapter, it was established that the coreless silica (CSF) tip yielded the most promising outcomes for refractive index (RI) sensing. Thus, in this chapter the CSF tip is further explored to optimize the probe. The aim is to establish a proof of concept regarding the applicability of these types of probes to measure glucose concentrations in aqueous solutions from 25 to 200 mg/dl, mimicking the range typically found in human saliva.

Diabetes is a condition that affects people across the globe, and is due to the inability of the human body to process insulin effectively. Hence, the monitoring of glucose levels is crucial to the management of the progression of such diseases. Most glucometers are tested in blood samples, however, previous statistical studies suggest a strong correlation between glucose salivary levels and blood levels [84]. Hence, salivary techniques can be an attractive alternative technology to explore for measuring glucose levels, since they can be easily applied as a noninvasive method.

To understand the sensing potential of the CSF tip, two distinct sensing configurations were developed and subjected to characterization. The initial sensor integrates the principles of multimode interference (MMI) and self-imaging sensing, accompanied by Multiphysics COMSOL 6.0 simulation. Subsequently, the second sensor combines MMI and self-imaging theory with a thin layer of oxide graphene (GO) of 80 μg/ml. This graphene layer is deposited using the layer-by-layer (LbL) technique.

4.2 Fundamentals and Simulation of Sensors Operation

As highlighted in sections 2.3.3 and 3.6.2, the coupling of light from a single mode fibre (SMF) to the multimode CSF leads to the excitation of multiple modes, each propagating with distinct propagation constants. This generates an interference pattern that exhibits sensitivity to external perturbations. When light reaches the CSF-external medium interface it suffers a Fresnel reflection due to the difference of RI between both mediums and a small fraction of the light is reflected. Moreover, as the modes interfere constructively and destructively along the fibre it leads to the periodic formation of self-image points. These self-image points correspond to exact replicas of the input field at the CSF-external medium interface and correspond to lower loss points. Their position, L_{CSF}, can be determined by the following equation [85]:

$$L_{CSF} = p\frac{n_{CSF}D_{CSF}^2}{\lambda_0} \tag{4.1}$$

Where p corresponds to the self-image index, n_{CSF} is the CSF effective RI, D_{CSF} is the CSF diameter and λ_0 is the interference wavelength. To achieve a self-image point the L_{CSF} needs to be very precise, since a small variation in the scale of microns can be enough to lose the self-imaging and only modal interference will be observed. Considering the CSF from Thorlabs (FG125LA, USA) with the following characteristics: $n_{CSF} = 1.4440$, $D_{CSF} = 125 \pm 1/2\mu$m and $\lambda_0 = 1.55\mu$m and Equation 4.1, it can be theoretically determined the L_{CSF} for several p as presented in Table 4.1.

TABLE 4.1: CSF Self-Image Points for different p

CSF Self-Image Points	
p	L_{CSF} (mm)
1	14.56
2	29.12
3	43.68
4	58.24
	...

Additionally, complete immersion of the CSF tip in a liquid results in the cladding RI matching that of the liquid. As a result, the difference between the RI of the core and cladding is reduced compared to when the CSF tip is exposed to air. This reduction leads to a higher penetration of the evanescent field generated at the CSF-liquid interface, increasing the effective RI. By using Equation 4.1, it is possible to conclude that that as the

effective RI increases, while holding other variables constant, the λ_0 value also increases. Therefore, combining the self-image principle with the evanescent field as in Equation 3.3, it is expected that the sensors present shifts in wavelength, on top of the intensity modulation.

Following the calculation of the theoretical points, it was decided to simulate a CSF tip with a length of 29.12 mm, spliced into a SMF which served as the waveguide for the input light. Typically, the second and fourth self-imaging points are better for achieving high-quality self-imaging, as the modes are better focused at these lengths [86]. However the fourth self-image requires a longer length of CSF, making it more difficult to handle and manipulate. Therefore, the simulation will focus on the observation of the first and second point of self-image. The simulation was conducted to visualize the pattern of self-image interference, by using the wave-optics module and the beam propagation method within the COMSOL Multiphysics 6.0 software. Furthermore, the electric field distribution was also studied along the longitudinal and transversal axes. For better contextualization, the simulation specifics are described in Appendix C, including a brief introduction to COMSOL Multiphysics work-flow. In the simulation, the tip was surrounded by an air medium of 1.0003 RIU. The geometry and the RI settings are presented in Table 4.2.

TABLE 4.2: Geometric and RI settings - CSF (FG125LA) and SMF (SM28) from Thorlabs.

Settings	Parameter	Value
Geometry	SMF core	8 µm
	SMF cladding	125 µm
	SMF length	5 mm
	CSF diameter	125 µm
	CSF length	14.56 mm for p =1
		29.12 for p=2
RI	Operating Wavelength	1550 nm
	SMF core RI	1.4529 RIU
	SMF cladding RI	1.4440 RIU
	CSF RI	1.4440 RIU
	Analyte RI	1.0003 RIU

Figure 4.1 presents the final result of the simulation for the light propagation from the SMF to the CSF tip, as well as the electric field throughout the longitudinal axis.

Figure 4.1.(a) depicts the self-image phenomenon along the CSF tip. It is possible to observe that the light is confined in the core of the SMF, and when it reaches the CSF the beam is expanded and an interference pattern is formed. In the interference pattern is possible to observe two bright focused points, which represent the self-imaging points

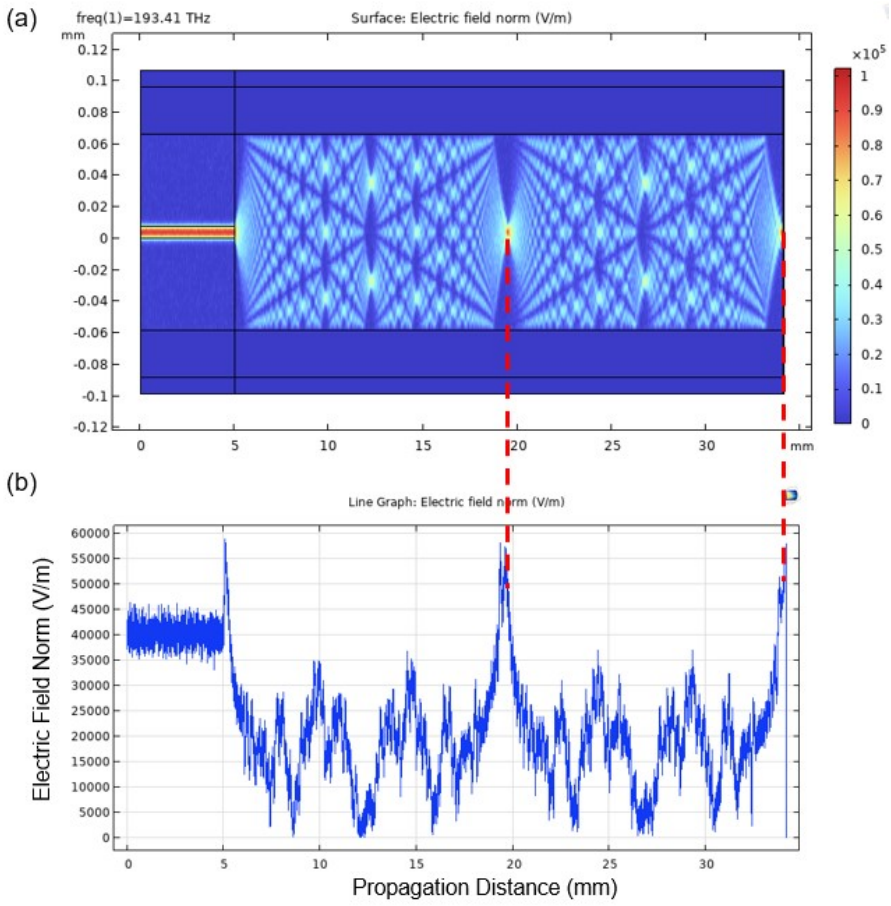

FIGURE 4.1: (a)Light propagation, (b) and electric field distribution (longitudinal) for an CSF tip with a length of 29.12 mm.

for $p = 1$ at 14.56 mm, and $p = 2$ at 29.12 mm, right at the end of the fibre. Hence, it can be deduced that the theoretical values calculated using Equation 4.1, and presented in Table 4.1, align closely with those observed in the simulation. Figure 4.1.(b) presents the distribution of the electric field, revealing two distinct peaks that correspond to the self-image points. These peaks occur due to the electromagnetic beam being concentrated at these specific lengths.

Figure 4.2 presents the transverse electric field at different lengths of the CSF structure. As anticipated, the self-imaging points exhibit a curve identical to a Gaussian fit, closely resembling the field at the entry of the CSF probe, generated through the propagation of an unidirectional electromagnetic beam. The third curve corresponds to the mode field at a CSF length of 8.23 mm, precisely where the observation of two distinct bright points separated by a region of destructive interference is evident in Figure 4.1(a). This alignment translates in the absence of the electric field between the two peaks in Figure 4.2.

Following the results of the simulation and considering that one of the goals for the sensor

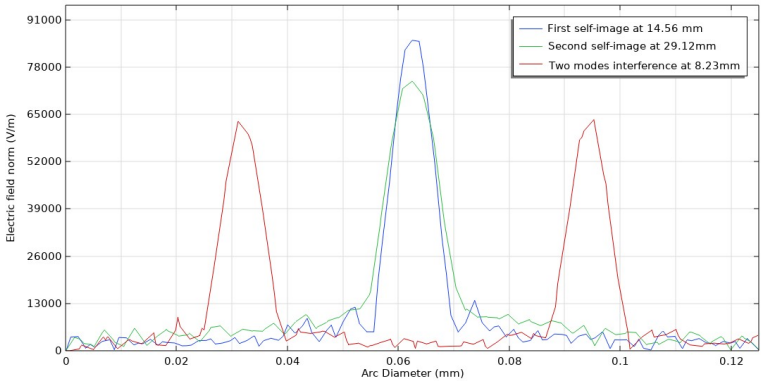

FIGURE 4.2: Mode field distribution at different points of the CSF tip.

is to have the smallest possible length, it was decided to experimentally verify whether the CSF tip with a length of 29.12 mm achieves better results than the one with 14.56 mm, as reported in the literature [86]. Therefore, tips with these lengths were fabricated and tested with glucose aqueous solutions ranging from 25-200 mg/dl, prepared in a laboratory environment. Figures 4.3a and 4.3b present the spectra for both configurations, and in the inset, it is possible to observe the resulting curves regarding wavelength shifts.

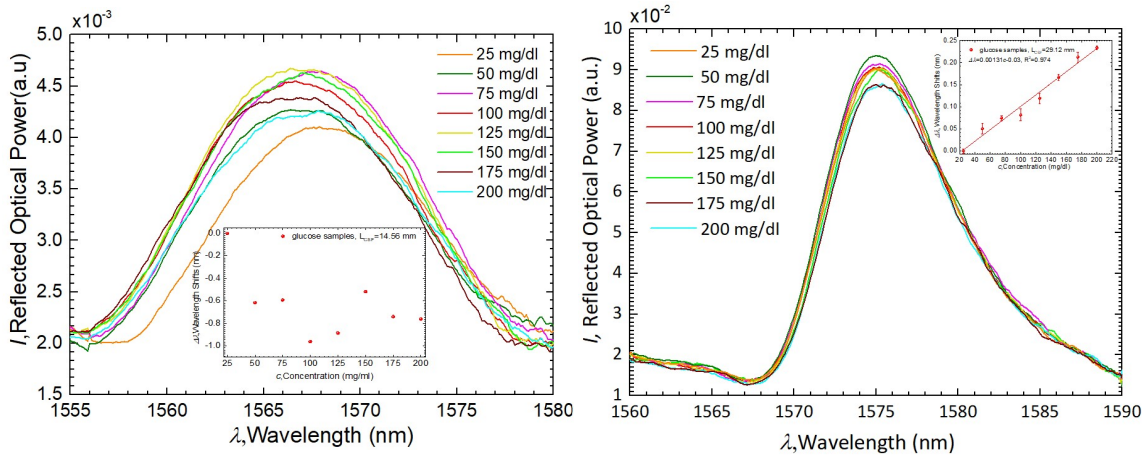

(A) L_{CSF}=14.56 mm.

(B) L_{CSF}=29.12 mm..

FIGURE 4.3: Experimental spectra of the glucose solutions measurement for both CSF tips at different points of self-image.

When comparing both spectra, the peak of self-image is better defined in the tip of length 29.12 mm. Moreover, as seen in the inset graph, it also showed sensitivity to glucose aqueous solutions measurements, whereas in the case of the tip with 14.56 mm length there is a lack of sensitivity. Thus, the fabrication focus will be on CSF tips with a length of 29.12 mm, since it showed better results.

4.3 Sensor Design and Fabrication

The sensor design is depicted in Figure 4.4, and it consists on splicing a CSF (FG125LA, Thorlabs, USA) into a SMF (SM28, Thorlabs, USA). The characteristics of both fibres are the same as the one presented in Table 4.2, which were used for the simulation purposes.

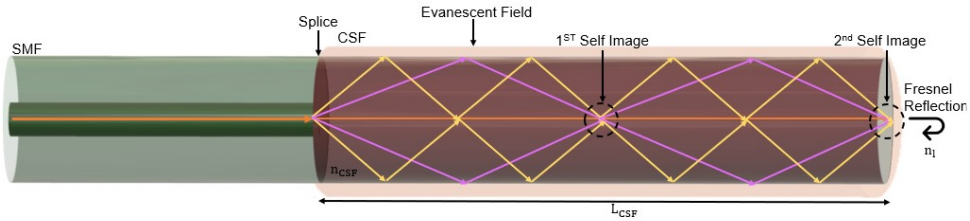

FIGURE 4.4: Schematic diagram of the sensor structure, where L_{CSF} corresponds to the CSF length- image not to scale.

The fabrication process of the tips is described as follows. First, to facilitate the removal of the cladding, the CSF was immersed in a standard acetone solution for one to two minutes. The cladding was then removed with a fibre stripper, and the CSF was cleaned with ethanol. Next, the CSF was perpendicularly cleaved using a cleaver machine and spliced ((Type 82C, Sumitomo Electric, Japan) into the SMF, as mentioned earlier. Finally, to accurately measure the length of the CSF tip, a setup employing a micrometric translation stage was used. This setup was necessary to ensure that the tip would be precisely cut, since even a small variation of microns can lead to the loss of the self-image point. In the setup, described in Figure 4.5, the fibre is clamped between two magnetic bases, ensuring that the SMF-CSF spliced point is aligned precisely with the blade of the cleaver machine (FC-6RS, Sumitomo Electric, Japan).

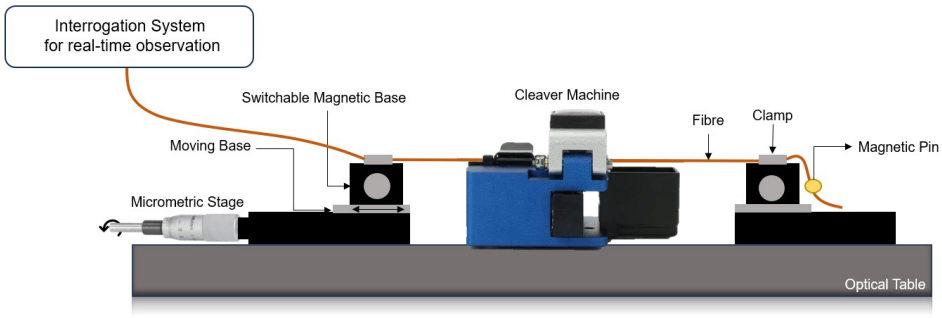

FIGURE 4.5: Schematic configuration of the cleavage setup.

The second clamp secures the end of the fibre between two magnetic pins, ensuring it is under tension. Once the fibre is properly positioned, the micrometric driver is engaged and rotated until the desired length is achieved. As a result, the magnetic base supporting

the fibre also moves. The micrometric driver (151-411ME-H, Thorlabs, USA) used has a travel range of 50 mm, with 10 μm travel per division. It is important to maintain the cleaver machine open before cutting the CSF to facilitate the movement of the fibre.
Several tips with L_{CSF}=29.12 mm were fabricated, and the cleavage process was monitored in real-time with a reflection interrogation system, identical to the one in Figure 3.1. Figure 4.6 shows the spectra of different tips with similar length observed in the OSA .

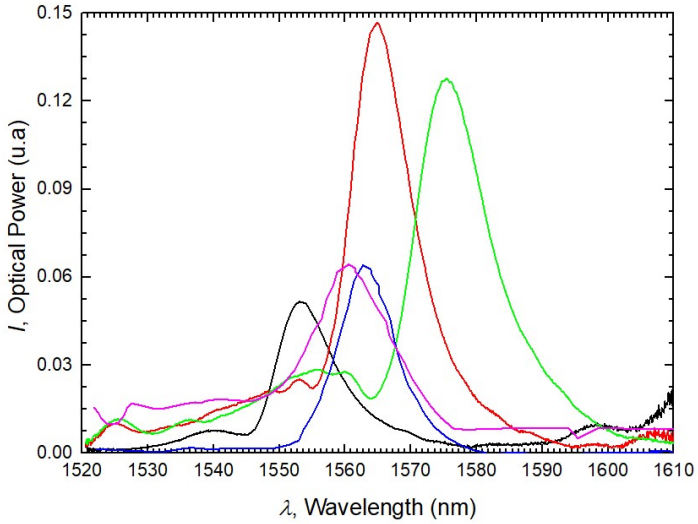

FIGURE 4.6: Experimental spectra of different CSF tips with L_{CSF}=29.12 mm in air.

It is observed that each spectrum has a predominant peak. However, the peaks have different amplitudes and are centered at different wavelengths, due to the limitations of the cleaving process. Among the various tips, the best ones were selected to be applied the LbL technique for GO deposition.

4.4 Graphene Oxide Coating on Optical Fibres

The final sensor configuration corresponds to a CSF tip that relies on self-imaging and multimode interference, incorporating a thin film of GO deposition to enhance the sensitivity of the probe. As mentioned in section 2.3.5, GO offers the advantage of being cost-effective, thereby facilitating the potential commercialization of such sensing heads. Moreover, the presence of carboxyl groups at the edges of GO sheets, along with hydroxyl and epoxy groups within basal planes, allows for effective functionalization of the optical fibre surface, alongside with pronounced hydrophilic properties [87].
The experimental protocol used to deposit GO onto the fibres involves a low-cost thin film

adsorption method known as the layer-by-layer (LbL) technique. The first implementation of this technique traces back to 1965 when J. J. Kirkland and R. K. Iler of DuPont pioneered its utilization using microparticles as described in their work [88]. This method relies on a sequential deposition process involving materials with opposite charges, known as polyelectrolytes, resulting in the formation of a multilayer structure, primarily held together by electrostatic forces [89, 90].

Before starting the LbL method, the tip of 29.12 mm was immersed in 1.0 M of sodium hydroxide (NaOH) to remove any biological residues, and also in order to hydroxylate the surface of the fibre to help promote the adhesion of a polycation. The GO solution was obtained by diluting GO in an aqueous solution and dissolving it with ultrasonic waves for 30 min. The LbL protocol is depicted in Figure 4.7, and is described as follows [91]:

1. The air-dried fibre tip is immersed in a polycationic solution named polyethylenimine (PEI, Sigma-Aldrich P3143) for 30 minutes with a concentration of 80 μg/ml. The PEI solution was diluted in sodium chloride (NaCl) aqueous solution with a concentration of 0.03 g/ml;

2. The probe is rinsed in deionized water to remove any extra compounds or particles and air-dried for 5 minutes;

3. The tip is immersed in the polyanionic solution of GO (Sigma-Aldrich, 777676) with a concentration of 80 μg/ml for 30 minutes;

4. Repeat step 2.

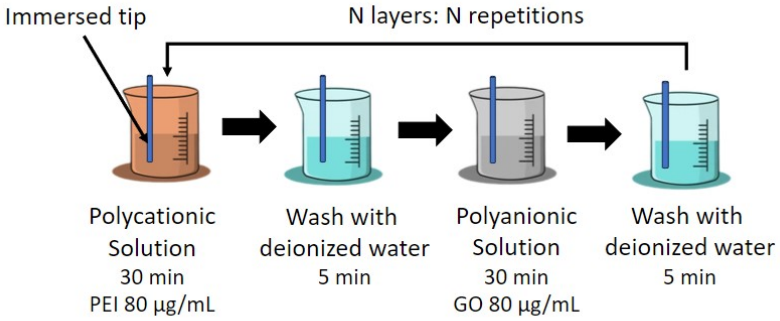

FIGURE 4.7: Description of LbL technique.

The final sensors were fabricated using one bilayer of PEI/GO and the LbL process was continuously monitored in real-time using the OSA. Figure 4.8 presents microscope images obtained with LEICA ICC50W. The images correspond to a CSF tip before and after the LbL procedure.

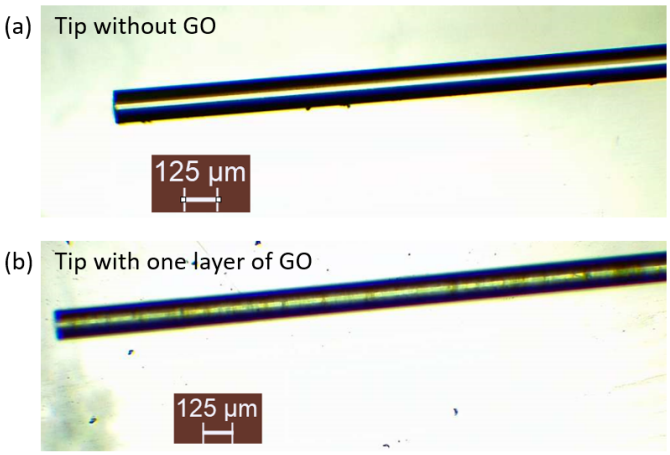

FIGURE 4.8: Microscope images with objective with amplification 4x of CSF tip: (a) without GO; (b) one layer of PEI/GO of 80 μg/ml.

4.5 Experimental Setup and Methodology

The sensors were tested to assess their capability in detecting glucose concentrations within aqueous solutions. Additionally, an experiment involving temperature variations was conducted. The experimental setup for both the glucose concentration and temperature experiments are similar to the configuration depicted in Figure 3.1, as detailed in Section 3.2, concerning the RI measurements.

Glucose aqueous solutions with concentrations ranging from 25-200 mg/dl were prepared through a dilution method, in a laboratory-controlled environment at approximately 21 °C. This range was purposely chosen to mimic the glucose concentration levels found in human saliva. A magnetic stirrer (NAHITA, magnetic stirred, model n°690/1) was used to homogenize the aqueous solutions with glucose (G8270-100g) supplied by Sigma Aldrich. The sensors were immersed in these solutions, and the optical spectra were captured with an OSA. The OSA was configured to operate in a linear scale with a resolution of 0.5 nm. For each measurement the tips were immersed for 150 seconds before processing the respective data.

In the context of the temperature experiment, and in contrast to the temperature experiments performed so far, the response to temperature variations was determined by positioning the sensing probe vertically within a water bath with a starting temperature of approximately 40 ºC. The range under study spanned from 22 ºC to 35 ºC, as this range corresponds to the typical temperature interval for measuring glucose levels in saliva.

4.6 Experimental Results

The CSF tip based on self-imaging with a GO thin film was characterized in terms of RI. The samples used for RI testing were fabricated using a similar protocol as the one presented previously for the glucose samples in Section 4.5. Moreover, the RI of the solutions was determined with an Abbe refractometer (ATAGO, DR-A1). In this case, the final glucose aqueous solutions had a RI ranging from 1.3380 to 1.3853 RIU. In Appendix B is presented an additional study regarding how the concentration of glucose aqueous solutions can be related to the RI, in a similar range. Figure 4.9 presents the final results for the RI characterization, with an inset graph of the resulting spectra.

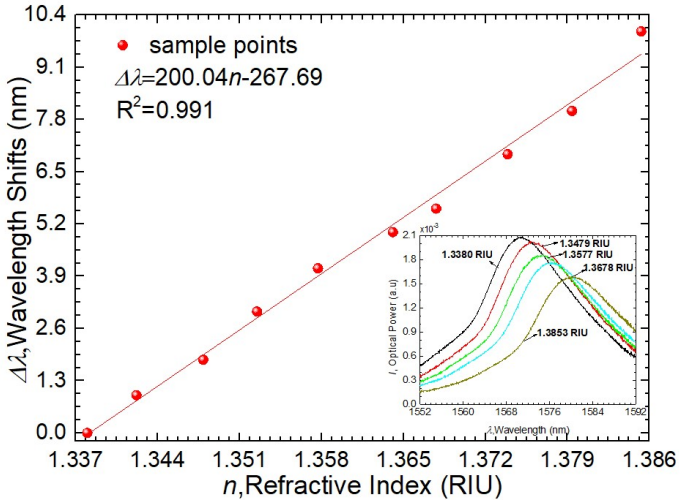

FIGURE 4.9: Sensor response to RI experiment.

The resulting fitting curve can be described by a linear relationship with a correlation coefficient (R^2) of 0.991. In comparison to the previously discussed CSF tip, from Chapter 3, which had a length of 12 mm, there is an improvement of the sensor performance. The former exhibited a total wavelength shift ($\Delta\lambda$) of 7.11 nm, while the current sensing head achieved a $\Delta\lambda$ of 9.99 nm. This translates to an enhancement by a factor of 1.4. Moreover, through the optimization of the length of CSF sensing head, and with the introduction

of a GO thin film, the sensitivity increased, reaching a value of 200 ± 6 nm/RIU. This sensitivity is similar to the one obtained in the work reported in [69], which also operated within a similar refractive index range and GO concentration, but in a transmission interrogation system.

Following the RI characterization, the probe uncoated/coated with GO was tested for the measurement of glucose in aqueous solutions, for comparison purposes. Figure 4.10a shows the resulting spectra under different glucose aqueous solutions ranging from 25 mg/dl to 200 mg/dl, regarding the CSF based GO tip. The spectra is described by a well-defined peak due to the self-image phenomenon. The sensor displays changes in both wavelength and amplitude. As the glucose concentration increases, the wavelength shifts towards the red.

Figure 4.10b presents the resulting fitting curves of the CSF tip with/without a bilayer of PEI/GO regarding glucose concentration variations. As expected, in both sensors it is possible to observe that as the concentration becomes higher, the wavelength peak also increases. It is also noted that the sensor with the PEI/GO layer shows a bigger wavelength variation.

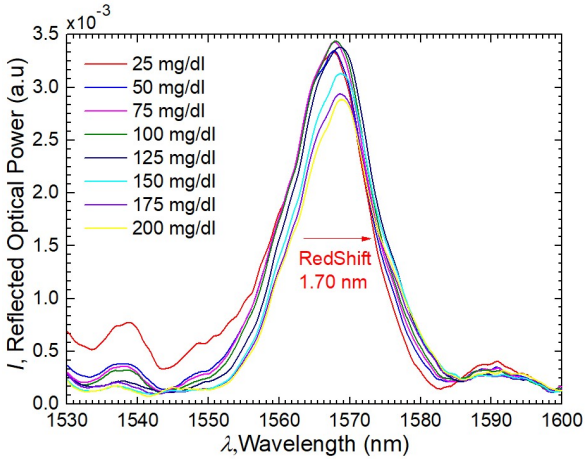

(A) Output spectra of the GO based CSF tip under glucose aqueous solutions.

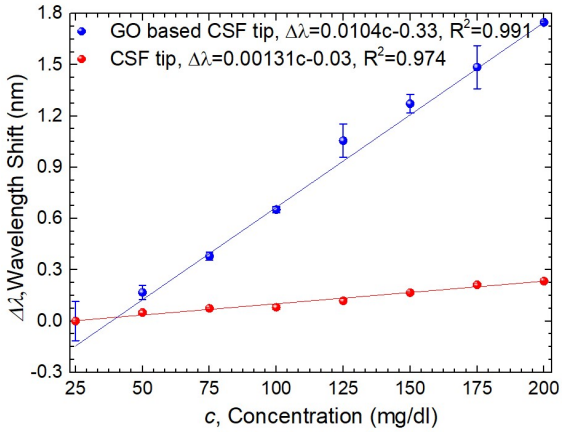

(B) Sensors response to glucose concentration variations.

FIGURE 4.10: Experimental spectra for the CSF based GO tip and glucose solutions measurement for both probes, with and without a GO thin film.

Both fitting curves are described by a linear relationship between the wavelength peaks and the glucose solutions. Overall, for the same range, the PEI/GO based sensor performed better in the glucose study with a $\Delta\lambda = 1.70$nm and a R^2=0.991, while the CSF tip obtained a $\Delta\lambda$=0.23 nm and a $R^2 = 0.974$. Through the slope of the linear equation is possible to determine both sensors wavelength sensitivity. In the case of the GO based

CSF tip it was obtained a sensitivity of $(1.0403\pm0.0004)\times10^{-2}$ nm/(mg/dl), while in the CSF tip it was $(1.31\pm0.08)\times10^{-3}$ nm/(mg/dl). This means that by adding one layer of PEI/GO with a concentration of 80 μg/ml, the final sensitivity of the optimized sensor increased by a factor of 8.

Figure 4.11 depicts the uncoated sensor response to temperature, revealing a residual sensitivity of $(-4\pm80)\times10^{-4}$nm/ºC in the range of 22ºC to 35ºC.

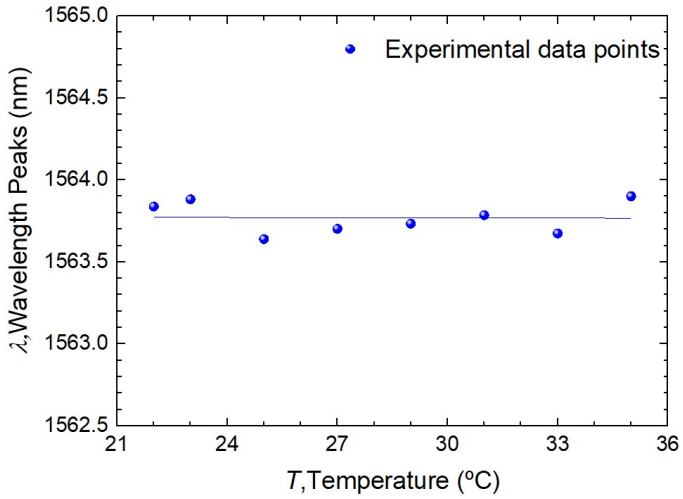

FIGURE 4.11: Sensor response to temperature variations.

In the case of the probe based on GO, a stability test was also performed. In the stability test the sensor was immersed in a glucose aqueous solution with a concentration of 25 mg/dl for one hour. The experimental result is depicted in Figure 4.12. It was obtained a standard deviation of 6×10^{-4} nm/min, meaning that the probe exhibits a good stable response.

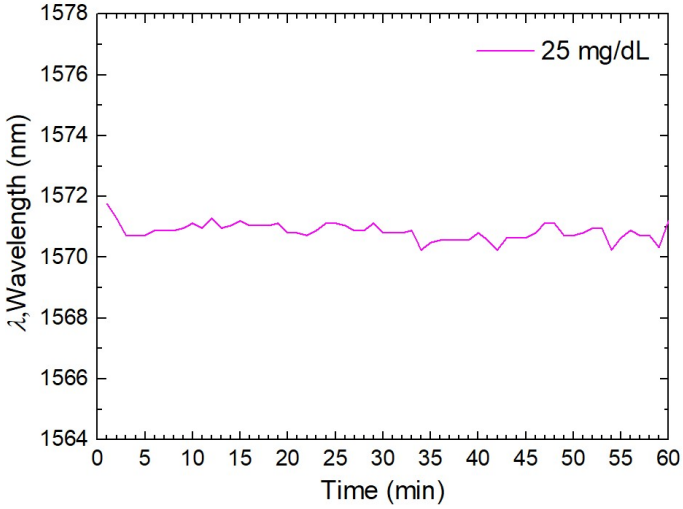

FIGURE 4.12: Sensor stability test.

The maximum theoretical resolution, δ, for both sensors was calculated by taking into consideration the OSA resolution, R_{OSA}, and the sensors sensitivity, S_s, in the following equation [92]:

$$\delta = \frac{R_{OSA}}{S_s} \tag{4.2}$$

For the sensors based on CSF uncoated/coated with GO it was obtained a resolution of 15 mg/dl and 1.90 mg/dl, respectively. Meaning that this values are the maximum theoretical values that both probes are able to resolve.

4.7 Concluding Remarks

This chapter has been dedicated to the development of an optical fibre sensors based on self-imaging and coated with a thin film of GO. The aim of the presented sensors were to non-invasively detecting glucose, ranging from 25-200 mg/dl in aqueous solutions, which closely mimic the glucose concentrations found in human saliva.

With the use of the software COMSOL Multiphysics 6.0, the phenomenon of self-imaging in the CSF fibre was simulated, making it possible to study and observe the self-imaging behaviour, as well as the distribution of the electric field along the probe. The simulation results accurately determined the first two self-imaging length points, which also were well-established with the electric field study. Furthermore, the LbL technique was applied to deposit PEI/GO bilayers onto the CSF sensing head.

The CSF GO-based sensor showed an improvement regarding RI characterization, compared to the CSF sensing head presented in the Chapter 3, and achieved a sensitivity of 200 $\pm$ 6 nm/RIU. Moreover, it showed a better performance in the proposed range for the glucose concentration detection, when compared with the CSF tip based solely on self-imaging and MMI principles, which obtained a sensitivity of $(1.31\pm0.08)\times10^{-3}$ nm/(mg/dl). The GO-based sensor obtained a final sensitivity of $(1.0403\pm0.0004)\times10^{-2}$ nm/(mg/dl), meaning that the sensitivity of the sensor was enhanced by a factor of 8.

In summary, the results presented in this chapter, emphasize an enhancement of the probe sensitivity due to the combination of self-imaging theory and GO integration. This shows

the applicability of this types of sensing heads for non-invasive glucose detection methodologies. Comparing the proposed sensor to others is challenging due to the limited availability of reported work using this specific design for this particular glucose range, and especially within an interrogation system based on reflection.

Chapter 5

Transmissive Plasmonic Gold (Au) Sensor Based on Unclad Fibre

5.1 Introduction

Surface plasmon resonance (SPR) based sensors have gained significant attention in recent years for their potential in biochemical sensing due to their built-in benefits, such as high sensitivity, selectivity, and real-time testing capabilities [93, 94].

This chapter focuses on the implementation of a transmissive plasmonic sensor based on an unclad optical fibre. Similarly, to the previous chapter, the final aim of the probe is to detect the concentration of glucose aqueous solutions ranging from 25 to 200 mg/dl. The theoretical background of this type of sensor is presented first, underling the principles of SPR. Next, the fabrication of the sensor is detailed, and the step-by-step process of functionalization involving glucose oxidase (GOx) is described. Following the fabrication, the chapter presents a refractive index (RI) characterization prior to the functionalization of the sensor.

Finally, the chapter concludes with the glucose concentration testing using the optimized sensor and the final results are presented.

5.2 Fundamentals of Sensor Operation and Design

As mentioned in Section 2.3.4, Surface Plasmon Polaritons (SPP), also commonly referred to as surface plasmons (SP), correspond to the oscillations of free electrons within a metal that are confined to the interface between the metal and a dielectric. These oscillations can

be interpreted as an electromagnetic wave, in which the electric field exponentially decays and reaches a maximum at the metal-dielectric interface. The description of SP can be derived from electrodynamics, specifically through the application of Maxwell Equations for the interaction between metals and electromagnetic fields. By solving Maxwell Equations, it is possible to determine the propagation constant of the surface plasmon wave (K_{sp}), which is given by the following dispersion relation [95]:

$$K_{sp} = \frac{w}{c}\left(\frac{\epsilon_m \epsilon_d}{\epsilon_m + \epsilon_d}\right) \tag{5.1}$$

Here, ϵ_m and ϵ_s represent the dielectric constants (or relative permittivity) of the metal layer and the dielectric medium, respectively, whereas w represents the frequency of the incident light, and c is the velocity of light.

Surface plasmons are transverse-magnetic (TM) polarized meaning that they can be excited by a p-polarized light. This excitation occurs when the wave vector of the incident light (K_{inc}) along the metal-dielectric interface is equal to the wave vector of the SP wave - this condition, $K_{sp} = K_{inc}$, gives rise to a phenomenon known as surface plasmon resonance (SPR).

In the presented sensor, the SP excitation is achieved through the waveguide-based method. By using a waveguide such as the optical fibre, the propagation of light is based on total internal reflection, explained in section 2.2 and described by Equation 2.1. Then, an evanescent field is created at the interface of the metal-optical fibre and excites the SP by penetrating the metal layer, the evanescent wave vector, K_{ev}, is then described by [95]:

$$K_{ev} = \frac{w}{c}\sqrt{\epsilon_f} sin\theta \tag{5.2}$$

When the wave vector of the evanescent wave matches the one of SP, $K_{ev} = K_{sp}$, the resonant condition can be mathematically described by the following equation:

$$\sqrt{\epsilon_f} sin\theta = \sqrt{\frac{\epsilon_m \epsilon_d}{\epsilon_m + \epsilon_d}} \tag{5.3}$$

Where ϵ_f corresponds to the dielectric constant of the waveguide and θ is the angle of incidence of light. Note that, for the previous condition to occur, ϵ_f should be higher than ϵ_d, i.e, the RI of the waveguide should be higher than the RI of the dielectric external medium, and since $\epsilon_m < 0$; for some value of angle greater than the critical angle, the Equation 5.3 is satisfied. In addition, when working at optical frequencies, it is possible to consider $\epsilon_d = n_d^2$, where n_d represents the refractive index of the dielectric medium. Therefore, it

can be concluded that alterations in the local refractive index of the surrounding medium can be detected using the SPR phenomenon.

In the case of an optical fibre coupled SPR sensor, the metal layer should be coated onto an unclad region of the optical fibre to enhance the strength of the evanescent field and increase the depth of penetration. This excitation at a specific wavelength leads to the transfer of energy from incident photons to surface plasmons, resulting in a reduction in the energy of the transmitted light in the waveguide. In addition, the metal layer should be thin enough, in the nanometric scale, so that the evanescent wave penetrates through the metal onto the dielectric medium, making it sensitive to external perturbations.

The coupling between the evanescent field and the surface plasmon depends on factors such as the wavelength of light, fibre parameters and geometry, and properties of the metal layer. For instance, an unclad fibre exhibits a greater depth of penetration of the evanescent field compared to a fibre with cladding. Additionally, the numerical aperture (NA) of the fibre is directly related to the maximum acceptance angle of light. A higher NA enables support for more propagating modes, which in turn leads to more reflections directly influencing the SPR curve.

It is worth mentioning that in comparison to the most conventional configurations of SPR, namely, the prism-based SPR sensors, optical fibre based SPR sensors offer an easier tuning and smaller bulk size, while maintaining a similar sensitivity [33].

5.2.1 Sensor Fabrication

The sensing device consists of a large diameter step-index multimode fibre functionalized with Au coating. Two distinct silica fibres were used, with core diameters of 400 and 600 μm, respectively, (FT400ETM and FT600EMT, Thorlabs, USA, 0.39 NA), with a maximum attenuation of 10 dB/km at 800 nm. To prepare the fibres, a 150 mm portion of the optical fibre was cut, and 30 mm of the hard polymer cladding (Tefzel) with 25 μm of thickness was stripped at both ends of the fibre using a blade. In the middle section, 10 mm of the cladding was removed and the stripped part was cleaned with ethanol to remove any cladding remnants. An optical microscope inspection was also done to ensure the cladding was taken off.

5.2.1.1 Au Deposition

Following the previous preparation, in the 10 mm unclad region of the fibre a coating of Au was deposited. The deposition of the Au nanocoating was performed using a sputter coated (LEICA EM SCD500), as shown in Figure 5.1. The coater worked by bombarding an Au target with ions, with the distance between the optical fibre to the target being approximately 50 mm. The coating process was carried out inside a chamber at a pressure of around 10^{-2} torr, a current of 10.25 mA, and a voltage of 1.2 kV. Each side of the fibre was subjected to 80 seconds of Au deposition. For the end parts of the fibre, carbon tape was used to prevent the deposition of Au in those regions. Finally, the Au-coated fibre was annealed in a thermal chamber at 180ºC for 2 hours. The annealing process is helpful to increase the adhesion of the Au thin film to the silica surface and enhance the efficiency of the fibre for biosensing purposes [96].

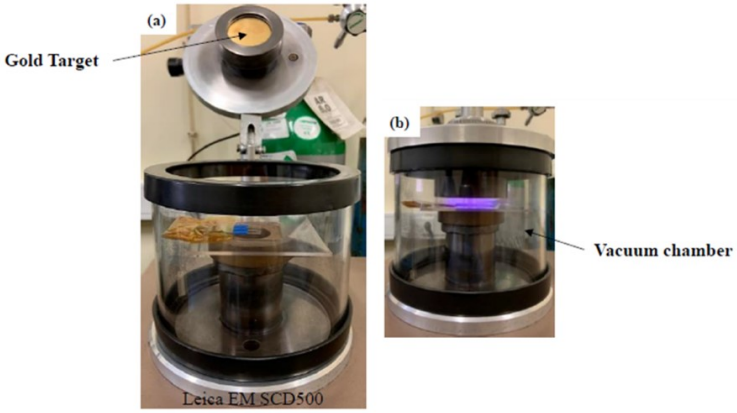

FIGURE 5.1: Pictures of (a) the Au sputter-coater, where fiber tips are placed horizontally inside the vacuum chamber, (b) the sputtering process..

5.2.1.2 Characterization of the Au Coating

Following the deposition of the Au onto the probe, it was performed a morphological and topography characterization with *Scanning Electron Microscopy* (SEM) technique to assess the homogeneity and thickness of the Au coating. The SEM images were acquired using the TESCAN Vega3 SB equipment available at the Physics Department of the University of Aveiro, in secondary electron mode with a high voltage of 15.0 kV. Figure 5.2 presents the acquired SEM images of the Au tip after thermal annealing. The Au film appears to have a homogeneous and smooth deposition with a final thickness of approximately 55 nm.

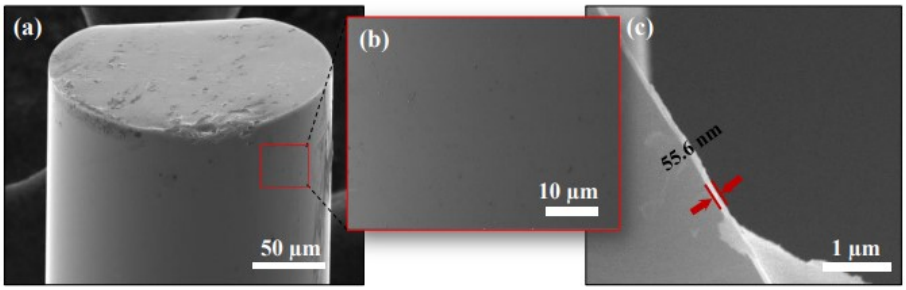

FIGURE 5.2: SEM images of an Au tip after thermal annealing .

5.2.1.3 Functionalization of the Sensor

In optical biosensors based on plasmonic sensing the process of functionalization of the sensor is crucial to help increase the sensitivity and selectivity of the probe. Therefore, the functionalization process involved an enzyme with a strong affinity to the glucose molecule known as glucose oxidase (GOx). The GOx is an enzyme that is covered with carbohydrate chains in the superficial layers, whereas inside the shell contains active sites where glucose binds, as in a deep pocket. There are different ways to immobilize the GOx onto the sensing surface such as: covalent binding [97], gel embedding [98], and chemical cross-linking [99]. Overall, covalent binding allows a stable covalent bond between the enzyme and the support material leading to a good stability and high activity of the enzyme. On the other hand, gel embedding physically traps the enzyme within the gel matrix and preserves the enzyme activity, which leads to a high activity, and chemical cross-linking creates covalent linkages between the enzyme molecules or the enzyme and the support material, leading to a good stability. In this study, the covalent binding was the chosen method as it provides a high activity of the enzyme, as well, as good stability. Typically, the covalent binding process occurs with the mediation of reactive groups between the metal surface and the enzyme, such as amino groups (-NH2) or carboxyl groups (-COOH). The chemical reaction between GOx and glucose is defined as follows:

$$C_6H_{12}O_2 + O_2 + H_2O \xrightarrow{GOx} C_6H_{12}O_7 + H_2O_2 \tag{5.4}$$

In this process, the GOx acts as a catalyst facilitating the oxidation of the glucose ($C_6H_{12}O_2$) in the presence of oxygen and water (O_2, H_2O) into gluconic acid ($C_6H_{12}O_7$) and hydrogen peroxide (H_2O_2). More specifically, the catalyst reaction arises from a compound known as FAD (flavinadenine dinucleotide) which is inside the active site of the GOx and combines with the glucose. In the optical sensing context, as the glucose concentration

increases, the FAD decreases, leading to a reduction of the GOx activity. This reduction causes a change of the RI right next to the surface coated with the enzyme, and consequently it is possible to observe alterations in the experimental spectra wavelength.

The process of functionalization of the probe with GOx follows an identical protocol as the one presented in [6], and it is mainly divided into two steps. The first step corresponds to building a connection between the GOx and the Au surface, through an amination process. For this purpose, the probe was cleaned 3 times with deionized water and was air dried. Afterwards, the sensor was immersed in a solution of 10 mM of MEA (mercaptoethylamine, molecular formula: $NH_2 - CH_2 - CH_2 - SH$, M6500-25G, Sigma-Aldrich) for 10h. In this process, the MEA molecule connects to the Au surface through the -SH (mercapto) group. Between the first and the second step of functionalization the probe should be once again cleaned with deionized water to remove any MEA molecules that have not been bounded to the probe. Finally, in the second step, the sensor was immersed in the GOx (G2133-50KU, Sigma-Aldrich) solution prepared with sodium acetate buffer with a concentration of 15 mg/mL for 10h. This time was chosen due to the reported work in [6] which studied different times (2h,5h,10h) and concluded that this was the optimal time. Figure 5.3 presents a summary of the steps of the fabrication of the sensor, including the final design.

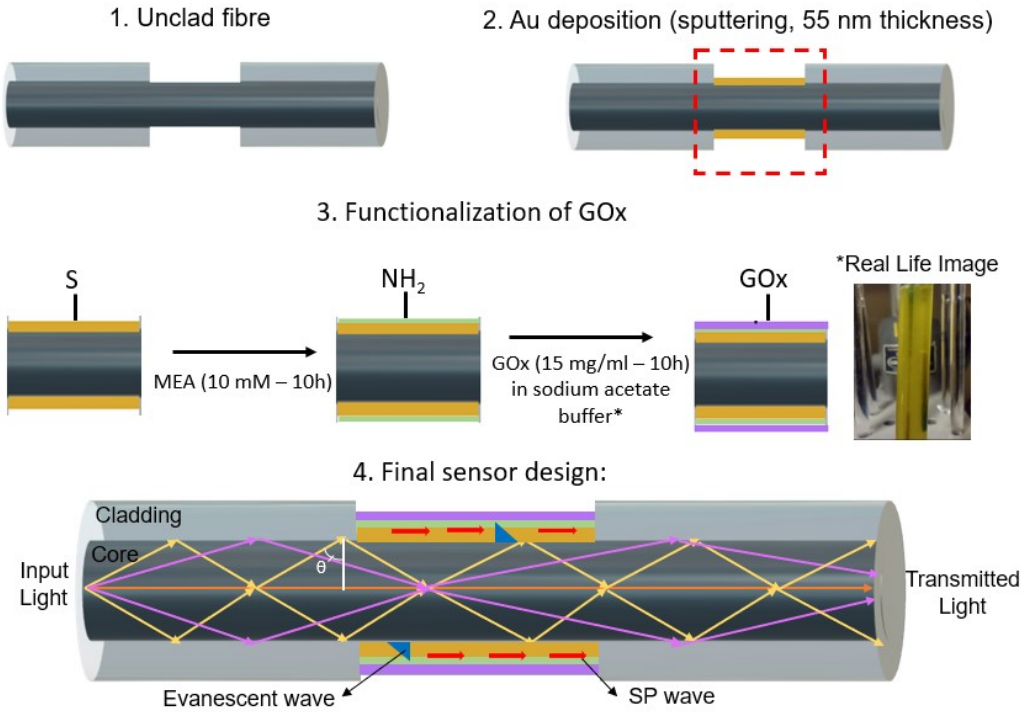

FIGURE 5.3: Fabrication steps of the Au sensor, including the final design.

5.2.2 Experimental Setup

The experimental setup is depicted in Figure 5.4. The sensor was placed in a small container of Acrylonitrile butadiene styrene (ABS) with dimensions of 10×16×8.42 mm. The transmission interrogation system consisted of SMA-terminated patch cables connecting in-line the halogen light source (Tungsten Halogen Light Source, wavelength between 300-2500nm, manufactured by Sarspec, Portugal) and a spectrometer from Ocean Optics (USB4000, detection range of 200 to 1100 nm) with an optical resolution of 10 pm, to both ends of the probe. The spectrometer was connected to a computer, and by using the software SpectraSuite the SPR signature was visualized and processed in real-time. In the SpectraSuite software it was set an integration time of 70 ms and an average of scans of 7. The normalization of the signal was performed by taking into consideration the reference spectrum to standardize the optical transmission spectra with air as the surrounding medium in addition to the dark spectrum to eliminate electronic noise. This setup ensured the sensor robustness as well as the stability of the fibre inside the liquid.

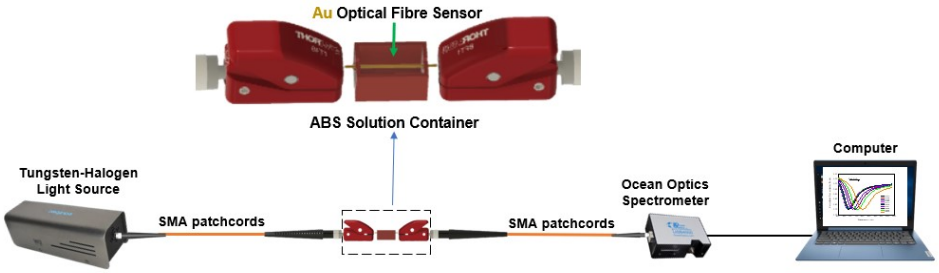

FIGURE 5.4: Schematic configuration of the experimental setup - image not to scale.

5.3 Experimental Results

5.3.1 Refractive Index Characterization

To assess the quality of the Au layer deposition on the sensors before functionalization, it was performed a characterization in terms of refractive index (RI) using glucose aqueous solutions. The same test was applied to different unclad fibres with core diameters of 400 μm and 600 μm, to verify which ones had the best response. The glucose monohydrate (Sigma-Aldrich) solutions were prepared in a laboratory-controlled environment at approximately 22ºC through a dilution process. The concentration of the solutions ranged from 0.0001 g/ml to 0.5000 g/ml, corresponding to a RI range of 1.3332 RIU to 1.3806 RIU.

The RI of these solutions was determined using an Abbe refractometer (ATAGO, DR-A1) to measure the samples. During the measurements, the sensors were immersed in the ABS solution container. After each measurement, the sensing region would be cleaned three times with deionized water for one minute each. Subsequently, the sensors were immersed in the testing solutions for 150 seconds to allow the signal to stabilize [6].

Figures 5.5a and 5.5b present the spectra response of the sensors of each diameter. Based on the analysis of the obtained spectra, it can be concluded that the positions for both SPR signals undergo a redshift as the RI values increase. The total resonant wavelength shift, $\Delta\lambda_p$, regarding the 400 μm sensor corresponded to 117.2 nm, whereas in the case of the 600 μm sensor the $\Delta\lambda_p$ increased slightly to 125.8 nm.

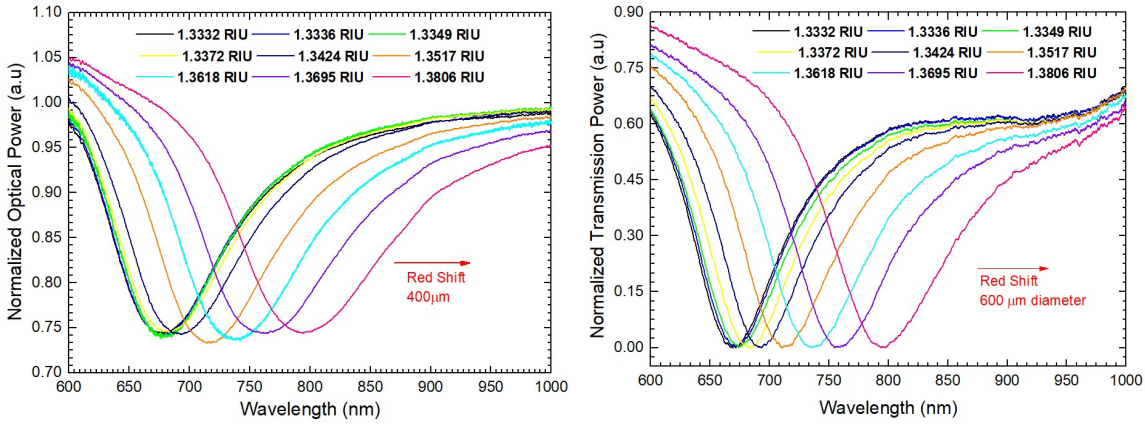

(A) Au sensor of 400 μm core diameter.

(B) Au sensor of 600 μm core diameter.

FIGURE 5.5: Output spectra response of the Au sensors to the RI experiment.

Figure 5.6 shows the corresponding fitting curves of both sensors. In both cases, it is possible to conclude a non-linear relationship between λ_p and RI, described by a second-degree polynomial function, and a determination coefficient (R^2) of 0.998. The wavelength sensitivity was determined by dividing the fitting curve into two linear ranges. The resulting sensitivities for each range and sensor are provided in Table 5.1, along with their corresponding R^2 values. It can be concluded that the 600 µm sensor has a higher sensitivity overall, especially in the lower range of RI (1.3332-1.3424 RIU). For the higher range (1.3519-1.3806 RIU), the sensitivities were similar when considering the standard deviation. However, due to the unavailability of this type of fibre in the laboratory, it was decided to focus on developing sensors with optical fibre of 400 µm diameter. The results also exhibited sensitivities and experimental curves similar to those reported in [100] and [101], within the same ranges, and based on unclad multimode fibre with Au coating.

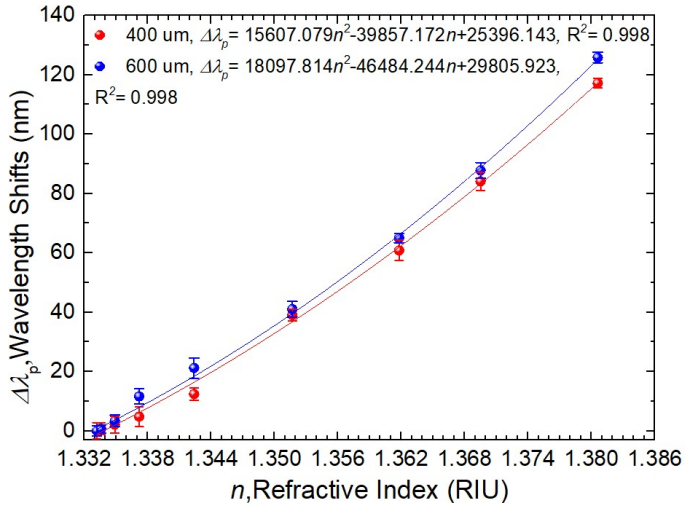

FIGURE 5.6: Comparison of Au sensors response to RI variations with different core diameters.

TABLE 5.1: Wavelength sensitivities results obtained in the RI experiment.

RI range (RIU)	1.3332-1.3424	1.3519-1.3806
400 μm Sensitivity (nm/RIU)	1339 $\pm$34	2723$\pm$100
R^2	0.998	0.997
600 μm Sensitivity (nm/RIU)	2449$\pm$197	3041$\pm$179
R^2	0.990	0.993

The stability and resolution tests were also performed on the Au sensor with 400μm diameter. The stability test was studied with the sensing region being immersed in a solution with RI of 1.3695 RIU for 1h, while being monitored in the OSA. It was obtained a standard deviation of 1.7×10^{-2} nm/min, meaning a good stability. In the case of the resolution test, the probe was immersed in the previous solution, analogue to the stability test, and in another solution with RI of 1.3424 RIU for one more hour. The resolution was calculated with the Equation 3.2, presented in section 3.4.1, and was obtained 2.6×10^{-3} RIU, being the minimum variation of RI that the sensor could discriminate. The experimental results are presented in Figures 5.7a and 5.7b.

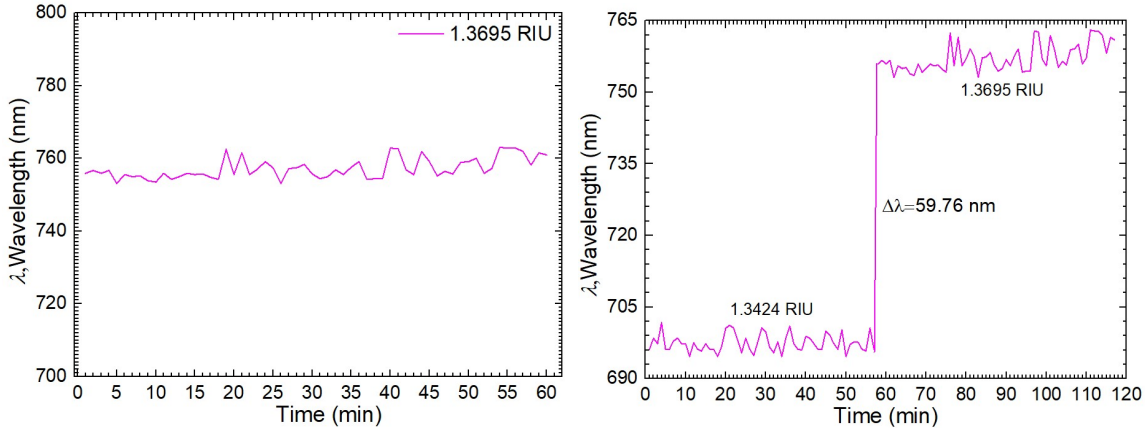

(A) Sensor stability test.

(B) Sensor resolution test.

FIGURE 5.7: Stability and resolution tests.

5.3.2 Glucose Solutions Measurement

Following the RI characterization of the Au sensors, the sensors with the best responses were functionalized and were tested for aqueous glucose solutions with concentrations ranging from 25-200 mg/dl. Between each measurement the sensors would be cleaned with deionized water for 1 minute each and would be immersed in the testing solution for 150 seconds. Figure 5.8a presents the resulting spectra of the Au based sensor after the functionalization, and a redshift of the characteristic SPR curve is observed. Figure 5.8b depicts the fitting curve of the wavelength resonant peaks as a function of the glucose aqueous samples, after the GOx immobilization.

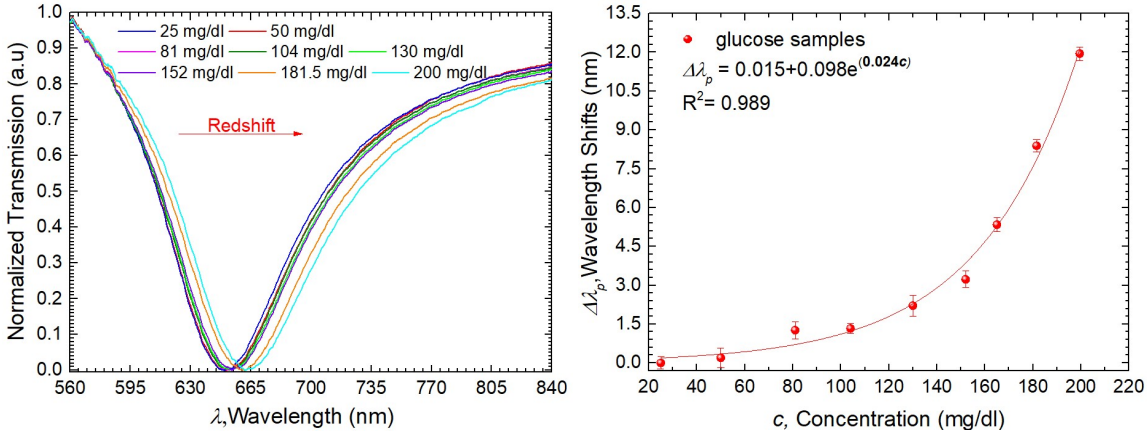

(A) Output spectra response of the Au functionalized sensor in the glucose study.

(B) Au functionalized sensor response to glucose concentration variations.

FIGURE 5.8: Experimental spectra for the functionalized Au/GOx probe and glucose solutions measurement.

The sensor shows sensitivity to the testing range and is described by an exponential curve

with a $R^2 = 0.989$. The sensitivities of the functionalized probe were estimated by dividing the test range into two linear ranges. In Table 5.2 the final results are presented.

TABLE 5.2: Wavelength sensitivities results obtained in glucose aqueous solutions measurements.

Glucose aqueous solutions range (mg/dl)	25-130	152-200
Sensitivity (nm/(mg/dl))	0.021±0.003	0.184±0.005
R^2	0.951	0.998

While the sensitivity of the presented sensor is lower compared to some recent reports, its crucial to consider that those studies involved sensors with U-shaped or tapered configurations which exhibit fragility, making it a disadvantage. Comparing configurations, a similar probe with a comparable transmission interrogation system and detection range reported in 2012 achieved a sensitivity of 0.0366 nm/(mg/dl) but employed a different immobilization process [102]. Meaning that the process of functionalization in plasmonic biosensors play a crucial role in enhancing sensor performance, with the potential to lead to different outcomes by altering the process itself.

The stability of the sensing head was also studied. In this case, the sensor was immersed for one hour in a glucose aqueous solution with a concentration of 200 mg/dl.

The experimental results are represented in Figure 5.9. It can be concluded a standard deviation of 1.2×10^{-2} nm/min, meaning that the sensor offers a good stable response.

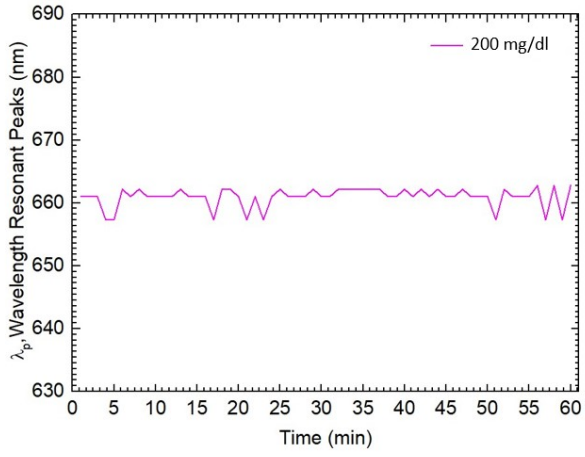

FIGURE 5.9: Au sensor stability test.

The maximum theoretical resolution, δ, was calculated by following Equation 4.2 for each

range. In this case, instead of the resolution of the OSA, it was substituted by the resolution of the Ocean Optics spectrometer. The maximum theoretical values obtained for [25,130]mg/dl and [152,200]mg/dl were 4.76 mg/dl and 0.54 mg/dl, respectively.

5.4 Concluding Remarks

To summarize, this chapter introduced a plasmonic Au sensor based on an unclad multimode fibre. First, multiple similar sensors were characterized for RI measurements, in order to identify the most responsive ones. Given that the experimental curve exhibited characteristics of a second-degree polynomial, the testing range was divided into two linear ranges. Within the [1.3332,1.3424] RIU range, the resulting sensitivity was 1339$\pm$34 nm/RIU, while in the [1.3519,1.3806] RIU range, it was 2729 $\pm$100 nm/RIU.

The final goal of the sensor was to detect glucose concentrations in aqueous solutions within the range of 25 to 200 mg/dl. To achieve this, the sensor underwent a functionalization process involving the immobilization of glucose oxidase (GOx), in order to enhance its sensitivity. The response of the sensor to glucose aqueous measurements was described by an exponential fitting curve. Once again, the testing range was divided into two sections, with linear fitting applied. Within the [25,130] mg/dl range, the sensitivity was 0.021$\pm$0.003 nm/(mg/dl), while in the [152,200] mg/dl range, it was 0.184 nm/(mg/dl).

In conclusion, this chapter has unveiled the capabilities of the proposed sensor, offering a sensitive detection of glucose concentrations. However, it is crucial to perform selectivity studies to ensure an accurate measurement of the glucose. Overall, the sensor provided promising results that justify further investigation to ensure its applicability.

Chapter 6

Final Remarks and Future Work

Initially, the focus of this dissertation was the study and development of optical fibre sensors for refractometric sensing. Subsequently, the research efforts were redirected towards optimizing these sensing structures to establish a proof of concept for detecting and monitoring of glucose concentrations in aqueous solutions. This shift in focus was driven by the potential real-life applications of such sensors within the biomedical field.

The dissertation can be divided into two main sections. The first section involves the characterization of refractive index (RI) of various sensing tips, including single mode fibre (SMF), multimode fibre (MMF), coreless silica fibre (CSF), and CSF combined with graded-index fibre (GIF). The study and characterization of such tips was detailed in Chapter 3, and led to the conclusion that the CSF tip showed the most favorable response for RI measurements. Therefore, it was selected for further study and optimization in regards of the second section.

The second section covers Chapters 4 and 5. The research was concentrated on optimizing the CSF tip and developing an Au-functionalized plasmonic sensor based on an unclad multimode fibre. The main goal for both of these sensing configurations was to explore their potential for non-invasively detecting glucose concentrations in aqueous solutions, specifically, concentrations ranging from 25 to 200 mg/dl, mimicking the typical glucose levels found in human saliva.

Regarding the CSF tip, in Chapter 4, the optimization process was based in self-imaging principles to determine the optimal probe length. Additionally, GO was deposited onto the probe using a layer-by-layer technique to enhance its performance. The final sensitivity was determined to be $(1.0403 \pm 0.0004) \times 10^{-2}$ nm/(mg/dl) for glucose measurements

and 200±6 nm/RIU for RI characterization within the range of 1.3380 to 1.3853 RIU.
Further investigation is recommended, with potential future work outlined as follows:

- **Exploring Different GO Concentrations:** Considering that the GO concentration used in this study was 80 μg/ml for one bilayer of PEI/GO, different concentrations and layers can be applied. This exploration can potentially optimize the GO layer to enhance the performance of the sensing head.

- **GOx immobilization:** To help increase the sensitivity and selectivity of the probe.

The Chapter 5 provided a discussion of the plasmonic theory and the functionalization process. For the plasmonic sensor, the sensing head was submitted to an optimization through a functionalization process involving the covalent binding of glucose oxidase (GOx) to the gold (Au) surface.
The response curve of the sensor is characterized by an exponential fit. To facilitate analysis, this curve was segmented into two linear ranges. The calculated sensitivities for these ranges were 0.021±0.003 nm/(mg/dl) for the concentration range of [25,130] mg/dl, and 0.184±0.005 nm/(mg/dl) for the range of [152,200] mg/dl. Prior to the functionalization process, the probe was characterized in terms of refractive index (RI).
Future work is proposed, including:

- **Reflection Interrogation System:** Investigate the implementation of a reflection interrogation system instead of the current transmission scheme. This change could potentially enhance the performance of the sensor and make it more flexible to various scenarios, as only the tip would need to be immersed.

- **Selectivity Study:** Given that saliva is constituted by various compounds, a comprehensive study on the selectivity of the probe is crucial to eliminate cross-sensitivities.

When comparing both sensors, the plasmonic-based sensor achieved higher sensitivities than the GO based CSF tip. In contrast, the later offers a more cost-effective, robust, and simpler fabrication solution. In conclusion, both sensors demonstrated the capability to detect the proposed range, and, therefore supporting their potential for further development for real-time and label-free glucose monitoring and detection.

Appendix A

Raman Spectroscopy for Glucose Measurements

Raman spectroscopy is a non-destructive, low-cost characterization technique, typically used to provide a structural fingerprint by which molecules and different materials can be identified. It is based on the phenomenon of inelastic scattering of light and it was first observed, experimentally, by Raman and Krishnan in 1928 [103]. A source of monochromatic light, usually a laser, is employed in the system. The laser light interacts with molecular vibrations, resulting in shifts in the energy of the laser photons. The shifts in energy gives information about the vibrational modes in the system, which are specific to the chemical bonds and symmetry of a molecule - a fingerprint. In this case, the Raman spectroscopy was used to identify different glucose concentrations through the detection of Raman fingerprints of glucose, namely: {516,1062,1125,1366,1460} cm^{-1} [104]. The glucose aqueous solutions were prepared with glucose monohydrate from Sigma-Aldrich, ranging from 5 wt.% to 50 wt.%. The RI of the final solutions was determined with an Abbe refractometer (ATAGO, DR-A1) and ranged between 1.3379 RIU to 1.3834 RIU. The experimental setup is presented in Figure A.1 and it consists on the Raman Spectroscopy Kit for samples in cuvettes from Thorlabs. The complete kit includes a RSB1(/M) spectrometer base unit, a front end for collecting the scattered Raman signal (RSBC1/M cuvette) and an excitation laser input (FC/PC). The signal is processed in real-time on a computer with the Thorlabs OSA Raman Software. The kit is designed for 680 nm (visible range) to 785 nm (near infrared region - NIR) excitation and for a detection range of 815 nm to 915 nm, with a spectral resolution better than 10cm^{-1}.

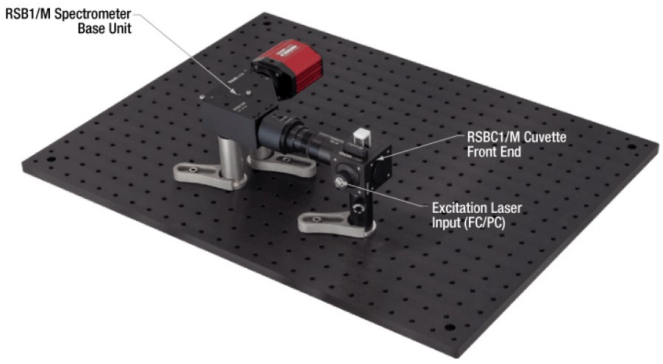

FIGURE A.1: Raman Spectroscopy Kit from Thorlabs.

Figure A.2a shows the resulting data analysis of the Raman spectrum. The baseline was removed and it was applied a 7-point adjacent averaging smoothing using software OriginLab. It is possible to observe different intensity bands, which correspond to the glucose fingerprints. The wavenumber of 1125cm^{-1} showed the best signal-to-noise ratio, followed by the wavenumber of 1062cm^{-1}. The spectral intensity response to the glucose concentration variations in aqueous solutions is presented in Figure A.2b. In both fingerprints is observed a linear relationship between the Raman intensity and the glucose concentration. As expected a higher concentration of glucose in the solution leads to a higher peak band, since there is more glucose molecules to interact with light, and therefore the magnitude of the inelastic scattering also increases. The results are consistent with reports such as [105, 106] and it can be conclude that Raman spectroscopy can be indeed used to detect glucose concentrations in aqueous solutions.

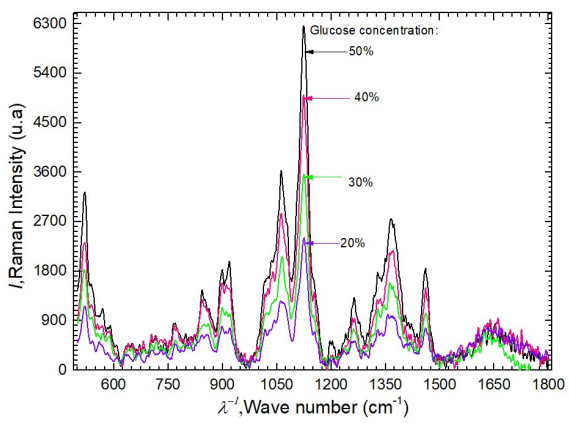

(A) Raman spectra measurements for different glucose solutions.

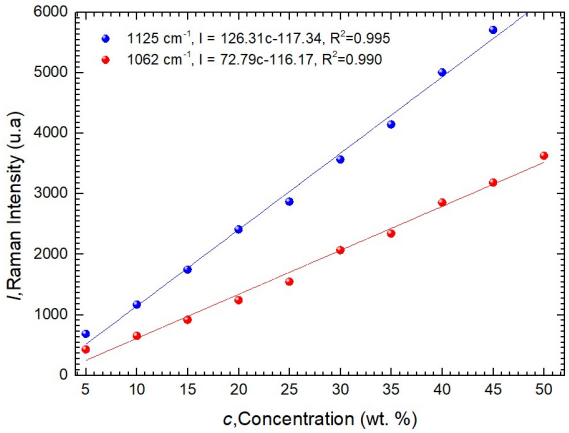

(B) Raman intensity response to glucose concentration variations.

FIGURE A.2: Raman spectroscopy experiment.

Appendix B

Refractive index conversion into glucose aqueous solutions concentration

A range of glucose aqueous solutions were prepared in a controlled laboratory environment, with glucose mass fractions varying from 0 wt.% to approximately 50 wt.%. The concentration of the solutions was measured using eleven liquid solutions of glucose monohydrate supplied by Sigma-Aldrich. A magnetic stirrer (NAHITA, magnetic stirred, model n° 690/1) was used to dilute the glucose in deionized water at room temperature. The concentration of the solutions ranged from 0.0001 g/ml to 0.5000 g/ml corresponding to a refractive index (RI) range of 1.3332 to 1.3806 RIU. The RI of each solution was determined by utilizing an Abbe refractometer (ATAGO, DR-A1). The glucose concentration present in the aqueous solutions was represented graphically as a function of the RI, as it is depicted in Figure B.1. It is possible to observe a linear relationship between the glucose aqueous solutions and the RI, respectively. For this range, the fitting curve has a correlation factor (R^2) of 0.999, and is described by the following equation:

$$c = 10.55n - 14.06 \tag{B.1}$$

Therefore, it is possible for this range to determine glucose concentrations in aqueous solutions through the RI.

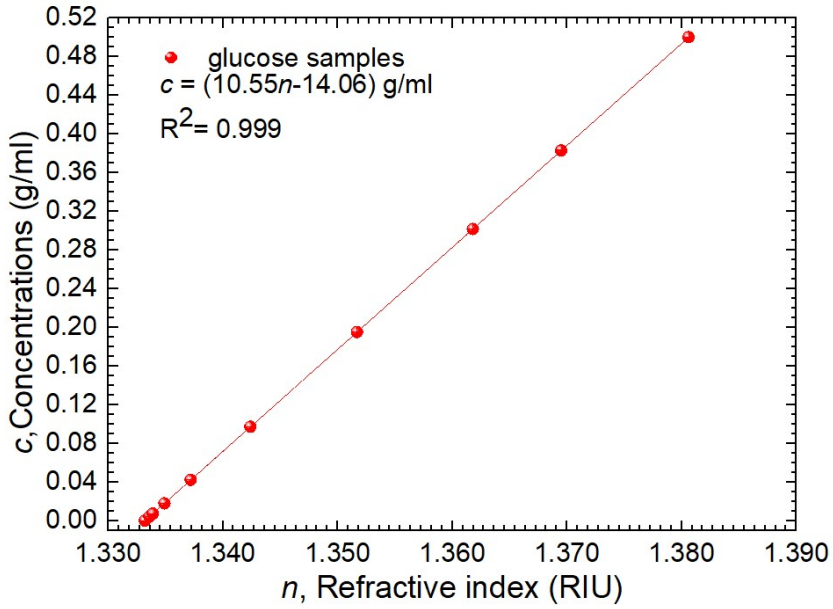

FIGURE B.1: Concentration of glucose in aqueous solutions as a function of RI.

Appendix C

Coreless Silica tip simulation using COMSOL Multiphysics

C.1 Work Flow of COMSOL Multiphysics Simulation Software

COMSOL Multiphysics serves as a comprehensive simulation platform offering both fully coupled multiphysics and single-physics modeling capabilities. The Model Builder encompasses the entire modeling workflow — from defining geometries and material properties to specifying physics that elucidate distinct phenomena, all the way to conducting computations and assessing results. In essence, the modeling workflow involves the subsequent steps:

1. Set up Model Environment.

2. Model geometry and dimensions - where it is possible to use solid or boundary modeling to create objects in 1D, 2D and 3D. It is also possible to import different CAD file formats.

3. Physics-based modeling and materials - by choosing the physics phenomena under study (fluid flow, electromagnetic fields, acoustics, among others) and by assigning relevant materials properties for each domain of the geometry.

4. Equation-based modeling - is possible to create model definitions based on mathematical equations and directly input them into the graphical user interface (GUI) of the software, including physics boundary conditions;

5. Mesh - it determines how the geometry is divided and with what shape or element type. The size, density, and number of elements in the geometry, including the element quality. These factors have a direct impact on the computation of a problem.

6. Studies and optimization.

7. Visualization and results evaluation - COMSOL allows you to generate reports containing images, plots, equations, and explanations of your simulation process.
In the subsequent section, these steps are implemented and concretized through the simulation of a coreless silica fiber (CSF) tip, spliced into a single mode fiber (SMF) functioning as the input/output light conduit.

C.2 Coreless Silica Tip Simulation

This model utilizes the *Electromagnetic Waves, Beam Envelopes* interface, employing am unidirectional formulation to simulate the propagation of light from a SMF (SM28, Thorlabs, USA) to a CSF (LA125, Thorlabs, USA) tip. The primary goal is to observe the self-imaging phenomena and the resulting interference pattern. The unidirectional formulation is applied due to the integration of single layer anti-reflective coatings in all surfaces to suppress reflections. Additionally, the geometry is surrounded by *Perfect Matched Layers* to absorb ongoing waves, and an analyte surrounding is also added to mimic the actual environment of the probe. Within the SMF, the phase is defined as *ewbe.beta_1*x*, resolved through the *Boundary Mode Analysis* study step. On the other hand, in the CSF tip, the light propagates similarly as in a free-space, while taking into consideration the refractive index of the coreless fibre. Finally, two ports are added in the beginning of the SMF, input light, and in the ending of the CSF, where the excitation is concluded. For a comprehensive understanding of the modeling instructions, the conclusive specifics are presented in the following section.

C.2.1 Modeling Instructions

From the **File** menu, choose **New.**

NEW:

1. In the **New**, window click **Model Wizard.**

MODEL WIZARD:

1. In the **Model Wizard** window, click **2D**.

2. In the **Select Physics** tree, select **Optics**>**Wave Optics**>**Electromagnetic Waves, Beam Envelopes (ewbe)**.

3. Click **Add**.

4. Click **Study**.

5. In the **Select Study** tree, select **Preset Studies for Selected Physics Interfaces**>**Frequency Domain**

6. Click **Done**.

GLOBAL DEFINITIONS

Parameters I

1. In the **Model Builder** window, under **Global Definitions** click **Parameters I**. In Figure C.1 is presented the parameters as they were defined in the software.

Name	Expression	Value	Description
n_air	1	1	air RI
n_cladding	1.444	1.444	cladding RI SMF
n_ncf	1.4440	1.444	coreless fibre RI
n_core	1.4529	1.4529	core RI SMF
w	1.55 [um]	1.55E-6 m	interference wavelength
t_pml	10 [um]	1E-5 m	perfect match layer
d_cladding	125 [um]	1.25E-4 m	cladding diameter SMF
t_air	30 [um]	3E-5 m	thickness of air layer
l_ncf	34 [mm]	0.034 m	coreless fibre length
l_fibre	5 [mm]	0.005 m	fibre length
l_air	5 [mm]	0.005 m	length of air portion
d_core	8.2 [um]	8.2E-6 m	core diameter SMF

FIGURE C.1: Parameters defined in the Multiphysics COMSOL 6.0 software.

Geometry I

1. In the Model Builder window, under Component 1 (comp1) click Geometry 1.

2. In the Settings window for Geometry, locate the Units section.

3. From the Length unit list, choose mm.

4. Geometry toolbar was used to design the CSF tip.

5. Click **Build All Objects**

In Figure C.2 is presented the final geometry for the probe.

MATERIALS

1. In the **Model Builder**, under **Component I (compI)** right-click **Materials** and choose **Blanck Material**.

2. In the **Settings** window for **Material**, type *Material core* in the **Label** text field.

3. Select Domain 4 (Core Domain).

4. Locate the **Material Contents** section. In the table, enter the following setting in the **Value** column, next to the **Property**>Refractive index, real part: *n_core* (was defined in the parameters table).

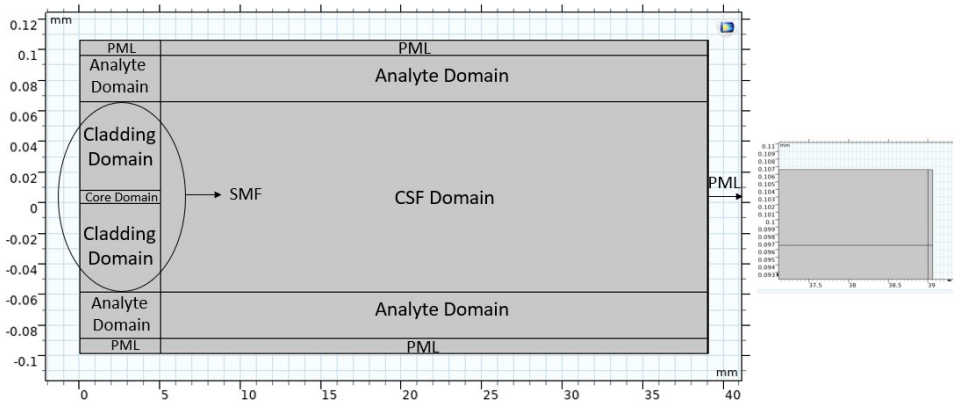

FIGURE C.2: 2D SMF-CSF tip design for simulation purposes.

5. Repeat the same procedure of the remaining domains of the design. For the analyte and PML domains it was chosen **Air**, with a refractive index, real part of 1. The imaginary parts were assumed to be 0.

ELETROMAGNETIC WAVES, BEAM ENVELOPES (EWBE)

1. In the **Model Builder**, under **Component I (compI)** click **Eletromagnetic Waves Beam Envelopes (ewbe)**.

2. In the **Settings** window for **Electromagnetic Waves, Beam Envelopes**, locate the **Components** section.

3. From the **Electric field components solved for** list, choose **Out-of-plane vector**.

4. Locate the **Wave Vectors** section. From the **Number of directions** list, choose **Unidirectional**.

5. From the **Type of phase specification** list, choose **User defined**.

6. In the ψ_1 text field, type *psi*. This variable will be defined after all physics features have been added.

Ports

1. In the **Physics** toolbar, click **Boundaries** and choose **Port**. Two ports should be added, one for the input light and other for the output light.

2. Select Boundaries 5,7 and 9 for the first port and 33 for the second port.

3. In the **Settings** window for **Port**, locate the **Port Properties** section.

4. From the **Type of port** list, choose **Numeric**.

5. In the first/second port, under **Port name** type *1/2* and in the box of **Wave excitation at this port** select **On/Off**.

6. In the second port select **Activate slid condition on interior port** check box and from

the **Slit type** list, choose **Domain-backed**.

Transition Boundary Condition I

A **Transition boundary condition** should be feature, to model anti-reflection (AR) coatings in the boundary between the SMF and CSF.

1. In the **Physics** toolbar, click **Boundaries** and choose **Transition Boundary Condition**.

2. Select Boundaries 16, 18, 20, 22, 23, 24 and 26.

3. In the **Settings** window for **Transition Boundary Condition**, locate the **Transition Boundart Condition** section.

4. From the *n* list, choose **User defined**. In the associated text field, type *sqrt(ewbe.neff_1)*, to define the refractive index for the AR coating layer.

5. From the *k* list, choose **User defined**. In the *d* text field, type *1e-9*, to define the thickness of the AR coating layer.

DEFINITIONS

Now, lets add the expressions for the user-defined phase, that is used by the EWBE interface.

Variables

1. In the **Model Builder** window, under **Component I (compI)** right-click **Definitions** and choose **Variables**.

2. In the **Settings** window for **Variables**, locate the **Geometric Entity Selection** section.

3. From the **Geometric entity level** list, choose **Domain**.

4. Select Domains 1-7 (left side on the SMF domain).

5. Locate the **Variables** section. In the table, enter the following settings: **Name**>*psi*; **Expression**>*ewbe.beta_1*x*; **Unit**>*rad*.

Repeat the steps 1 to 3:

6. Select Domains 8-17 (right side on the CSF domain).

7. Locate the **Variables** section. In the table, enter the following settings: **Name**>*psi*; **Expression**>*ewbe.k*x*; **Unit**>*rad*.

Perfect Matched Layer I

1. In the **Definitions** toolbar, click **Perfect Matched Layer**.

2. Select Domains 1,7,8, 12-17. This corresponds to the thin top, bottom, and right-most domains.

MESH 1

Define a mesh that resolves the variations of the field envelope.

1. In the **Model Builder** window, under **Component 1 (comp1)** right-click **Mesh 1** and choose **Build All**.

2. In the **Settings** window for **Mesh**, locate the **Sequence Type** section.

3. From the list, choose **Physics-controlled mesh**.

4. In the **Settings** window for **Mesh**, locate the **Element Size**. From the list, choose **Extremely Fine**.

5. In the **Settings** window for **Mesh**, locate the **Mesh Type**. From the list, choose **Triangular mesh**.

6. In the **Settings** window for **Mesh**, locate the **Maximum element size in free space**. In the text field type ***w*2.5**.

STUDY 1

Step 1: Boundary Mode Analysis.

1. In the **Model Builder** window, under **Study 1** click **Step 1: Boundary Mode Analysis**.

2. In the **Settings** window for **Boundary Mode Analysis**, locate the **Study Settings** section.

3. In the **Mode analysis frequency** text field, type *c_const/w*.

5. Select the **Search for modes around** check box. In the associated text field, type *n_core*.

Step 2: Boundary Mode Analysis 1.

1. Right-click **Study 1**>**Step 1: Boundary Mode Analysis** and choose **Duplicate**.

2. In the **Settings** window for **Boundary Mode Analysis**, locate the **Study Settings** section.

3. In the **Port name** text field, type *2*.

Step 3: Frequency Domain.

1. In the **Model Builder** window, click **Step 3: Frequency Domain.**

2. In the **Settings** window for **Frequency Domain**, locate the **Study Settings** section.

3. In the **Frequencies** text field, type *c_const/w*

After all the steps are completed, in the **Study** toolbar, click **Compute**

RESULTS

In the **Results** section, under **Electric Field** is possible to observe the final results of the simulation. It is also possible to perform **1D Plot Groups** through **Cut Line 2D** to study the electric fields throughout the SMF-CSF tip simulation.

Bibliography

[1] K. K. K. Annamdas and V. G. M. Annamdas, "Review on developments in fiber optical sensors and applications," in *Fiber Optic Sensors and Applications VII*, A. Mendez, H. H. Du, A. Wang, E. Udd, and S. J. Mihailov, Eds., vol. 7677, International Society for Optics and Photonics. SPIE, 2010, p. 76770R. [Online]. Available: https://doi.org/10.1117/12.849799 [Cited on pages 1 and 9.]

[2] Y. Chen, J. Liu, Z. Yang, J. S. Wilkinson, and X. Zhou, "Optical biosensors based on refractometric sensing schemes: A review," *Biosensors and Bioelectronics*, vol. 144, p. 111693, 2019. [Online]. Available: https://doi.org/10.1016/j.bios.2019.111693 [Cited on page 1.]

[3] C. Caucheteur, T. Guo, and J. Albert, "Review of plasmonic fiber optic biochemical sensors: improving the limit of detection," *Analytical and bioanalytical chemistry*, vol. 407, pp. 3883–3897, 2015. [Online]. Available: https://doi.org/10.1007/s00216-014-8411-6 [Cited on page 1.]

[4] C. Gouveia, A. Markovics, J. Baptista, B. Kovacs, and P. Jorge, "Measurement of co2 using refractometric fiber optic sensors," in *Proceedings of the 3rd WSEAS International Conference on Advances in Sensors, Signals and Materials, Stevens Point, WI, USA*, 2010, pp. 169–173. [Online]. Available: https://www.researchgate.net/publication/225082904 [Cited on page 1.]

[5] P. Gong, X. Li, X. Zhou, Y. Zhang, N. Chen, S. Wang, S. Zhang, and Y. Zhao, "Optical fiber sensors for glucose concentration measurement: A review," *Optics & Laser Technology*, vol. 139, p. 106981, 2021. [Online]. Available: https://api.semanticscholar.org/CorpusID:233552707 [Cited on pages 2, 5, and 8.]

[6] W. Zheng, B. Han, S. E, Y. Sun, X. Li, Y. Cai, and Y. nan Zhang, "Highly-sensitive and reflective glucose sensor based on optical fiber surface plasmon resonance,"

Microchemical Journal, vol. 157, p. 105010, 2020. [Online]. Available: https://www.sciencedirect.com/science/article/pii/S0026265X19337154 [Cited on pages 12, 13, 54, and 56.]

[7] S. Novais, C. I. Ferreira, M. S. Ferreira, and J. L. Pinto, "Optical fiber tip sensor for the measurement of glucose aqueous solutions," *IEEE Photonics Journal*, vol. 10, no. 5, pp. 1–9, 2018. [Online]. Available: https://ieeexplore.ieee.org/document/8463572 [Cited on pages 2, 14, 15, and 29.]

[8] N. S. Kapany, "Fiber optics," *Scientific American*, vol. 203, no. 5, pp. 72–81, 1960. [Online]. Available: http://www.jstor.org/stable/24940695 [Cited on page 5.]

[9] B. Saleh and M. Teich, *Fundamentals of Photonics, 3rd Edition*, 02 2019. [Cited on pages ix, 6, and 7.]

[10] G. Keiser, *Optical fiber communications*. McGraw-Hill New York, 2000, vol. 2. [Cited on pages ix, 6, and 7.]

[11] D. Gloge, "Weakly guiding fibers," *Appl. Opt.*, vol. 10, no. 10, pp. 2252–2258, Oct 1971. [Online]. Available: https://opg.optica.org/ao/abstract.cfm?URI=ao-10-10-2252 [Cited on page 6.]

[12] P. Lu, N. Lalam, M. Badar, B. Liu, B. T. Chorpening, M. P. Buric, and P. R. Ohodnicki, "Distributed optical fiber sensing: Review and perspective," *Applied Physics Reviews*, vol. 6, no. 4, p. 041302, 2019. [Online]. Available: https://doi.org/10.1063/1.5113955 [Cited on page 8.]

[13] R. Min, Z. Liu, L. Pereira, C. Yang, Q. Sui, and C. Marques, "Optical fiber sensing for marine environment and marine structural health monitoring: A review," *Optics & Laser Technology*, vol. 140, p. 107082, 2021. [Online]. Available: https://doi.org/10.1016/j.optlastec.2021.107082

[14] A. G. Leal-Junior, C. A. Diaz, L. M. Avellar, M. J. Pontes, C. Marques, and A. Frizera, "Polymer optical fiber sensors in healthcare applications: A comprehensive review," *Sensors*, vol. 19, no. 14, p. 3156, 2019. [Online]. Available: https://doi.org/10.3390/s19143156

[15] A. Cutolo, R. Bernini, G. M. Berruti, G. Breglio, F. A. Bruno, S. Buontempo, E. Catalano, M. Consales, A. Coscetta, A. Cusano *et al.*, "Innovative photonic

sensors for safety and security, part ii: Aerospace and submarine applications," *Sensors*, vol. 23, no. 5, p. 2417, 2023. [Online]. Available: https://doi.org/10.3390/s23052417 [Cited on page 8.]

[16] D. A. Krohn, T. MacDougall, and A. Mendez, *Fiber optic sensors: fundamentals and applications*. Spie Press Bellingham, WA, 2014. [Cited on pages 8 and 9.]

[17] J. L. Santos and F. Farahi, *Handbook of optical sensors*. Crc Press, 2014. [Cited on pages 8, 9, and 10.]

[18] M. M. Eid, "Optical fiber sensors: review of technology and applications," *Indonesian Journal of Electrical Engineering and Computer Science*, vol. 25, no. 2, pp. 1038–1046, 2022. [Online]. Available: https://www.researchgate.net/publication/358269445 [Cited on pages ix, 8, and 9.]

[19] Y. Zheng, J. Yu, Z.-W. Zhu, B. Zeng, and C. Yang, "Design, sensing principle and testing of a novel fiber optic displacement sensor based on linear macro-bending loss," *Optik*, vol. 242, p. 167194, 2021. [Online]. Available: https://www.sciencedirect.com/science/article/pii/S0030402621008585 [Cited on page 9.]

[20] X. Yang, Z. Chen, C. S. M. Elvin, L. H. Y. Janice, S. H. Ng, J. T. Teo, and R. Wu, "Textile fiber optic microbend sensor used for heartbeat and respiration monitoring," *IEEE Sensors Journal*, vol. 15, no. 2, pp. 757–761, 2015. [Online]. Available: https://ieeexplore.ieee.org/document/6888477 [Cited on page 9.]

[21] B. H. Lee, Y. H. Kim, K. S. Park, J. B. Eom, M. J. Kim, B. S. Rho, and H. Y. Choi, "Interferometric fiber optic sensors," *Sensors*, vol. 12, no. 3, pp. 2467–2486, 2012. [Online]. Available: https://www.mdpi.com/1424-8220/12/3/2467 [Cited on page 9.]

[22] J. K. Sahota, N. Gupta, and D. Dhawan, "Fiber bragg grating sensors for monitoring of physical parameters: A comprehensive review," *Optical Engineering*, vol. 59, no. 6, pp. 060 901–060 901, 2020. [Online]. Available: https://doi.org/10.3390/s121012890 [Cited on page 9.]

[23] B. Xu, J. Huang, L. Ding, and J. Cai, "Graphene oxide-functionalized long period fiber grating for ultrafast label-free glucose biosensor," *Materials Science*

and Engineering: C, vol. 107, p. 110329, 2020. [Online]. Available: https://www.sciencedirect.com/science/article/pii/S0928493118336993 [Cited on page 9.]

[24] M. S. Peixoto e Silva, T. H. C. d. Barros, H. P. Alves, J. F. d. Nascimento, and J. F. Martins Filho, "Evaluation of fiber optic raman scattering distributed temperature sensor between –196 and 400 °c," *IEEE Sensors Journal*, vol. 21, no. 2, pp. 1527–1533, 2021. [Online]. Available: https://ieeexplore.ieee.org/document/9166556 [Cited on page 9.]

[25] K. Wang, X. Dong, M. H. Köhler, P. Kienle, Q. Bian, M. Jakobi, and A. W. Koch, "Advances in optical fiber sensors based on multimode interference (mmi): A review," *IEEE Sensors Journal*, vol. 21, no. 1, pp. 132–142, 2021. [Online]. Available: https://ieeexplore.ieee.org/document/9162065 [Cited on pages ix, 9, 10, and 11.]

[26] A. Mehta, W. Mohammed, and E. Johnson, "Multimode interference-based fiber-optic displacement sensor," *IEEE Photonics Technology Letters*, vol. 15, no. 8, pp. 1129–1131, 2003. [Online]. Available: https://ieeexplore.ieee.org/document/1215526 [Cited on page 10.]

[27] K. Tian, G. Farrell, X. Wang, Y. Xin, Y. Du, W. Yang, H. Liang, E. Lewis, and P. Wang, "High sensitivity temperature sensor based on singlemode-no-core-singlemode fibre structure and alcohol," *Sensors and Actuators A: Physical*, vol. 284, pp. 28–34, 2018. [Online]. Available: https://doi.org/10.1016/j.sna.2018.10.016 [Cited on page 10.]

[28] Q. Wu, Y. Semenova, A. M. Hatta, P. Wang, and G. Farrell, "Bent sms fibre structure for temperature measurement," *Electronics letters*, vol. 46, no. 16, pp. 1129–1130, 2010. [Online]. Available: https://www.researchgate.net/publication/224164945 [Cited on page 10.]

[29] Y. Zhao, L. Cai, and H.-F. Hu, "Fiber-optic refractive index sensor based on multi-tapered sms fiber structure," *IEEE Sensors Journal*, vol. 15, no. 11, pp. 6348–6353, 2015. [Online]. Available: https://ieeexplore.ieee.org/document/7163533 [Cited on page 10.]

[30] F. Villuendas and J. Pelayo, "Optical fibre device for chemical seming based on surface plasmon excitridon," *Sensors and Actuators A: Physical*, vol. 23, no. 1, pp. 1142–1145, 1990, proceedings of the 5th International Conference on

Solid-State Sensors and Actuators and Eurosensors III. [Online]. Available: https://www.sciencedirect.com/science/article/pii/092442479087104Q [Cited on page 10.]

[31] R. B. Schasfoort, *Handbook of surface plasmon resonance*. Royal Society of Chemistry, 2017. [Cited on pages 11 and 12.]

[32] O. R. Bolduc and J.-F. Masson, "Advances in surface plasmon resonance sensing with nanoparticles and thin films: nanomaterials, surface chemistry, and hybrid plasmonic techniques," 2011. [Online]. Available: https://pubs.acs.org/doi/10.1021/ac2012976 [Cited on page 12.]

[33] A. K. Sharma, R. Jha, and B. D. Gupta, "Fiber-optic sensors based on surface plasmon resonance: A comprehensive review," *IEEE Sensors Journal*, vol. 7, no. 8, pp. 1118–1129, 2007. [Online]. Available: https://ieeexplore.ieee.org/document/4260987 [Cited on pages ix, 12, and 51.]

[34] A. Shafkat, A. N. Z. Rashed, H. M. El-Hageen, and A. M. Alatwi, "The effects of adding different adhesive layers with a microstructure fiber sensor based on surface plasmon resonance: a numerical study," *Plasmonics*, vol. 16, pp. 819–832, 2021. [Online]. Available: https://link.springer.com/article/10.1007/s11468-020-01352-y [Cited on pages ix, 12, and 13.]

[35] J. Boehm, A. François, H. Ebendorff-Heidepriem, and T. M. Monro, "Chemical deposition of silver for the fabrication of surface plasmon microstructured optical fibre sensors," *Plasmonics*, vol. 6, pp. 133–136, 2011. [Online]. Available: https://link.springer.com/article/10.1007/s11468-010-9178-z [Cited on page 12.]

[36] N. F. Murat, W. M. Mukhtar, A. R. A. Rashid, K. A. Dasuki, and A. A. R. A. Yussuf, "Optimization of gold thin films thicknesses in enhancing spr response," in *2016 IEEE International Conference on Semiconductor Electronics (ICSE)*, 2016, pp. 244–247. [Online]. Available: https://ieeexplore.ieee.org/document/7573637 [Cited on page 13.]

[37] J. E. Proctor, D. M. Armada, and A. Vijayaraghavan, *An introduction to graphene and carbon nanotubes*. CRC Press, 2017. [Cited on page 13.]

[38] K. S. Novoselov, A. K. Geim, S. V. Morozov, D. Jiang, Y. Zhang, S. V. Dubonos, I. V. Grigorieva, and A. A. Firsov, "Electric field effect in atomically thin carbon films," *Science*, vol. 306, no. 5696, pp. 666–669, 2004. [Online]. Available: https://www.science.org/doi/abs/10.1126/science.1102896 [Cited on page 13.]

[39] A. C. Ferrari, F. Bonaccorso, V. Fal'Ko, K. S. Novoselov, S. Roche, P. Bøggild, S. Borini, F. H. Koppens, V. Palermo, N. Pugno *et al.*, "Science and technology roadmap for graphene, related two-dimensional crystals, and hybrid systems," *Nanoscale*, vol. 7, no. 11, pp. 4598–4810, 2015. [Online]. Available: https://doi.org/10.1039/C4NR01600A [Cited on page 13.]

[40] B. N. Shivananju, W. Yu, Y. Liu, Y. Zhang, B. Lin, S. Li, and Q. Bao, "The roadmap of graphene-based optical biochemical sensors," *Advanced Functional Materials*, vol. 27, no. 19, p. 1603918, 2017. [Online]. Available: https://doi.org/10.1002/adfm.201603918 [Cited on page 13.]

[41] J. xin Li, Z. rong Tong, L. Jing, W. hua Zhang, J. Qin, and J. wei Liu, "Fiber temperature and humidity sensor based on photonic crystal fiber coated with graphene oxide," *Optics Communications*, vol. 467, p. 125707, 2020. [Online]. Available: https://www.sciencedirect.com/science/article/pii/S0030401820302509 [Cited on page 13.]

[42] J. x. Li, W. h. Zhang, Z. r. Tong, and J. w. Liu, "Fiber optic sensor modified by graphene oxide–glucose oxidase for glucose detection," *Optics Communications*, vol. 492, p. 126983, 2021. [Online]. Available: https://doi.org/10.1016/j.optcom.2021.126983 [Cited on page 13.]

[43] P. Kumar, S. Kumar, J. Kumar, G. Purbia, O. Prakash, and S. Dixit, "Graphene-oxide-coated fiber bragg grating sensor for ethanol detection in petrol," *Measurement Science and Technology*, vol. 31, no. 2, p. 025109, 2019. [Online]. Available: https://iopscience.iop.org/article/10.1088/1361-6501/ab2d63 [Cited on page 13.]

[44] G. Xiao, K. Zhang, Y. Yang, H. Yang, L. Guo, J. Li, and L. Yuan, "Graphene oxide sensitized no-core fiber step-index distribution sucrose sensor," in *Photonics*, vol. 7, no. 4. MDPI, 2020, p. 101. [Online]. Available: https://doi.org/10.3390/photonics7040101 [Cited on page 13.]

[45] P. R.Cooper, "Refractive-index measurements of paraffin, a silicone elastomer, and an epoxy resin over the 500–1500 nm spectral range," *Appl. Opt.*, vol. 21, no. 19, pp. 3413–3415, Oct 1982. [Online]. Available: https://opg.optica.org/ao/abstract.cfm?URI=ao-21-19-3413 [Cited on page 14.]

[46] P. R. Cooper, "Refractive-index measurements of liquids used in conjunction with optical fibers," *Appl. Opt.*, vol. 22, no. 19, pp. 3070–3072, Oct 1983. [Online]. Available: https://opg.optica.org/ao/abstract.cfm?URI=ao-22-19-3070 [Cited on page 14.]

[47] A. Kumar, T. Subrahmanyam, A. Sharma, K. Thyagarajan, B. Pal, and I. Goyal, "Novel refractometer using a tapered optical fibre," *Electronics Letters*, vol. 20, no. 13, pp. 534 – 535, 1984. [Online]. Available: https://www.researchgate.net/publication/3399809 [Cited on page 14.]

[48] A. Yasli, "Cancer detection with surface plasmon resonance-based photonic crystal fiber biosensor," *Plasmonics*, vol. 16, no. 5, pp. 1605–1612, 2021. [Online]. Available: https://www.researchgate.net/publication/350191674 [Cited on page 14.]

[49] N. Zhang, W. Xu, S. You, C. Yu, C. Yu, B. Dong, and K. Li, "Simultaneous measurement of refractive index, strain and temperature using a tapered structure based on smf," *Optics Communications*, vol. 410, pp. 70–74, 2018. [Online]. Available: https://www.sciencedirect.com/science/article/pii/S0030401817308751 [Cited on page 14.]

[50] S. Novais, M. S. Ferreira, and J. L. Pinto, "Determination of thermo-optic coefficient of ethanol-water mixtures with optical fiber tip sensor," *Optical Fiber Technology*, vol. 45, pp. 276–279, 2018. [Online]. Available: https://www.sciencedirect.com/science/article/pii/S106852001830378X [Cited on page 15.]

[51] Q. Wang and B.-T. Wang, "Surface plasmon resonance biosensor based on graphene oxide/silver coated polymer cladding silica fiber," *Sensors and Actuators B: Chemical*, vol. 275, pp. 332–338, 2018. [Online]. Available: https://www.sciencedirect.com/science/article/pii/S092540051831503X [Cited on page 15.]

[52] Y. Zheng, T. Lang, B. Cao, J. Jin, R. Dong, and H. Feng, "Fiber optic spr sensor for human immunoglobulin g measurement based on the mmf-ncf-mmf structure," *Optical Fiber Technology*, vol. 46, pp. 179–185, 2018. [Online]. Available:

https://www.sciencedirect.com/science/article/pii/S1068520018304875 [Cited on page 15.]

[53] M. Zhang, G. Zhu, L. Lu, X. Lou, and L. Zhu, "Refractive index sensor based on ultrafine tapered single-mode nocladding single-mode fiber structure," *Optical Fiber Technology*, vol. 48, pp. 297–302, 2019. [Online]. Available: https://www.sciencedirect.com/science/article/pii/S1068520018306631 [Cited on page 15.]

[54] L. Wang, L. Yang, C. Zhang, C. Miao, J. Zhao, and W. Xu, "High sensitivity and low loss open-cavity mach-zehnder interferometer based on multimode interference coupling for refractive index measurement," *Optics Laser Technology*, vol. 109, pp. 193–198, 2019. [Online]. Available: https://www.sciencedirect.com/science/article/pii/S0030399218306546 [Cited on page 15.]

[55] P. Wang, S. Zhang, R. Wang, G. Farrell, M. Zhang, T. Geng, E. Lewis, and K. Tian, "Temperature-insensitive refractometer based on an ri-modulated singlemode-multimode-singlemode fibre structure," *Opt. Express*, vol. 27, no. 10, pp. 13 754–13 764, May 2019. [Online]. Available: https://opg.optica.org/oe/abstract.cfm?URI=oe-27-10-13754 [Cited on page 15.]

[56] F. Han, T. Lang, B. Mao, C. Zhao, J. Kang, C. Shen, and D. Wang, "Surface plasmon resonance sensor based on coreless fiber for high sensitivity," *Optical Fiber Technology*, vol. 50, pp. 172–176, 2019. [Online]. Available: https://www.sciencedirect.com/science/article/pii/S1068520018307326 [Cited on page 15.]

[57] H. Hu, X. Song, Q. Han, P. Chang, J. Zhang, K. Liu, Y. Du, H. Wang, and T. Liu, "High sensitivity fiber optic spr refractive index sensor based on multimode-no-core-multimode structure," *IEEE Sensors Journal*, vol. 20, no. 6, pp. 2967–2975, 2020. [Online]. Available: https://ieeexplore.ieee.org/document/8918508 [Cited on page 15.]

[58] F. Wang, K. Pang, T. Ma, X. Wang, and Y. Liu, "Folded-tapered multimode-no-core fiber sensor for simultaneous measurement of refractive index and temperature," *Optics Laser Technology*, vol. 130, p. 106333, 2020. [Online]. Available: https://www.sciencedirect.com/science/article/pii/S003039922030966X [Cited on page 16.]

[59] G. Xiao, K. Zhang, Y. Yang, H. Yang, L. Guo, J. Li, and L. Yuan, "Graphene oxide sensitized no-core fiber step-index distribution sucrose sensor," *Photonics*, vol. 7,

no. 4, 2020. [Online]. Available: https://www.mdpi.com/2304-6732/7/4/101 [Cited on page 16.]

[60] S. Zhang, Z. Wang, M. Zhu, L. Li, S. Wang, S. Li, F. Peng, H. Niu, X. Li, S. Deng, T. Geng, W. Yang, and L. Yuan, "A compact refractive index sensor with high sensitivity based on multimode interference," *Sensors and Actuators A: Physical*, vol. 315, p. 112360, 2020. [Online]. Available: https://www.sciencedirect.com/science/article/pii/S0924424720316769 [Cited on page 16.]

[61] Y. Zhang, M. Liu, Y. Zhang, Z. Liu, X. Yang, J. Zhang, J. Yang, and L. Yuan, "Simultaneous measurement of temperature and refractive index based on a hybrid surface plasmon resonance multimode interference fiber sensor," *Appl. Opt.*, vol. 59, no. 4, pp. 1225–1229, Feb 2020. [Online]. Available: https://opg.optica.org/ao/abstract.cfm?URI=ao-59-4-1225 [Cited on page 16.]

[62] R. Nasirifar, M. Danaie, and A. Dideban, "Hollow-core graded index optical fiber refractive index sensor based on surface plasmon resonance," *Optical and Quantum Electronics*, vol. 52, pp. 1–23, 2020. [Cited on page 16.]

[63] F. Xia, H. Song, Y. Zhao, W.-M. Zhao, Q. Wang, X.-Z. Wang, B.-T. Wang, and Z.-X. Dai, "Ultra-high sensitivity spr fiber sensor based on multilayer nanoparticle and au film coupling enhancement," *Measurement*, vol. 164, p. 108083, 2020. [Online]. Available: https://www.sciencedirect.com/science/article/pii/S0263224120306217 [Cited on page 16.]

[64] J. H. Osório, W. M. Guimarães, L. Peng, M. A. Franco, S. C. Warren-Smith, H. Ebendorff-Heidepriem, and C. M. Cordeiro, "Exposed-core fiber multimode interference sensor," *Results in Optics*, vol. 5, p. 100125, 2021. [Online]. Available: https://www.sciencedirect.com/science/article/pii/S2666950121000730 [Cited on page 16.]

[65] Y. Zheng, X. Yang, W. Feng, and W. Fan, "Optical fiber refractive index sensor based on smf-tcf-ncf-smf interference structure," *Optik*, vol. 226, p. 165900, 2021. [Online]. Available: https://www.sciencedirect.com/science/article/pii/S0030402620317174 [Cited on page 16.]

[66] L. Liu, J. Zheng, S. Deng, L. Yuan, and C. Teng, "Parallel polished plastic optical fiber-based spr sensor for simultaneous measurement of ri and temperature," *IEEE*

Transactions on Instrumentation and Measurement, vol. 70, pp. 1–8, 2021. [Online]. Available: https://ieeexplore.ieee.org/document/9400473 [Cited on page 16.]

[67] Y. Liu, H. Chen, H. Li, S. Zhang, Z. Gao, Y. Feng, Y. Zhang, and S. Li, "High-performance surface plasmon resonance refractometer based on a no-core fiber coated with a silver film," *J. Opt. Soc. Am. B*, vol. 38, no. 9, pp. 2536–2542, Sep 2021. [Online]. Available: https://opg.optica.org/josab/abstract.cfm?URI=josab-38-9-2536 [Cited on page 16.]

[68] Y. Singh and S. K. Raghuwanshi, "Titanium dioxide (tio2) coated optical fiber-based spr sensor in near-infrared region with bimetallic structure for enhanced sensitivity," *Optik*, vol. 226, p. 165842, 2021. [Online]. Available: https://www.sciencedirect.com/science/article/pii/S0030402620316624 [Cited on page 17.]

[69] S. Yan, S. Pu, Y. Zhang, M. Yuan, and C. Zhang, "Sensing properties of graphene-oxide-functionalized single-mode–no-core–single-mode fiber structure," *Results in Physics*, vol. 25, p. 104310, 2021. [Online]. Available: https://www.sciencedirect.com/science/article/pii/S2211379721004411 [Cited on pages 17 and 45.]

[70] C. Teng, M. Li, R. Min, S. Deng, M. Chen, M. Xue, L. Yuan, and H. Deng, "A high-sensitivity spr sensor based on mmf-tapered hcf-mmf fiber structure for refractive index sensing," *IEEE Sensors Journal*, vol. 22, no. 19, pp. 18 517–18 523, 2022. [Online]. Available: https://ieeexplore.ieee.org/document/9869352 [Cited on page 17.]

[71] C. Teng, S. Ying, R. Min, S. Deng, H. Deng, M. Chen, X. Chu, L. Yuan, Y. Cheng, and M. Xue, "Side-polish plastic optical fiber based spr sensor for refractive index and liquid-level sensing," *Sensors*, vol. 22, no. 16, 2022. [Online]. Available: https://www.mdpi.com/1424-8220/22/16/6241 [Cited on page 17.]

[72] X. Fu, D. Li, Y. Zhang, G. Fu, W. Jin, and W. Bi, "High sensitivity refractive index sensor based on cascaded core-offset splicing ncf-hcf-ncf structure," *Optical Fiber Technology*, vol. 68, p. 102791, 2022. [Online]. Available: https://www.sciencedirect.com/science/article/pii/S1068520021003412 [Cited on page 17.]

[73] H.-T. Chou, Y.-S. Liao, T.-M. Wu, S.-H. Wang, K.-H. Chiang, and W.-C. Su, "Development of localized surface plasmon resonance-based optical fiber biosensor for immunoassay using gold nanoparticles and graphene oxide nanocomposite film," *IEEE Sensors Journal*, vol. 22, no. 7, pp. 6593–6600, 2022. [Online]. Available: https://ieeexplore.ieee.org/document/9698179 [Cited on page 17.]

[74] H. Dang, Y. Zhang, Y. Qiao, and J. Li, "Refractive index and temperature sensing performance of microfiber modified by uv glue distributed nanoparticles," *Polymers*, vol. 14, no. 12, 2022. [Online]. Available: https://www.mdpi.com/2073-4360/14/12/2425 [Cited on page 17.]

[75] J. S. Paiva, P. A. Jorge, C. C. Rosa, and J. P. Cunha, "Optical fiber tips for biological applications: from light confinement, biosensing to bioparticles manipulation," *Biochimica et Biophysica Acta (BBA)-General Subjects*, vol. 1862, no. 5, pp. 1209–1246, 2018. [Online]. Available: https://doi.org/10.1016/j.bbagen.2018.02.008 [Cited on page 19.]

[76] Y. Xiong and F. Xu, "Multifunctional integration on optical fiber tips: challenges and opportunities," *Advanced Photonics*, vol. 2, no. 6, pp. 064 001–064 001, 2020. [Online]. Available: https://www.researchgate.net/publication/345998274 [Cited on page 19.]

[77] R. Romero, O. Frazão, D. Pereira, H. Salgado, F. Araújo, and L. Ferreira, "Intensity-referenced and temperature-independent curvature-sensing concept based on chirped fiber bragg gratings," *Applied optics*, vol. 44, no. 18, pp. 3821–3826, 2005. [Online]. Available: https://doi.org/10.1364/AO.44.003821 [Cited on page 23.]

[78] S. Silva, O. Frazão, J. Santos, and F. Malcata, "A reflective optical fiber refractometer based on multimode interference," *Sensors and Actuators B: Chemical*, vol. 161, no. 1, pp. 88–92, 2012. [Online]. Available: https://doi.org/10.1016/j.snb.2011.09.045 [Cited on page 25.]

[79] Q. Wang and G. Farrell, "All-fiber multimode-interference-based refractometer sensor: proposal and design," *Optics letters*, vol. 31, no. 3, pp. 317–319, 2006. [Online]. Available: https://doi.org/10.1364/OL.31.000317 [Cited on page 25.]

[80] Y. Zhao, J. Zhao, and Q. Zhao, "Review of no-core optical fiber sensor and applications," *Sensors and Actuators A: Physical*, vol. 313, p. 112160, 2020. [Online]. Available: https://doi.org/10.1016/j.sna.2020.112160 [Cited on page 27.]

[81] A. Messica, A. Greenstein, and A. Katzir, "Theory of fiber-optic, evanescent-wave spectroscopy and sensors," *Applied optics*, vol. 35, no. 13, pp. 2274–2284, 1996. [Online]. Available: https://pubmed.ncbi.nlm.nih.gov/21085364/ [Cited on page 28.]

[82] X. Zhou, K. Chen, X. Mao, Q. Yu *et al.*, "A reflective fiber-optic refractive index sensor based on multimode interference in a coreless silica fiber," *Optics Communications*, vol. 340, pp. 50–55, 2015. [Online]. Available: https://ieeexplore.ieee.org/document/5545365 [Cited on page 29.]

[83] H. Fukano and K. Yoshioka, "Fiber-optic temperature sensor with selectively enhanced fabry–perot interference using focusing effect of graded-index fiber for cryotherapy," *Japanese Journal of Applied Physics*, vol. 59, no. SO, p. SOOD05, 2020. [Online]. Available: https://iopscience.iop.org/article/10.35848/1347-4065/ab9650 [Cited on pages 31 and 33.]

[84] S. Gupta, S. V. Sandhu, H. Bansal, and D. Sharma, "Comparison of salivary and serum glucose levels in diabetic patients," *Journal of diabetes science and technology*, vol. 9, no. 1, pp. 91–96, 2014. [Online]. Available: https://pubmed.ncbi.nlm.nih.gov/25294888/ [Cited on page 35.]

[85] J. E. Antonio-Lopez, J. Sanchez-Mondragon, P. LiKamWa, and D. A. May-Arrioja, "Fiber-optic sensor for liquid level measurement," *Optics letters*, vol. 36, no. 17, pp. 3425–3427, 2011. [Online]. Available: https://doi.org/10.1364/OL.36.003425 [Cited on page 36.]

[86] N. M. Razali, M. Q. Lokman, S. N. F. Zuikafly, F. Ahmad, M. A. A. Rahman, H. Yahaya, and S. W. Harun, "No-core fiber by self-image length optimization for optical based refractive index sensor," *Optical Fiber Technology*, vol. 74, p. 103133, 2022. [Online]. Available: https://doi.org/10.1016/j.yofte.2022.103133 [Cited on pages 37 and 39.]

[87] E. Morales-Narváez and A. Merkoçi, "Graphene oxide as an optical biosensing platform: A progress report," *Advanced materials*, vol. 31, no. 6, p. 1805043, 2019. [Online]. Available: https://doi.org/10.1002/adma.201805043 [Cited on page 41.]

[88] J. Kirkland, "Porous thin-layer modified glass bead supports for gas liquid chromatography," *Analytical Chemistry*, vol. 37, no. 12, pp. 1458–1461, 1965. [Online]. Available: https://doi.org/10.1021/ac60231a004 [Cited on page 42.]

[89] S. M. Haggag, A. Farag, and M. E. Mahmoud, "Layer-by-layer chemical deposition technique for thin film assembly of deposited nano-sized magnesium (ii)–5, 7-dinitro-8-hydroxyquinolate: Characterization and spectral–optical–electrical properties," *Polyhedron*, vol. 30, no. 16, pp. 2723–2732, 2011. [Online]. Available: https://doi.org/10.1016/j.poly.2011.08.002 [Cited on page 42.]

[90] P. Shende, A. Patil, and B. Prabhakar, "Layer-by-layer technique for enhancing physicochemical properties of actives," *Journal of Drug Delivery Science and Technology*, vol. 56, p. 101519, 2020. [Online]. Available: https://doi.org/10.1016/j.jddst.2020.101519 [Cited on page 42.]

[91] C. S. Monteiro, M. Raposo, P. A. Ribeiro, S. O. Silva, and O. Frazão, "Tuning of fiber optic surface reflectivity through graphene oxide-based layer-by-layer film coatings," in *Photonics*, vol. 7, no. 1. MDPI, 2020, p. 11. [Online]. Available: https://doi.org/10.3390/photonics7010011 [Cited on page 42.]

[92] F. Chiavaioli, C. A. Gouveia, P. A. Jorge, and F. Baldini, "Towards a uniform metrological assessment of grating-based optical fiber sensors: From refractometers to biosensors," *Biosensors*, vol. 7, no. 2, p. 23, 2017. [Online]. Available: https://doi.org/10.3390/bios7020023 [Cited on page 47.]

[93] J. Homola, "Surface plasmon resonance sensors for detection of chemical and biological species," *Chemical reviews*, vol. 108, no. 2, pp. 462–493, 2008. [Online]. Available: https://doi.org/10.1021/cr068107d [Cited on page 49.]

[94] Y. Zhao, R.-j. Tong, F. Xia, and Y. Peng, "Current status of optical fiber biosensor based on surface plasmon resonance," *Biosensors and Bioelectronics*, vol. 142, p. 111505, 2019. [Online]. Available: https://doi.org/10.1016/j.bios.2019.111505 [Cited on page 49.]

[95] B. D. Gupta, A. M. Shrivastav, and S. P. Usha, "Surface plasmon resonance-based fiber optic sensors utilizing molecular imprinting," *Sensors*, vol. 16, no. 9, p. 1381, 2016. [Online]. Available: https://doi.org/10.3390/s16091381 [Cited on page 50.]

[96] S. Huang, J. Hu, J. Wan, M. Johnson, H. Shu, and B. Chin, "The effect of annealing and gold deposition on the performance of magnetoelastic biosensors," *Materials Science and Engineering: C*, vol. 28, no. 3, pp. 380–386, 2008. [Online]. Available: https://doi.org/10.1016/j.msec.2007.04.006 [Cited on page 52.]

[97] N. Balistreri, D. Gaboriau, C. Jolivalt, and F. Launay, "Covalent immobilization of glucose oxidase on mesocellular silica foams: Characterization and stability towards temperature and organic solvents," *Journal of Molecular Catalysis B: Enzymatic*, vol. 127, pp. 26–33, 2016. [Online]. Available: https://doi.org/10.1016/j.molcatb.2016.02.003 [Cited on page 53.]

[98] S. Singh and B. D. Gupta, "Fabrication and characterization of a surface plasmon resonance based fiber optic sensor using gel entrapment technique for the detection of low glucose concentration," *Sensors and Actuators B: Chemical*, vol. 177, pp. 589–595, 2013. [Online]. Available: https://doi.org/10.1016/j.snb.2012.11.094 [Cited on page 53.]

[99] J. Huang, Y. Liu, P. Zhang, Y. Li, and L. Ding, "A temperature-triggered fiber optic biosensor based on hydrogel-magnetic immobilized enzyme complex for sequential determination of cholesterol and glucose," *Biochemical Engineering Journal*, vol. 125, pp. 123–128, 2017. [Online]. Available: https://doi.org/10.1016/j.bej.2017.06.002 [Cited on page 53.]

[100] J. Cao, E. K. Galbraith, T. Sun, and K. T. Grattan, "Cross-comparison of surface plasmon resonance-based optical fiber sensors with different coating structures," *IEEE Sensors Journal*, vol. 12, no. 7, pp. 2355–2361, 2012. [Online]. Available: https://ieeexplore.ieee.org/document/6156414 [Cited on page 56.]

[101] A. S. Assunção, M. Vidal, M. Loyez, C. Caucheteur, F. M. Costa, J. Mesquita-Bastos, C. Marques, S. O. Pereira, and C. Leitão, "Towards heart failure biomarker detection with plasmonic fiber tip biosensors," in *2022 IEEE International Symposium on Medical Measurements and Applications (MeMeA)*, 2022, pp. 1–5. [Online]. Available: https://ieeexplore.ieee.org/document/9856453 [Cited on page 56.]

[102] S. K. Srivastava, R. Verma, and B. D. Gupta, "Surface plasmon resonance based fiber optic glucose biosensor," in *Third Asia Pacific Optical Sensors Conference*, vol. 8351. SPIE, 2012, pp. 451–456. [Online]. Available: https://www.researchgate.net/publication/258715250 [Cited on page 59.]

[103] C. V. Raman and K. S. Krishnan, "A new type of secondary radiation," *Nature*, vol. 121, no. 3048, pp. 501–502, 1928. [Online]. Available: https://www.nature.com/articles/121501c0 [Cited on page 63.]

[104] J. W. Kang, Y. S. Park, H. Chang, W. Lee, S. P. Singh, W. Choi, L. H. Galindo, R. R. Dasari, S. H. Nam, J. Park *et al.*, "Direct observation of glucose fingerprint using in vivo raman spectroscopy," *Science Advances*, vol. 6, no. 4, p. eaay5206, 2020. [Online]. Available: https://www.science.org/doi/10.1126/sciadv.aay5206 [Cited on page 63.]

[105] J. Shao, M. Lin, Y. Li, X. Li, J. Liu, J. Liang, and H. Yao, "In vivo blood glucose quantification using raman spectroscopy," *PloS one*, vol. 7, no. 10, p. e48127, 2012. [Online]. Available: https://pubmed.ncbi.nlm.nih.gov/23133555/ [Cited on page 64.]

[106] C. C. Pelletier, J. L. Lambert, and M. Borchert, "Determination of glucose in human aqueous humor using raman spectroscopy and designed-solution calibration," *Applied spectroscopy*, vol. 59, no. 8, pp. 1024–1031, 2005. [Online]. Available: https://opg.optica.org/as/abstract.cfm?URI=as-59-8-1024 [Cited on page 64.]